Magnétorésistance de magnon reversement de l'aimantation et dynamique de parois dans FePt et NiFe nanostructures

van Dai Nguyen

▶ **To cite this version:**

van Dai Nguyen. Magnétorésistance de magnon reversement de l'aimantation et dynamique de parois dans FePt et NiFe nanostructures. Autre [cond-mat.other]. Université de Grenoble, 2012. Français. NNT : 2012GRENY039 . tel-00772893

HAL Id: tel-00772893

https://theses.hal.science/tel-00772893

Submitted on 11 Jan 2013

HAL is a multi-disciplinary open access archive for the deposit and dissemination of scientific research documents, whether they are published or not. The documents may come from teaching and research institutions in France or abroad, or from public or private research centers.

L'archive ouverte pluridisciplinaire **HAL**, est destinée au dépôt et à la diffusion de documents scientifiques de niveau recherche, publiés ou non, émanant des établissements d'enseignement et de recherche français ou étrangers, des laboratoires publics ou privés.

UNIVERSITÉ DE GRENOBLE

THÈSE

Pour obtenir le grade de

DOCTEUR DE L'UNIVERSITÉ DE GRENOBLE

Spécialité : **NANOPHYSIQUE**

Arrêté ministériel :

Présentée par

Van-Dai NGUYEN

Thèse dirigée par **Dr. Alain MARTY**
codirigée par **Dr. Jean-Philippe ATTANÉ**

préparée au sein **du Laboratoire de Nanostructures et Magnétisme et de l'École Doctorale de Physique**

Magnon magnetoresistance, magnetization reversal and domain wall dynamics in FePt and NiFe nanostructures

Thèse soutenue publiquement le**: 28 September 2012**

Devant le jury composé de:
Monsieur Hervé COURTOIS
Professeur, UJF Grenoble, Président
Monsieur André THIAVILLE
Directeur de recherche, Paris XI Orsay, Rapporteur
Monsieur Matthieu BAILLEUL
Directeur de recherche, IPCMS Strasbourg, Rapporteur
Monsieur Dafiné RAVELOSONA
Directeur de recherche, IEF Orsay, Examinateur
Monsieur Alain MARTY
Directeur de recherche, CEA Grenoble, Directeur de thèse
Monsieur Jean-Philippe ATTANÉ
Maitre de conférence, UJF Grenoble, Co-directeur de thèse

Université Joseph Fourier

Contents

Introduction

Spintronics

The discovery of the giant magnetoresistance (GMR) [1, 2] which awarded the 2007 Nobel Prize in Physics to A. Fert and P. Grünberg has triggered the rise of a new field of electronics called spintronics. This discovery is associated to a remarkable transition from fundamental research of spin-dependent transport in nanostructures to device applications in the area of data storage technologies. Spintronics devices exploit the spin degree freedom of electron rather than its charge, and offers new ways to store, carry and control the information. Such devices could also combine several advantages such as non-volatility, high speed data processing, reduced power consumption and high integration densities [3].

Among other, research in spintronics address two basic requirements: the detection and the manipulation of the magnetization in ferromagnetic nanostructures, which are the basic building blocks of spintronics. These two points are major challenges for fundamental research and the main topics of this thesis.

Magnetization reversal detection

Magnetoresistance (MR) effects based on spin-dependent transport properties can provide simple and fast ways to detect magnetization reversal in nanostructures. So far, the development of spintronics is based on few magnetoresistances including the giant magnetoresistance (GMR), the tunneling magnetoresistance (TMR), the anisotropic magnetoresistance (AMR) and the extraordinary Hall effect (EHE).

Important for both fundamental research and applications, the GMR is based on the large change of the resistance of a magnetic multilayer under the application of a magnetic field. The discovery of the GMR is considered to be the starting point of spintronics. Shortly later, spin-valve structures composed of two ferromagnetic layer separated by a nonmagnetic metallic layer, and exhibiting GMR effect were developed [4]. Basically, GMR spin-valves structures reveal the change in resistance depending on the relative orientation of magnetization of the two ferromagnetic layers in which the resistance is low when the magnetization in ferromagnetic layers are parallel and high when anti-parallel.

Later, the observation of room temperature TMR in 1995 [5] in magnetic tunnel junctions (MTJs) [6] was considered as a second breakthrough in the development of spintronics. MTJs consist of two ferromagnetic layers separated by an ultra-thin insulating layer in which the electrons can tunnel from one ferromagnetic layer to the other. As for GMR, the resistance of the stack depends on the relative orientation of the magnetization of the ferromagnetic layers. GMR reaches up to 180 % values whereas TMR goes up to 1000 % in MgO-based MTJ.

GMR and MTJ are the basic elements of spintronics devices which include magnetic field sensors, hard drives, read heads and magnetoresistive random access memory (MRAM) [7]. The higher the MR signal is, the smaller and faster the storage element can be.

Apart from the great potential for application, GMR and TMR are also of great interest for studying novel spintronics nanostructures since the change of resistance is quantitatively proportional to the orientation of the magnetization. Indeed, GMR measurement has been used to study magnetization reversal in an individual nanomagnet such as nanopillar [8] and is particularly used to detect domain wall (DW) position and motion in nanowires [9].

Although it was replaced by GMR for magnetoresistive HDD read heads [7], AMR is still an extremely important tool for studying the magnetic state of nanostructures. AMR was first observed in 1856 by William Thomson [10] and arises from the spin orbit coupling. The amplitude of AMR is much smaller than GMR and TMR (a few percent in some alloys based on 3d metals) but the resistance value is directly related to the orientation of the magnetization and the current lines [11]. AMR measurements have been thus extensively used to study magnetization reversal in materials with in-plane magnetization [11, 12, 13] and have been used more recently to probe the presence of DW in nanowires [14] or to distinguish different type of DW [15].

The EHE arises also from the spin–orbit scattering. The possibility for applications, such as magnetic sensors and nonvolatile MRAM, has been mentioned but no significant progress has reported until recently [16]. For nanostructures with perpendicular magnetization, the EHE is the most common detection technique of magnetization reversal [17]. Additionally, EHE is very important for characterizing DW motion and precise detection of DW position within Hall crosses [18].

It is worth noticing that extensive approach to follow DW motion is the use of imaging techniques such as Kerr, magnetic force microscopy (MFM), Lorentz transmission electron microscopy techniques and so on. In this thesis, we will mostly focus on the ways using magnetotransport measurements.

Magnetization reversal manipulation

The second important requirement for further development of spintronics is the ability to manipulate the magnetization reversal in nanostructures, which has been done conventionally

using magnetic field. In the first generation of MRAM devices, the magnetization of the memory element is switched by local magnetic fields generated when passing current through nearby metallic wires [19]. However, the writing current is high and limited by the CMOS electronic circuit.

For that reason, more efficient ways to switch the magnetization of nanodevices without the use of magnetic fields are sought. For instance, laser induced magnetization switching provide an ultra-fast way to manipulate magnetization [20] which can offer new perspectives for applications.

Recently, the experimental demonstration of current induced DW motion and magnetization switching in magnetic nanostructures opened a fast and promising way to manipulate magnetization.

Due to the spin dependent scattering of the electrons in magnetic materials, the electrical current is spin polarized, the direction of the spins being aligned with the direction of the local magnetic moments. The first concept of spin transfer torque induced DW motion was proposed by Berger in 1984 [21]. The idea is that across a DW, the exchange interaction aligns the spin direction of the conduction electron with the direction of local magnetization. To conserve the total angular momentum, it has to be transferred to the local magnetization, which is equivalent to a torque acting on the magnetization. This interaction consequently induces a displacement of the DW in the direction of the electron flow.

Experimental studies on current-induced DW motion have been performed shortly after the theoretical prediction (cf. ref. [22]). However, these early experiments have been mostly studied on thick NiFe films in which several difficulties arise as the extended thin films can result in more complex DW structures. Also, heating and Oersted fields become significant when increasing the film thickness and the current intensity. Importantly, these pioneering studies established the first steps for investigating current-induced DW motion.

The second concept of spin-transfer torque was proposed by Slonczewski in 1996 [23] and predicted that a flow of spin polarized current can exert a torque on the magnetic moments of thin magnetic layers and consequently switch the magnetization. Shortly later, this prediction was experimentally confirmed using point contact geometries [24] and nanopillars [25]. These results have basically shown that in order to observe the spin transfer torque effect, one needs to avoid the effect of the Oersted field and heating by reducing the size of the sample to nanoscale. Thus nanostructures such as nanopillar and nanowires became ideal systems for studying current-induced magnetization switching and DW motion.

Thanks to recent advances in lithographic techniques, magnetic nanostructures with lateral dimensions as small as a few tens of nanometers can be realized. In such nanostructures, the magnetic configuration can be properly tuned. For instance it is possible to study the current induced motion of a single DW inside nanowires, or the magnetization switching in the macro-

spin limit in pillars. Consequently, the topic of current induced magnetization switching became very active, both for experiments and theories [26]. This phenomenon offers an alternative way to conventional field-induced DW motion and new concepts based on DW motion such as the race-track memory or DW logic devices emerged [27]. These devices could simplify the design, integration and down-scaling of device architecture altogether with faster data processing and lower power consumption capabilities.

In the last decade, the number of studies on current induced DWs in magnetic nanowires has boomed. At first, single permalloy (NiFe) nanowires [28] or NiFe based spin valve structures [29] have been used to perform such experiments. As NiFe is the softest magnetic material, the magnetic properties can be well controlled, DW velocities are high (~100 m/s) [30] and the spin torque was expected to be efficient. Nevertheless, the critical current density for DW displacement at zero field is high $\sim 10^{12}\ A/m^2$ [26].

More recently, this topic progressively moved toward systems with perpendicular magnetization as CoPt [31], Co/Ni [32] and FePt [33] nanowires. These systems with high anisotropy increase the thermal stability and exhibit narrow DW that should present higher spin torque efficiencies (through the large magnetic gradient) and device densities [26].

On the theoretical side, the studies on current induced DW motion also flourished. Basically, the idea is to extend the Landau-Lifshitz-Gilbert (LLG) equations by adding spin transfer torque terms, *i.e.*, adiabatic and non adiabatic spin torque terms [34]. However, no consensus has still emerged on the origin and magnitude of the non adiabatic term. Moreover additional contributions such as Oersted field [35], Rashba effect [31] or automotive force [36] complicate the precise understanding of the phenomena.

Although such promising devices based on current induced DW motion motivated a large effort of research but several important open question need to be addressed. Discrepancies between theoretical and experimental results which linked to the nature of the current induced torques, the origin, the amplitude or even the existence of the non adiabatic torque term still exist. Different measurement methods and analysis has been used, which induce obviously different conclusions [26]. Additionally, the reduction of current densities for lower power consumption and increase of DW velocities for fast data processing are also major challenges.

Also, another promising way to manipulate the magnetization reversal in nanostructures is the use of pure spin currents which are created by either spin accumulation at the interface between ferromagnetic and metallic materials [37] or by the spin Hall effect [38]. The generation and detection of pure spin currents which are usually based on lateral spin valve structures [39] are also interesting perspectives in this field.

To conclude, the detection and the manipulation of magnetization reversal in nanostructures are crucial issues for both fundamental research and practical applications of spintronics devices. In this context, this PhD thesis will used a novel magnetoresistance effect, *i.e.*, the

Magnon magnetoresistance (MMR), to detect the magnetization reversal in nanostructures. We will show that this MR is able to provide information such as the DW position during the magnetization reversal. We will emphasis the versatility of this technique by doing so for two typical magnetic systems with planar (NiFe) and perpendicular magnetization (FePt). Having detected the position of DW in nanowires, we will study the DW depinning mechanism from different class of pining sites, either by field or current. For any device based on DW, this effect must be controlled precisely. We will show that similar features are found for both materials and a microscopic description of the phenomena will be given altogether with the comparison of field and current effects.

This thesis is organized as follows:

Chapter 1: Domain wall and magnetoresistance in nanostructures This chapter describes the micromagnetic origin of DW formation and the basic model of DW dynamics in nanostructures. The magnetotransport measurements which are usually used to detect magnetization reversal and characterize the DW motion in nanostructures are also presented.

Chapter 2: Magnetization reversal in FePt based thin films and nanowires Magnetization reversal in single layer FePt films and nanowires are presented, emphasizing on the dimensionality effect and the variation of reversal modes when reducing the wire width.

Chapter 3: Detection of magnetization reversal in FePt nanowires using the Magnon magnetoresistance This chapter will give a short description of the MMR in FePt thin film. We then show that MMR can be used to probe magnetization reversal in FePt nanowires and detect the switching field, the position of DW and its propagation along nanowires.

Chapter 4: Magnon magnetoresistance in NiFe nanowires and nanomagnets We will show that MMR measurements can be extended to systems with in-plane magnetization, as NiFe nanowires. We highlight the transition of MR signature from AMR to MMR by tuning the shape anisotropy and use the MMR to study the magnetization reversal in NiFe nanowires and nanomagnets.

Chapter 5: Stochasticity of domain wall depinning in ferromagnetic nanowires In this chapter, we study the stochasticity of DW depinning under applied field and current in magnetic nanowires having perpendicular (FePt) or in plane (NiFe) magnetization. By changing the class of DW pinning site, we observe three different behaviors of DW depinning in both systems and provide the associated microscopic descriptions.

Chapter 1

Domain wall and magnetoresistance in nanostructures

In this chapter, we begin with a short description of the domain wall (DW) structures in magnetic nanowires. We then discuss the theoretical models which have been developed to describe the phenomenon of the DW motion in nanowires driven by the magnetic field or the spin polarized current. The concepts for data storage applications based on the phenomenon of current induced DW motion will be shortly presented.

Finally, we will describe the experimental techniques to probe the position of a DW in nanowires which is a key point for studying field or current induced DW motion. In particular, we emphasize on the magneto-transport measurements which we mostly used in our studies, as they are well adapted to nanoscale structures.

1.1 Magnetic domain wall in nanowires

Magnetic DWs are boundaries between magnetic domain of different magnetic orientations. DWs play an important role in the magnetization reversal process of magnetic materials and have been intensively studied for many decades [40].

Basically, the formation of a domain results from the competition between various energy terms being: exchange, magnetocrystalline, Zeeman and magnetostatic energies. The total energy of the system is simply the sum of those energy terms:

$$E = E_{ex.} + E_{MC.} + E_{Zeeman} + E_{mag.} \tag{1.1}$$

As for all physical systems, the magnetic system tends to minimize its free energy. Since the magnitude of the magnetization vector is fixed, the way to do so is to vary its direction. The exchange energy ($E_{ex.}$) is minimized when the orientation of neighboring spins are par-

allel to each other. The magnetocrystalline energy ($E_{MC.}$) is associated to the direction of the magnetization relative to the some structural axes of the crystal. The Zeeman energy ($E_{Zeeman.}$) is minimized when the orientation of magnetization and the externally applied field are parallel. The magnetostatic energy arising from the dipole–dipole interaction is responsible for the formation of domain structures. Indeed, any uniformly magnetized regions will have lines of M that terminate on its surfaces. These sources and sinks of lines of magnetization will give rise to a nonzero divergence at these points. Using the basic relationship $B = \mu_0(H+M)$, we can express the divergence of M as:

$$\nabla.M = \frac{\nabla.B}{\mu_0} - \nabla.H \tag{1.2}$$

since the Maxwell's equation shows that $\nabla.B = 0$, it leads to $\nabla.M = -\nabla.H$

Hence these sources and sinks of magnetization at the sample surfaces will give rise to a field H that ensures the continuity of lines of B. This field is known as the demagnetizing field. The energy associated with this stray field H is expressed in the form of two equivalent integrals:

$$E_{mag.} = \frac{1}{2}\mu_0 \int\limits_{all\ space} H^2 dV = -\frac{1}{2}\mu_0 \int\limits_{sample} H.M dV \tag{1.3}$$

Note that the first expression is always positive, the second thus also must be always positive. The system will try to minimize this energy term as much as possible, making the stray field as small as possible. The second expression can be seen as the energy of a dipole MdV in the field created by the environment. By forming a non-uniform, flux-closed magnetic state, it is possible to reduce the number of lines of M that terminate on the sample surfaces and hence reduce the magnetostatic energy [41].

In general, one observes large uniformly magnetized regions separated by the regions where the magnetization rotates from the direction of one domain to the next. This region of non-uniform magnetization is called a DW. There are two typical types of DW known as Bloch and Néel (cf., fig. 1.1). Within a Bloch wall, the magnetization is oriented parallel to the plane of the wall. Whereas, in a Néel wall, the rotation of magnetization is perpendicular to the plane of the wall.

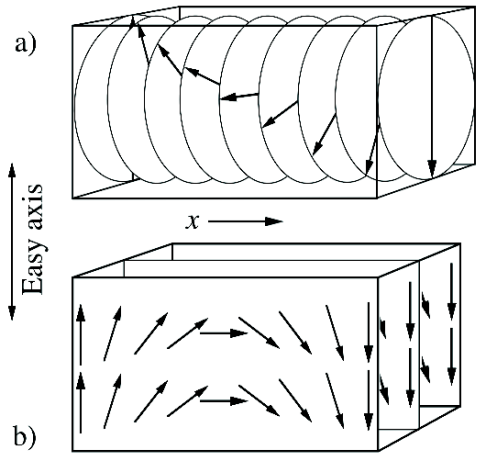

Figure 1.1: Schematics of (a) Bloch and (b) Néel DWs. In a Bloch wall, the magnetization rotates in a plane parallel to the plane of the wall. In a Néel wall, the magnetization rotates in a plane perpendicular to the wall (Figures are reproduced from [40])

In principle, the competition between the exchange and the magnetic anisotropy is responsible for the size of the DWs. If the exchange energy dominates, the wall tends to be wider, it is due to the fact that a small angle between adjacent spins results in a smaller exchange energy. On the contrary, the anisotropy energy causes a narrow DW, inside the wall the direction of spins is away from the easy axis of magnetization.

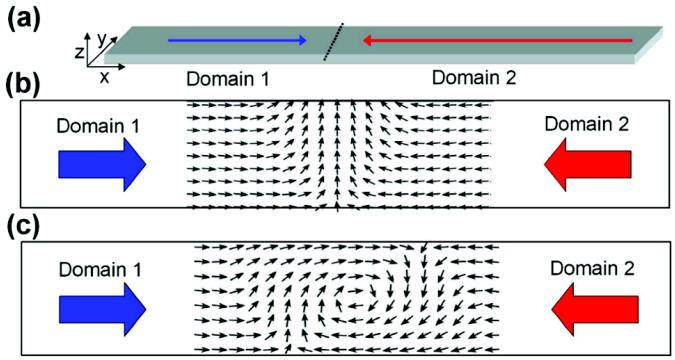

Figure 1.2: (a) Schematic presenting a magnetic wire with two domains pointing in opposite directions (red and blue arrows) and a domain wall (dotted line) separating the two domains. (b) top view of the spin structure of a transverse DW and (c) a vortex DW (Figures are reproduced from [26]).

In the case of nanowires with an in plane magnetization, the spin structures of DWs arising from the competition between the exchange energy and demagnetizating energy are predicted to be transverse walls or vortex walls (*cf.*, fig. 1.2) which depends on the width and thickness of the nanowires [42]. In the transverse wall, the spins rotate in the plane of the structure. Whereas, in vortex wall, the spins curl around the vortex core where the

magnetization is pointing out of the plane with a polarity pointing up or down. Also, the in-plane magnetization can curl clockwise or counter-clockwise around the vortex core leading to multiple configuration states. The energies of the two wall types vary with the geometry and material and it can be calculated from the micromagnetic simulations [26].

In film with perpendicularly magnetized materials, the anisotropy axis is perpendicular to the film plane and the anisotropy K is much larger than the demagnetizing energy $K_0 = \mu_0 M_S^2/2$ so that the magnetization is oriented perpendicularly to the film plane. The DW exhibit a Bloch configuration inside the layer and tends to the Néel one close to the surfaces (closure). The Bloch wall width is proportional to $\triangle = \sqrt{\frac{A}{K}}$ where A is exchange constant and K is anisotropy constant. In these systems, DW width parameters,$\triangle$ are typically of the order of a few nanometers. In FePt epitaxial thin films used in our study, the very strong magnetocrystalline anisotropy induces very narrow Bloch DW ($\triangle$~1 nm).

1.2 Domain wall motion in magnetic nanostructures

In principle, the operation of DW based devices is based on the displacement of DWs between at least two positions using either applied field or current pulses. Therefore, it is important to understand how DWs pin and depin in a magnetic nanostructure. It has been shown that there are several ways to pin DWs in magnetic nanostructures. For instance, the artificial pinning centers which can be properly defined using lithographies allows one to pin a DW at precise position in a nanowire. In nanowires with in-plane magnetization, there are various designs of artificial pinning sites which are mostly the notches or the constrictions with various widths and depths [42, 43]. For nanowires with out of plane magnetization, the pinning sites can be created using the local geometry of nanowires such as constrictions [44, 33], Hall crosses [45]. It can also be obtained by local change of the layer thickness [46], local decrease of the anisotropy using ion irradiation [47], pinning due to the edge roughness or lithographic defects [48]. Importantly, in such high anisotropic systems, the pinning sites due to intrinsic defects of layers are critical and can also efficiently pin DW [49]. The pinning can be due to a decrease of energy through the change of the DW length or by a reduction of the magnetocrystalline energy in the pinning potential landscape.

Once a DW is pinned, it will leave the pinning sites promptly if the strength of DW driving forces are strong enough to overcome the pinning barrier. Otherwise, they can cross the barrier by thermal activation, but with random delay leading to stochasticity. These DW driving forces can be provided by either an applied magnetic field through the Zeeman energy or by the electrical current through the spin transfer torque. This aspect will be discussed on the frame-work of the theoretical models which have been developed to describe the field and current induced DW motion.

1.2.1 Field induced domain wall motion

1.2.1.1 Landau-Lifschitz-Gilbert (LLG) equation

Understanding and controlling the field induced motion of DWs in nanowires [43, 50, 51] is an important preliminary step for studying their current-driven dynamics.

The dynamic of the DW motion under the influence of an applied field can be described by Landau-Lifschitz-Gilbert (LLG) equation:

$$\frac{\partial m}{\partial t} = -\gamma \overrightarrow{m} \times \overrightarrow{H_{eff.}} + \alpha \overrightarrow{m} \times \frac{\partial \overrightarrow{m}}{\partial t} \tag{1.4}$$

where m is the magnetization normalized to the saturation value, H_{eff} is the effective field which includes the external magnetic field and the contributions of anisotropy, demagnetizing and exchange fields, $\gamma = g\mu_B/\hbar$ is the gyromagnetic ratio where μ_B is the Bohr magneton, g the Landé factor, and α the Gilbert damping constant. The first term on the right-hand side of equation 1.4 is the precessional term which leads to the precession of the magnetization around the effective field direction. The second term is the damping term leading to the relaxation of magnetization towards this effective field.

1.2.1.2 Different regime of domain wall motion without pinning in ideal nanowires

Schryer and Walker [52] have studied the dynamic of DW motion deriving the first analytical solution for the motion of a Bloch wall in a uniaxial bulk materials under the influence of an applied field. The analytical solution within 1D model have predicted two separated regimes: a steady motion with a high mobility at low field and the precessional regime with a low mobility at high fields.

In an ideal nanowire without pinning sites, the motion of a DW has distinct characteristics depending on the magnitude of the applied field. In the first regime, at low fields, the DW velocity reach a steady value. In this stationary regime, the velocity increases linearly with field, according to the relation [43]:

$$\nu(H) = \frac{\gamma \triangle}{\alpha} H \tag{1.5}$$

where $\nu(H)$, γ, $\triangle$, α, H are velocity of DW motion, gyromagnetic ratio, DW width, Gibert damping, magnetic field, respectively.

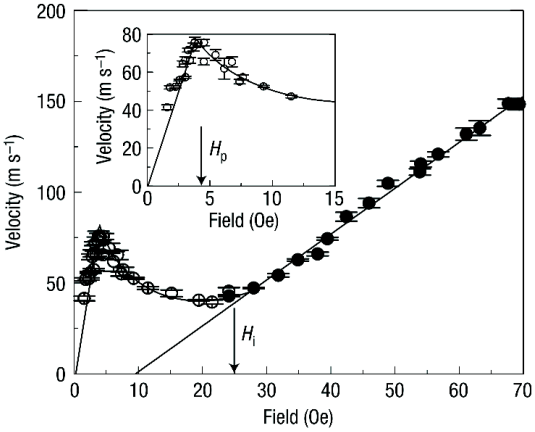

Figure 1.3: DW velocity determined by time-resolved MOKE measurements in a single layer permalloy nanowire as function of the applied field. This curve shows two regimes of the DW motion which are separated by the Walker breakdown field. (Figures are reproduced from ref. [53]).

When the field exceeds a certain threshold value, called Walker breakdown field, the average DW velocity drops sharply. Above this field, the DW moves in a complex manner, and its velocity oscillates in time. When the field is increased further, the average velocity is again proportional to the field, although the wall mobility is strongly reduced compared to the low-field value. The velocity in this second regime depends on the field value according to the relation:

$$\nu(H) = \frac{\gamma \triangle}{\alpha + \alpha^{-1}} H \tag{1.6}$$

There are several experimental results on the dynamic of DW motion in nanowires using time resolved measurements. The parameter widely used to characterize DW motion is the wall mobility which is defined as the change of DW velocity with the applied field. For example, Ono *et al.,* [9] have used GMR measurements to probe the propagation of the DWs in 500 nm wide NiFe/Cu/NiFe multilayer structures. They found that the DW velocity increases linearly with field above a threshold value but with relatively low mobilities, ν/H of about 2.6 m/s.Oe.

Atkinson *et al.,* [54] performed a similar study on a single layer Permalloy nanowire using time-resolved MOKE experiments. The DW motion was probed at very short timescale (20–500 ns). These authors also found that the DW velocity increased linearly with field as previously reported in ref. [9]. However, the DW mobility was more than 10 times higher (~38 m/s.Oe). These experiments have been performed in relatively high fields compared to the Walker breakdown fields.

In 2005, Beach *et al.*, [53] experimentally observed two regimes of the DW motion in single layer Permalloy nanowires as the predicted by Walker (*cf.,* fig. 1.3). This is the first observation of the Walker breakdown which was found to be a few Oersteds. They also showed that in the high-field regime, the velocity also increases linearly with field.

1.2.1.3 Different regime of domain wall motion in nanowires: The role of intrinsic defects

In systems with high magnetocrystalline anisotropy as FePt, Co/Ni or Co/Pt, the role of layer defects are no longer negligible. Indeed, once the DW is injected, in order to propagate further, DW has to overcome the local energy barriers (induced by structural disorder of the layer) which give rise to the threshold field H_P, *i.e.,* propagation field at T=0 K. Basically, at zero temperature, DWs are pinned until the propagation is reached. At finite temperature, thermal energy can allow DW propagation below the propagation field. This results from the competition between an elastic energy that acts to straighten the DW and a random structural disorder which tends to roughen it by local pinning site [51]. In this case, the motion of DW is characterized by two different regimes: a thermally activated regime below the propagation field and a viscous regime above the propagation field. This has been theoretically [55] and experimentally [48, 56, 51] studied in nanostructures with perpendicular magnetization.

It has been observed two different regimes for the DW motion in Pt/Co/Pt nanowires: a thermally activated regime and a viscous regime (*cf.,* fig. 1.4). In the thermally activated regime $H < H_P$, the velocity of DW motion can be given by [51]:

$$\nu(T,\ H) = \nu_0 exp\left(\frac{-2M_S V(H_P - H)}{k_B T}\right) \tag{1.7}$$

where k_B is the Boltzmann constant and T the temperature, H and H_P are the applied and propagation fields, respectively, and V is the activation volume.

In the creep regime for $H \ll H_P$ which reveals the response of DW to small applied field, the DW velocity is written by:

$$\nu(T,\ H) = \nu_0 exp\left(\frac{-U_C(H_P/H)^{1/4}}{k_B T}\right) \tag{1.8}$$

where U_C and H_P are the scaling constant and the propagation field, respectively.

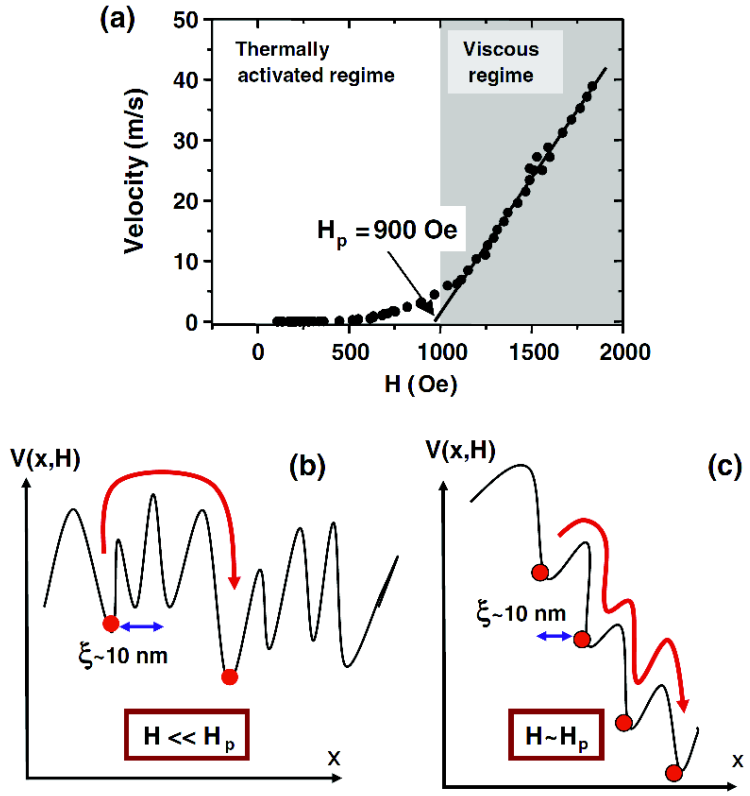

Figure 1.4: (a) DW velocity as a function of field in a Pt/Co/Pt sample. When $H > H_P$, the DW propagation is in a viscous regime and the velocity is linear in fields. For $H < H_P$, the DW motion is in thermally activated regime. The propagation field is determined by the intersection between the linear regime and $\nu = 0$. (b, c) Schematic illustration of the pinning potential $V(x,\ H)$ experienced by a DW for $H \ll H_P$ and $H \sim H_P$. The red arrows correspond to the jump to the next metastable state (Figures are reproduced from ref. [51]).

Basically, the difference between the two thermally activated regimes is that for $H \ll H_P$, two neighbor metastable states are separated by a high energy barrier. While for $H \sim H_P$, the pinning potential is slightly tilted under the action of the magnetic field. Experimentally, Cayssol *et al.*, [48] found in Pt/Co/Pt nanowires that the wall velocity varies as the inverse of the wire width, and decreases with wire roughness. Both regimes are characterized by very small DW velocities ($\sim$1 m/s).

Finally, for high applied fields $H > H_P$, a viscous flow regime is attained in which, the domain wall velocity varies linearly with the applied field

$$\nu(H) = \mu(H - H_P) \tag{1.9}$$

where μ is the DW mobility. In this regime, the disorder only acts as a friction force that renormalizes the applied magnetic field [51].

1.2.2 Current induced domain wall motion

1.2.2.1 Early model of current induced domain wall motion

The first model of interaction between spin polarized currents and the DW has been proposed by Berger [21]. The first type of interaction that can occur when a polarized current flows a magnetic system is called self-induced DW drag or hydromagnetic domain drag [57]. According to Berger, the current loop arising from nonuniform current distribution around a DW creates a magnetic field. This thus exerts a net force on the DW in the direction of the drift velocity of the carriers and it can lead to DW motion.

The second type is the $s-d$ exchange interaction between the conduction electrons and the localized magnetization. Berger showed that such interaction can influence the DW dynamics in two different ways. The first contribution which is called s–d exchange drag [21], is a viscous force on the DW which is proportional to the current. This term arises from the difference between the spin-dependent reflection coefficients of the conduction electrons at the DW. The second contribution is an exchange torque related to the transfer of spin angular momentum from the s conduction electrons to the localized magnetization [58] which is similar to the model of spin transfer torque in multilayers proposed by Slonczewski [23].

1.2.2.2 Model of current induced domain wall motion

The influence of the current on the DW dynamics can be studied by solving the Landau–Lifshitz–Gilbert (LLG) equation of motion [34]. Two spin-torque terms which are proportional to the gradient of the magnetization are added to the LLG equation. In the case of homogeneous magnetic materials, and assuming that the current is flowing along the x direction, the LLG equation can be written as :

$$\frac{\partial \overrightarrow{m}}{\partial t} = -\gamma \overrightarrow{m} \times \overrightarrow{H_{eff}} + \alpha \overrightarrow{m} \times \frac{\partial \overrightarrow{m}}{\partial t} - u \frac{\partial \overrightarrow{m}}{\partial x} + \beta u \overrightarrow{m} \times \frac{\partial \overrightarrow{m}}{\partial x} \tag{1.10}$$

The first two terms on the right-hand side of equation1.10 are describing the magnetization dynamic under the applied field. The last two terms describe the interaction with the current. The first current contribution is called adiabatic torque term. In the adiabatic limit which is valid for a wide DWs, the conduction electrons spin stays parallel to the local magnetization direction due to the exchange interaction. The magnitude of the adiabatic spin torque, which can be derived directly from the conservation of spin angular momentum, is given by [59]:

$$u = \frac{g \mu_B J P}{2 e M_S} \tag{1.11}$$

where J, P, and e are the current density, the spin polarized current, and the electron charge, respectively. The parameter u is called the spin drift velocity and is actually the

maximum velocity that the DW can reach in the adiabatic limit when the conduction electron spin moments are fully converted into DW displacement.

Since the result of analytical or micromagnetic simulations based on the description of spin transfer torque in the adiabatic limit were not reproducing quantitatively the experimental results [59]. Thiaville *et al.*, [34] introduced a second term in the LLG equation 1.10 which is called the non-adiabatic spin torque. This term basically occurs in systems with narrow DW in which the gradient of magnetization is too large for the spin polarized current to follow the local magnetization direction. Non-adiabatic spin torque is characterized by a dimensionless constant β. However, both the origin and the magnitude of β is still not clear. Many mechanisms have been proposed to explain the β term such as momentum transfer [60], spin mistracking [61] or spin-flip scattering [62]. It is predicted that a large non-adiabatic effect should appear in narrow DW due to the large magnetization gradients [60]. However, no consensus has merged on the value of β. For instance, the calculation in ref. [63] showed that β should be equal to α while other models indicated that this is not the case [64]. The experimental studies also found very different values of β parameter for both in plane [65, 43] and perpendicular anisotropy system [45, 33].

This dispersion of β value arises from the theoretical model and experimental method that are used to estimate β. This could also arise from the additional contributions such as the Oersted field [35], the Rashba effect [66] or automotive force[36].

1.2.2.3 Effect of Oersted field and Joule heating on current induced domain wall motion

Apart from the spin transfer torque induced DW motion, the Oersted field created by the current flow into the sample also affects on the DW depinning process. Experimentally, current induced DW motion usually require high current densities giving rise to large Oersted fields. Basically, this field is transverse to the current direction, its influence in single layer nanowires is often neglected because there is no net field along the nanowire direction. However, for spin valve structures where the distribution of current lines are usually inhomogeneous and asymmetric due to the different resistivities of the layers, it results an uncompensated Oersted field in the direction transverse to the nanowire within each layer. It has been shown that such effect can play a significant role on the DW motion, in particular for sample with weak pinning sites or low propagation fields [35, 43]

Additionally, high current densities leads to a significant contribution of Joule heating effect. This may lead to local temperature increases. It can be up to a few hundred of Kelvins depending on the wire structure, the material composition and current densities [45]. This is obviously influencing on the experiments, especially by getting close to the Curie temperature. For example, the change in the nanowire's resistance and thermal energy due to Joule heating

can lead to incorrect values of spin torque efficiency if it is not properly taken into account [67, 42, 45]

1.2.3 Applications of current induced domain wall motion

Although the mechanism of spin transfer torque phenomenon is still under discussions, the experimental results clearly demonstrated that spin polarized current can manipulate the motion of the DWs along nanowires. These results make the spin transfer torque phenomenon on the road toward applications. Indeed, several concepts for data storage based on such phenomenon have been recently proposed.

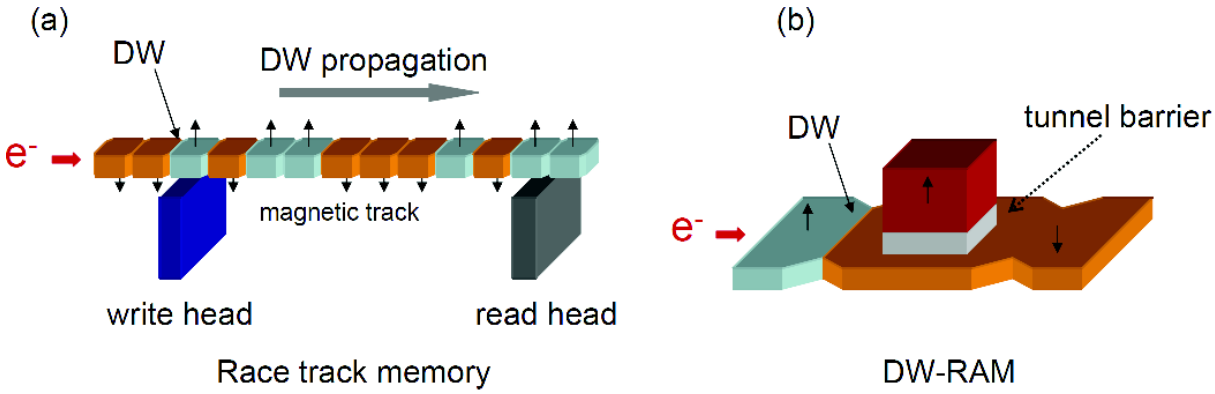

Figure 1.5: Schematics of the device based on current induced DW motion: (a) the race track memory and (b) DW-RAM.

The most famous concept of DW based memory has been proposed by Parkin *et al.*, it is called the race track memory [27]. Basically, this device contains a number of DWs in which each one carries an information bit being shifted synchronously by current pulses along a nanowire (*cf.*, fig. 1.5a). The race track memory has the advantage to combine the high density of the hard disk approach with the reliability of solid state memory. Such device is then operated without mechanically moving parts. A second concept is DW Random Access Memory (DW-RAM) in which the magnetic bit is written through the propagation of a DW in a narrow track while the bit is read using a magnetic tunnel junction (*cf.*, fig. 1.5b) [68]. In principle, this device uses current induced DW motion to switch a bit from P state ("0") to AP state ("1"). Despite a more complex three terminal architecture compared with standard MRAM, a low writing current is obtained even for relatively high current density due to the small cross-section area of the track. The RAM endurance can be increased since no writing current is flowing in the junction. Using high perpendicularly magnetized materials will be promised to reduce the size of device and increase the thermal stability, altogether with smaller power writing. These two concepts are the DW based counterpart of the MRAM or Spin-RAM based on pillar shaped vertical structures.

1.3 Magnetoresistance effects in nanostructures: Domain wall detection

The recent trends in nanomagnetism are shifting toward magnetic nanostructures, which are of technological relevance. Nevertheless, detection of the magnetization reversal of such nanostructures is a challenge since the magnetic moment is very tiny (*e.g.,* order of 10^{-15}-10^{-141} emu for Fe particles of 5-20 nm size [69]). Experimentally, such measurements can not be performed by the conventional magnetometers as vibrating sample magnetometer (VSM) or superconducting quantum interface device (SQUID) since the magnetic signal is well beyond the sensitivity limit of the such magnetometers (sensitivity is order of 10^{-5} emu for VSM or $\sim 10^{-7}$ emu for SQUID) [70]. The MR effects based on the interaction between spin polarized currents and magnetization can provide an easy and fast technique to study magnetization reversal in nanostructures. These techniques are one of most popular way to investigate the magnetization reversal in nanostructures [12, 9, 8, 71, 13].

This part will briefly discuss the use of magnetotransport measurements to detect magnetization switching and, in particular, to characterize the DW motion in nanostructures. The anisotropic magnetoresistance (AMR) is used to study in-plane magnetized single layer while the use of the extraordinary Hall effect (EHE) is favored for systems with out of plane anisotropy. For multilayer structures, the detection of magnetization reversal can be carried out using the giant magnetoresistance (GMR) effect. GMR measurements can provide information on the DW position along a nanowire while AMR can only probe the presence of the DW.

1.3.1 Anisotropic magnetoresistance

In a metallic ferromagnet, the variation of resistivity in the presence of external magnetic field typically exhibits the AMR effect in which the resistance depends on the angle between the current lines and magnetization directions. AMR effect which arises from spin-orbit coupling can reach few a percent in some alloys based on *3d* metallic Fe, Co, and Ni at room temperature [11]. In general, the resistance is high when the current lines are parallel to the direction of magnetization and low when the magnetization is perpendicular to the current. Let us define θ the angle between the magnetization and the direction of the current, the resistivity can be expressed by:

$$\rho = \rho_{\perp} + (\rho_{\parallel} - \rho_{\perp}) cos^2\theta \tag{1.12}$$

where $\rho_{\perp}$and $\rho_{\parallel}$ are the resistivities obtained when the magnetization is perpendicular or parallel to the current direction.

In in-plane magnetized systems, AMR is thus sensitive to the magnetization components during the reversal process, AMR has been commonly used to investigate magnetization reversal in nanostructures, especially in nanowires. The angular dependence of the switching field measurement allows studying magnetization reversal modes in such nanostructures [13, 71, 12].

The presence of a DW within nanowires will induces a change of the total resistance because the magnetization within the DW deviates from the current direction. A local variation of the magnetization direction within the DW with some magnetic moments having a component perpendicular to the current direction results in a lower resistance compare to the saturated state.

Therefore, AMR measurements have been commonly used to detect the presence of DW in nanowires [14, 42]. As an example, Thomas *et al.*,[43], shows the MR measurement 300 nm wide and 4 μm long NiFe nanowire with a triangular notch patterned on one side of the wire, which acts as a pinning center for the DW (*cf.,* fig. 1.6).

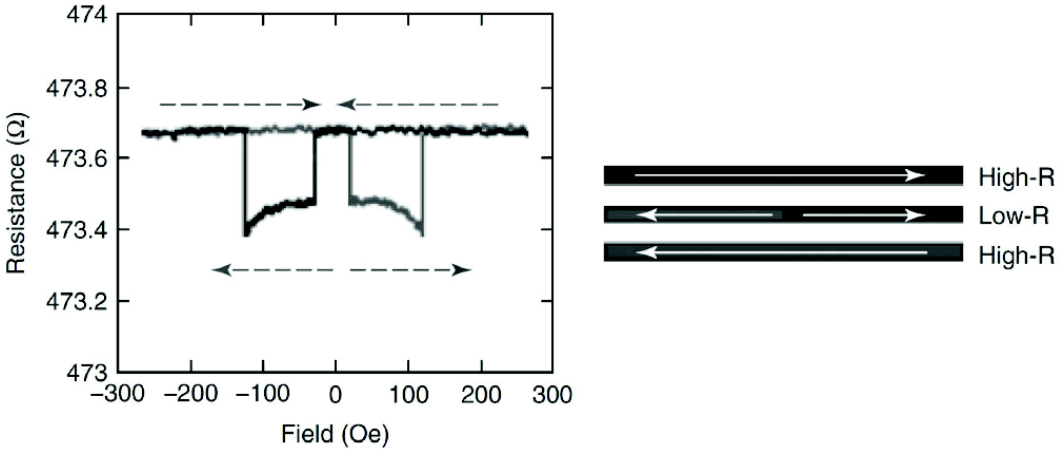

Figure 1.6: Examples of MR curves obtained when the propagation of a DW along a NiFe nanowire is probed by AMR (Figures are reproduced from ref. [43])

In the saturated state, magnetization is parallel to the current flow, the resistance is at the highest level. The partially reversed state corresponds to the injection of a DW into the nanowire that is trapped at the pinning site. This results in a sharp drop of resistance of $0.2\,\Omega$ due to the misalignment of the local magnetization within the DW and the current direction. By further increasing the applied field, the DW is driven from the pinning site to the outside of the contacts probes and the resistance reverse back to the saturation value through a sharp increase of resistance (*cf.,* fig. 1.6).

Although the signal is rather small ($\sim$0.04 % [43]), the AMR can be highly sensitive to the details of the DW structure [42, 15]. In particularly, AMR can distinguishes the vortex and transverse wall since they reveal a different component of the magnetization which is perpendicular to the current direction. However, AMR measurements is not sensitive to the

position of DW, it only detects the presence or absence of a DW in between the contacts. Therefore, such measurements can not provide any information about the position and the displacement of the DW. On the other hand, it has been recently showed that the enhancement of shape anisotropy in narrow NiFe nanowires leads to the disappearance of AMR effect [72]. AMR measurement is also quite limited to the study of magnetization reversal in narrow nanowires.

1.3.2 Extraordinary Hall effect

In ferromagnets, the Hall effect consists of two contributions, the ordinary and the EHE [73] being proportional not only to the external field H_{ext} but also to the magnetization M of the ferromagnet. The Hall resistivity ρ_H is thus described as:

$$\rho_H = \rho_0 H + 4\pi\rho_S M_\perp \tag{1.13}$$

where ρ_0, ρ_S are ordinary and extraordinary Hall coefficient, respectively. H is the external applied field and $M_\perp$ is the perpendicular magnetization. The ordinary Hall effect is associated to the Lorentz force acting on moving charge carriers. The EHE is related to the spin–orbit scattering in magnetic materials and the effect is much larger than the ordinary Hall effect in metals. Experimentally, when increasing the applied field H_{ext}, ρ_H changes rapidly at first due to the alignment of the magnetization, and then tends to vary in proportion to the applied field. The constant increment gives the value of ρ_0, and the extrapolated value of ρ_H to $H_{ext}= 0$ gives the value of $4\pi\rho_S M$. This analysis shows that EHE measurement can provide the information of the net magnetization in magnetic materials.

For the material with perpendicular magnetization, EHE has been extensively used as a powerful technique to detect magnetization switching in nanostructures [17, 74] and also commonly used to characterize DW motion [18, 45, 32]. Such measurement provide a large signal which allows the precise detection of DW motion within the Hall cross [75]. As an example, Ravelosona *et al.*, [18] shows EHE minor loop in fig. 1.7 corresponding to the reversal of the free layer in spin valve structure by propagation of a single DW through the 200×200 nm^2 Hall cross. The variation of the EHE allows detecting the DW motion on a scale as small as 10 nm, such as the jump indicated in fig. 1.7c.

However, it only points out the position of a DW within a Hall cross. Therefore, EHE measurement requires the devices to be patterned into a Hall cross geometry which limits the flexibility of the device structures.

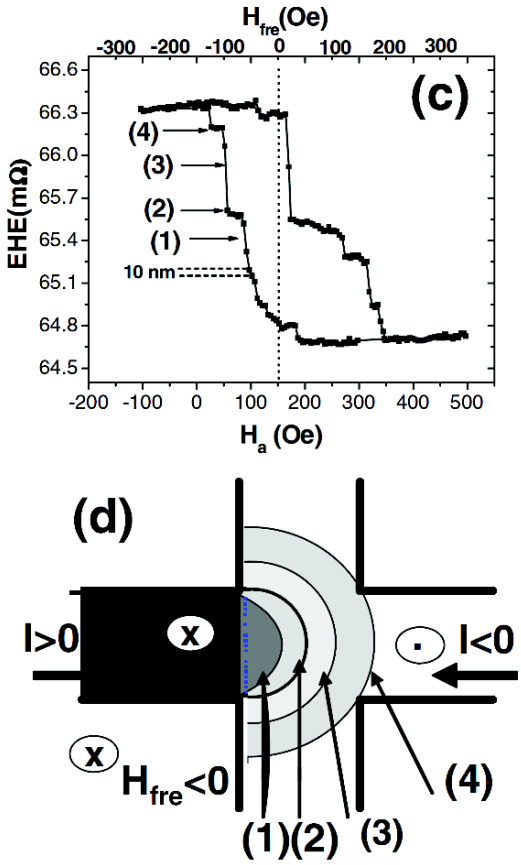

Figure 1.7: (c) EHE minor loop corresponding to the reversal of the free layer in a 200×200 nm^2 Hall cross. A small EHE jump corresponds to DW motion over 10 nm, the EHE values (1) to (4) refer to the positions indicated in (d) (Figures are reproduced from ref. [18]).

1.3.3 Giant magnetoresistance

GMR was first observed in samples with a large number of repetitions of Fe/Cr bilayers [1], this consequently leaded to the development of spin valve structures in which two ferromagnetic layers are separated by a thin metallic non-magnetic spacer [4]. In such structures, one ferromagnetic layer acts as a free layer in which its magnetization is easily reversed by a small magnetic field. The other one is a reference layer, *i.e.*, its magnetization remains unchanged under a small magnetic field due to a larger coercive field [76].

The mechanism of GMR can be basically understood in terms of spin-dependent resistivity and spin accumulation in magnetic and non-magnetic layers. These origins are closely related to each other and are at the heart of the mechanism of GMR effect which can be presented in the simple picture of the two current models (*cf.*, fig. 1.8).

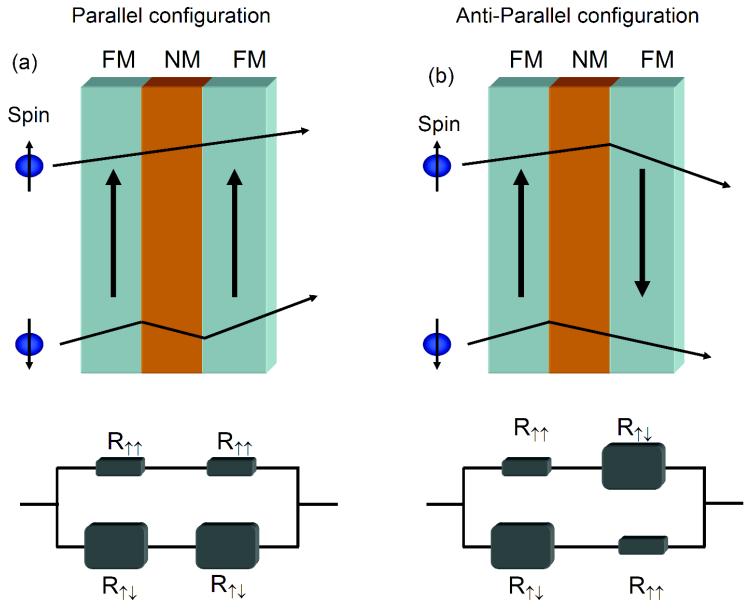

Figure 1.8: Schematic illustration of electron transport in a multilayer structure for (a) P and (b) AP configuration of two ferromagnetic layers. The solid lines are schematic illustration of individual electron trajectories within the two spin channels. Bottom panels show the resistor network within the two-current series resistor model.

In parallel configuration (P) of the magnetization, one of the two spin channels has a low resistance while the other has a high resistance (*cf.*, fig. 1.8a). Whereas, in anti-parallel configuration (AP), both spin channels have high resistance, since both up spin and down spin electrons are scattered at the interfaces (*cf.*, fig. 1.8b). As a result, the resistance in AP *c*onfiguration is larger than that in *P* configuration. Further details on the GMR effect and its developments for spintronics application can be found in this review paper [77].

Obviously, the GMR effect reveals that the change in resistance depends on the relative orientation of magnetization of the two ferromagnetic layers. This means that the variation of the resistance is proportional to the amount of reversed magnetization in one of the ferromagnetic layers. Such measurement provide a powerful technique to detect quantitatively the magnetization reversal in nanostructures. It has been shown that GMR measurement can be used to study magnetization reversal in individual nanostructures as nanopillars [8] or nanowires [9].

During the magnetization reversal of one ferromagnetic layer, the total resistance of the system is given by some average of the resistances in the P and the AP configuration. In the case of spin valve based nanowires, the domains are assumed in series with respect to the current direction then the resistance of this system can be given by [78]:

$$R = \frac{x}{L} R_{\uparrow\uparrow} + \frac{L-x}{L} R_{\downarrow\uparrow} \tag{1.14}$$

where x is the position of a DW, L is the length of the wire, $R_{\uparrow\uparrow}$ is the resistance for P configuration and $R_{\downarrow\uparrow}$ is the resistance for AP configuration. This equation underlines that a simple resistance measurement allows detecting the position of a DW. Experimentally, Ono *et al.*, [79] has showed an example of GMR measurement to measure DW position in a 500 nm wide NiFe/Cu/NiFe nanowire (*cf.,* fig. 1.9).

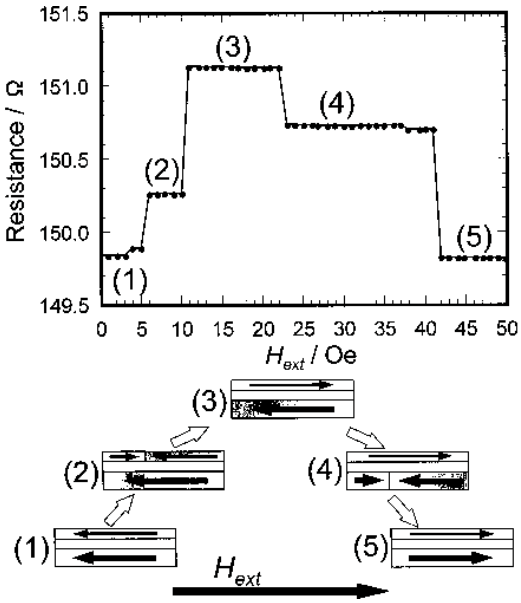

Figure 1.9: Resistance as a function of the external magnetic field of 500 nm wide NiFe/Cu/NiFe wire at room temperature. The magnetic domain structures inferred from the resistance measurement and the direction of the external field are schematically shown (Figures are reproduced from ref.[79]).

Fig. 1.9 shows the variation of GMR as a function of the applied field in which four very sharp leaps are observed. Increase of resistance (state 1) corresponds to the reversal of the free NiFe layer, a plateau of resistance at state 2 corresponds to the pinning of DW on the free NiFe layer. The ratio of the resistance changes from state 1 to state 2 allows measuring DW position where it pinned on the free NiFe layer by using the equation 1.14. Similarly, the DW position on the reference NiFe layer also can be detected based on the ratio of resistance changes from state 3 to 4. This result proved that the GMR is directly sensitive to the position of the DW along the nanowire, emphasizing that such measurement is very attractive for studying DW motion [78]. So far, spin valve structures have been extensively used to characterize the DW propagation in nanowires [79, 9, 18, 29, 33, 67]

However, the presence of the additional layers, *i.e.,* the reference and spacer layers in spin valve structures can give rise to several problems. For example, the shunting of current through the nonmagnetic spacer layer, which is typically much more conducting than the other layers in the stack, results in an inhomogeneous current distribution through the wire. This can also lead to the creation of Oersted fields which might influence the DW dynamics [35].

Arising vertical spin current or mirroring of the DW in the reference layer can alter the DW configurations. These can make the interpretation of the results more complicated.

1.4 Conclusions

In this chapter, we have briefly discussed the configuration of DW structures in magnetic nanowires. The formation of DW structures arise from the interplay between the exchange energy, anisotropy energy and demagnetizing energy which typically showed that transverse walls or vortex walls in nanowires with in plane magnetization and mixing Bloch and Néel configurations in nanowires with perpendicular magnetization.

We then discussed the theoretical models of the DW motion in nanowires driven by the magnetic field which basically showed the different regimes of DW motion. In the case of ideal nanowires without pinning which mostly apply for system with in-plane magnetization, the motion of DW is characterized by two regimes: a steady motion with a high mobility at low field and the precessional regime with a low mobility at high fields. While in the system with narrow DWs, because the pinning is induced by intrinsic defects, the motion of DW is separated by two regimes: a thermally activated regime for fields smaller than the propagation field and viscous regime for applied field higher than the propagation field.

The influence of the current on the DW dynamics was discussed by introducing two spin-torque terms (*i.e.,* adiabatic and non-adiabatic spin torque terms) which are proportional to the gradient of the magnetization in the LLG equation. The adiabatic spin torque term was well understood in term of the conservation of spin angular momentum in which the electron spins exert a torque on the magnetization which leads to the motion of DW. However, the understanding of the microscopic origin and the amplitude of the non-adiabatic torque term is still under discussions. The measurement of the β value shows very much different value depending on the measurement methods and the model used to extract the β term. Also, we shortly presented the concept for new data storage devices based on the current induced DW motion phenomenon.

We finally presented the typical magnetotransport measurements which can provide a good spatial and temporal resolution to detect magnetization switching, in particular, to characterize DW motion in nanowires. This part implied the comparison between the available techniques for the DW detection by AMR, EHE and GMR with the MMR which have been successfully developed in our group. This latter type of measurement will be described in detailed in the following chapters to characterize the motion of a DW for systems with either perpendicular or in plane magnetization.

Chapter 2

Magnetization reversal in FePt based thin films and nanowires

In this chapter, we will present the investigation on the magnetization reversal of high perpendicular anisotropy FePt materials with ultrathin DW . We particularly focus on the DW pinning on the structural defects and the dimensionality effect on the magnetization reversal modes of FePt nanostructures [80, 81].

Firstly, we will give a description of the growth and magnetization reversal process in a single FePt thin film and FePt/Pd/FePt spin valve deposited on MgO substrate. Secondly, we will show the effect of nanostructuration on the intrinsic coercivity and the change of the magnetization reversal modes when reducing the dimension of the nanowires. These results emphasis the importance of controlling these reversal modes for next experiment on studying the DW propagation in such nanowires. On the other hand, in view of applications, these effects must be controlled precisely, especially to reach technological nodes below 30 nm when pushing the scalability of DW-based devices towards ultimate sizes.

2.1 FePt based thin films

2.1.1 Growth of a single FePt thin film on MgO substrate

At room temperature, the equilibrium phase of $Fe_{50}Pt_{50}$ is in $L1_0$ phase (*cf.*, fig. 2.1a). The unit cell is tetragonal and the crystal structure can be described by a stacking of Fe and Pt atomic planes. There is a quadratic axis along the [001] direction corresponding to an easy axis of magnetization. The axial ratio c/a of the lattice parameters is slightly less than one, c/a$\sim$0.96-0.98. In the disordered fcc phase, the Fe and Pt atoms randomly occupy the lattice sites. In the case of FePt $L1_0$ phase, we can define an occupancy $n_{Fe/Fe}$(or $n_{Fe/Pt}$) of Fe atoms in the sub-lattice of Fe (or Pt). The order parameter for the ordered phase is defined

as:

$$S = \left[n_{Fe/Fe} - n_{Fe/Pt} \right] \tag{2.1}$$

In the ordered phase, the directional short range order is directly responsible for the anisotropy, it can be quantified using the probabilities $P^{Fe/Fe}_{In-plane}$ and $P^{Fe/Fe}{}_{out-of-plane}$ corresponding to the probabilities for a Fe atom having a first neighbor Fe in plane or out-of-plane. In the case of the stoichiometric composition $Fe_{50}Pt_{50}$, these probabilities vary from $P^{Fe/Fe}_{In-plane}$ $=P^{Fe/Fe}_{out-of-plane}$ $=0.5$ for disordered phase to $P^{Fe/Fe}_{In-plane}= 1$ and $P^{Fe/Fe}_{out-of-plane} = 0$ for perfectly $L1_0$ ordered alloy. Experimentally, the long range order can be measured by X-ray diffraction. The short range order which is directly responsible for the magnetocrystalline anisotropy of the $L1_0$ alloys is more difficult to measure quantitatively. However, V. Gehanno *et al.*, showed that this directional short range order parameter can be evaluated by using the polarized X-ray absorption fine structure (EXAFS) measurement [82]

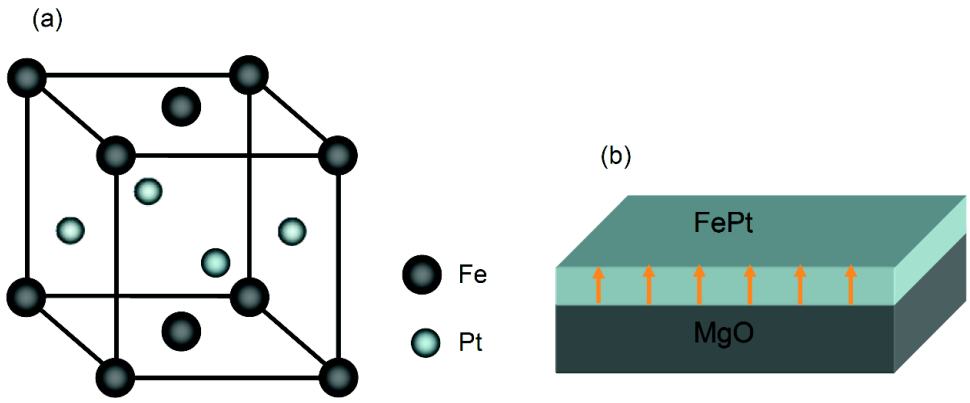

Figure 2.1: (a) Schematic of crystallography FePt structure chemically order in the $L1_0$ phase, with lattice parameters c = 0.379 nm and a = 0.386 nm. (b) Schematic of FePt films deposited directly on MgO substrate.

The microstructure and magnetic properties of $L1_0$ FePd and FePt thin films deposited by Molecular Beam Epitaxy (MBE) on MgO substrates has been extensively studied in our Laboratory: it has been particularly studied in previous PhD thesis [83, 84, 85, 86]. These works showed that the optimized condition to obtain the high order corresponding to the high magnetocrystalline anisotropy of FePt thin film can be of two ways:

+ Growth of FePt film at high temperatures ($\sim 500^oC$) on a Pt buffer layer. In this case, the lattice misfit between FePt and Pt ($\sim 1.5\%$) relaxes through the pileup of $a/6\,\langle 112 \rangle$ partial dislocations along $[111]$ planes, leading to the formation of microtwins [87, 83].

+ FePt film can be directly grown on MgO substrate(100). In this case, the strain relaxation process due to the lattice misfit between FePt and MgO($\sim 10\ \%$) occurs by the creation

of a dense lattice of dislocations at the interface between the MgO substrate and the FePt layer [88, 86] relaxing in a few atomic layers.

To avoid current passing through the large buffer layer, we choose the second type of FePt layers. We focus here on studying magnetization reversal of 10 nm thick FePt films deposited directly on single crystal MgO (001) substrate (*cf.*, fig. 2.1b). The detail description of experiment process is given in the appendix A. These layers possess a very high perpendicular anisotropy ($K_u \sim 5.10^6\ J/m^3$), which results on a magnetic configuration composed of perpendicularly magnetized domains separated by a Bloch-type DW. The disorders and defects in these layers arise either from local change in the chemical ordering of the $L1_0$ phase or from crystal relaxation due to the misfit between the FePt lattice parameter and that of MgO substrate.

2.1.2 Magnetization reversal of a single FePt thin film

Following the layer growth, the magnetization reversal process of as-deposited samples were studied using macroscopic EHE and polar Kerr microscopy measurements. Hysteresis loop of 10 nm thick FePt was studied by EHE at room temperature using the lock-in technique with an external field applied perpendicularly to the layer. As showed in fig. 2.2a, the hysteresis loop of the FePt layer exhibits a square loop with full magnetic remanence. The coercivity of 10 nm thick FePt films are around 0.4 T. The square hysteresis loop indicates that the magnetization state is unchanged from high fields collinear to the magnetization down to the value of the negative field corresponding to the magnetization reversal. It emphasize that there is no change in the magnetization when the applied field is reduced to zero fields. This allows the observation at any intermediate states of the reversal process at zero field using magnetic microscopes.

The high coercive field and the fullness of the magnetic remanence in such layers imply (*cf.,* fig. 2.2a) that the DWs are tightly pinned on defects. Structural studies showed that the strain relaxation process occurs by the creation of a lattice of dislocations at the interface between the MgO substrate and the FePt layer [85]. These defects could interact with DWs through magnetoelastic coupling. It has been showed by numerical simulations [88] that the anti-phase boundaries can also pin efficiently the DWs in FePt layers.

In the following, the magnetization reversal of the FePt thin films is studied by polar Kerr microscopy (cf., fig. 2.7b). The magnetic domain structure is imaged in a remnant state after applying field pulses. The sample is initially saturated in one direction by a strong field ($\sim$ 1.5 T), we then apply a sequence of field pulses in the opposite direction to create a partially reversed state of magnetization. Fig. [2.2b presents the typical domain configuration occurring during magnetization reversal. The Kerr image shows that the reversed domain ("white" domain) expands by DW propagation. Note that the white domain is connected.

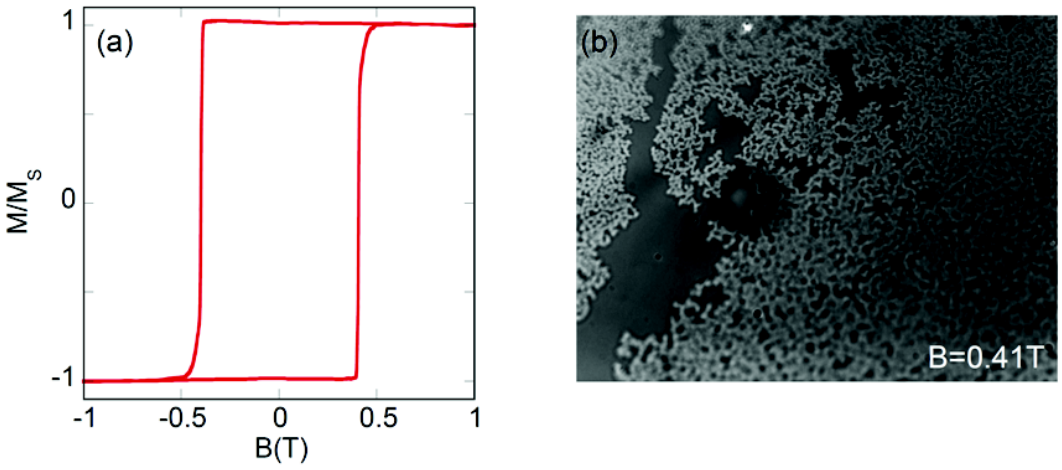

Figure 2.2: (a) Room temperature hysteresis loop measured in perpendicular field using EHE. (b) Polar Kerr microscopy image of a 10 nm thick FePt in partially reversed state showing that the reversed domains grows with dendritic structures. The sample was initially saturated by a negative field, the domain structure is obtained after applying a field pulse of 0.41 T with a pulse duration of 7 μs. The reversed domain appears in "white" domain. The size of Kerr image is 170×130 μm^2.

This means that all the white domain could originate from a single nucleation center. Furthermore, there can be large unreversed areas, which imply that the distance between nucleation centers is much larger than 100 μm. As seen previously [89], the structure of the reversed domain leads to fractal configurations.

Based on the model of invasion percolation without trapping (IPWT) [90], Attané *et al.*, [89] demonstrated that this fractal geometry of magnetic domain does not depend on the structure of the lattice (quasi-square lattice of structural defects for FePt/Pt: microtwins or isotropic defects distribution for FePt/MgO: dislocation or antiphase boundaries), it is part of a universality class process.

Basically, this model can be simply described as the schematic in fig. 2.3. The formation of structural defects during epitaxial growth process in FePt sample can be characterized by a distribution of numbers corresponding to the strength of defects, "N" corresponds to the nucleation center for the reversed domain.

At large scale, it is considered that the disorder strength is much larger than the exchange and demagnetizing fields. For a given applied field, only a portion of the sites (those for which $B(t) + h_i > 0$ where h_i is the random static field and B_t is the uniform field that drives the domain growth [89] can be reversed ("white" part). Consequently, in IPWT problem [90], the pressure and the resistance to fluid invasion can be replaced, respectively, by the magnetic field and the local coercivity values h_i. Note that the invasion percolation process occurs without trapping. Indeed, and contrarily to the initially proposed case of two incompressible fluids, in a magnetic layer a trapped unreversed domain, *i.e.*, an unreversed domain surrounded by

a reversed domain can be reversed if the magnetic field increases (*cf.*, fig. 2.3b) [89]. The reversed domain growth directions are basically selected as the easiest paths for the motion of the DW, which try to get around the defects possessing the highest pinning strengths (cf., fig. 2.3c,d). Therefore, the generated percolating cluster is similar to those obtained in standard percolation.

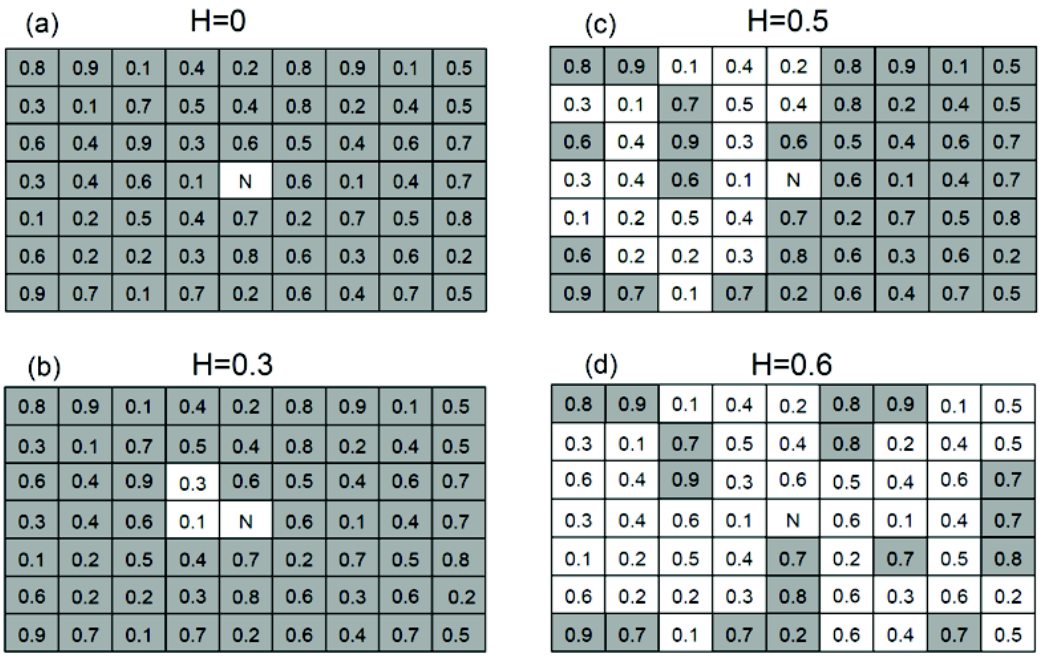

Figure 2.3: Schematic of an invasion percolation without trapping (IPWT) model to explain the magnetization reversal mechanism in FePt sample. The set of number corresponds to the strength of local coercitive field, "N" corresponds to the nucleation center. The "white" part is reversed domain and "grey" part is unreversed domain. One can see that the reversed domain propagates in the direction of the easiest paths when increasing applied field. For example: (a) Without reversal at H=0. (b) H=0.3, reverses the parts connected with the nucleus having a local coercivity lower than 0.4. (c) Reversal for H=0.5. (d) Finally H=0.6 reverses half of the layer by avalanche.

Further study using simulation, Attané *et al.,* [89] also elucidated that the fractal structures are qualitatively similar to the experimental results at large scale. At short distance, the effect of the demagnetizing field is found to be crucial, creating the dendritic pattern, *i.e.,* small unreversed domain embedded in the reversed domain that is observed in fig. 2.2b. However, for the large distance, the measurement of the fractal dimension of the reversed domain showed that properties of the percolating cluster are not influenced by the demagnetizing field.

2.1.3 FePt based spin valve thin film on MgO substrate

Recently, there has been a dramatic increase in the interest towards application of GMR and MTJs with perpendicular anisotropy in the field of spintronics, such as a spin transfer switching [91], magnetic random access memory and ultra high density magnetic information devices [92]. This interest is due to the fact that the systems with perpendicular anisotropy are expected to provide high thermal and magnetic stabilities. Therefore, this will allow the realization of small size devices, highly valuable for spintronic applications [93].

Basically, the effects of GMR require to stabilize a magnetic configuration in which the magnetization of two layers are anti-parallel. This anti-parallel configuration can be obtained using the exchange coupling with an antiferromagnetic layer [94], the exchange coupling between neighboring magnetic layers through the RKKY interaction [95], or simply using materials with different coercitive fields. This part will briefly present the properties of spin valve based on FePt with a Pd spacer. We show that the anti-parallel state is extremely stable by varying the nucleation fields of the two FePt electrodes layer. This is an important result for next studies of this thesis concerning the dynamic of DW propagation in spin valve based nanowires.

As shown in ref. [76, 86], by changing the Pt spacer layer to Pd with lower spin orbit coupling can improve slightly the amplitude of the GMR. Taking into account the advantage of this study, several spin valve structures FePt/Pd/FePt with different thicknesses of Pd have been deposited on MgO substrate using MBE. Both FePt layers, 5 nm thick, were grown by co-deposition of Fe and Pt at 500 ^oC, the Pd spacer with thickness ranging from 2 to 3 nm being grown at a lower temperature 330 ^oC to avoid the diffusion of Fe in the Pd layer.

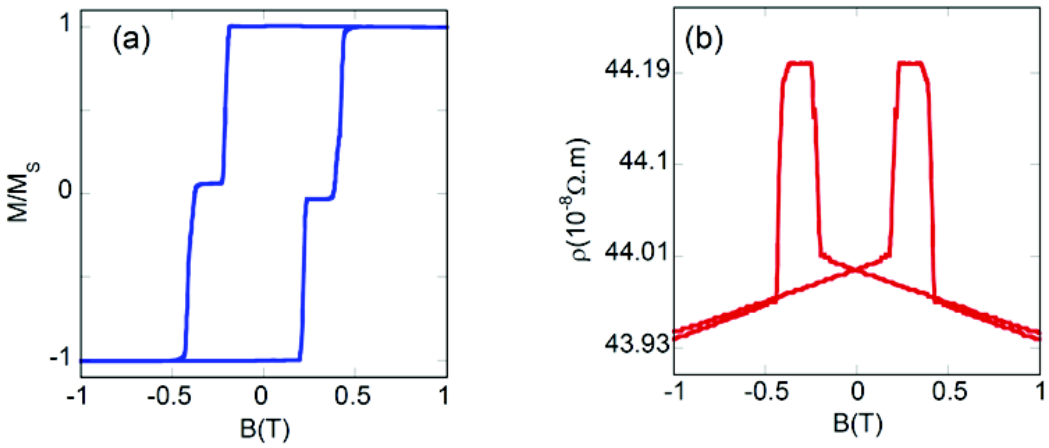

Figure 2.4: (a) EHE and (b) GMR measurement of spin valve FePt(5 nm)/Pd(2.4 nm)/FePt(5 nm) layer at room temperature.

Following the sample fabrication, we carried out EHE and GMR measurements at room temperature using the lock-in technique, with an external magnetic field applied perpendicularly to the layer. Fig. 2.4a shows an example of EHE measurement of the structure with 2.4

nm Pd, the separation of the coercitive fields (*i.e.*, $B_C \sim 0.2$ T for the soft layer and 0.4 T for the hard layer) revealing the AP configuration of the two FePt electrodes as evidenced by a large plateau in the curve. As a result of the AP configuration, the GMR effect is consequently obtained. GMR measurement of the sample with 2.4 nm Pd is plotted in the fig. 2.4b. The GMR curve shows a large plateau corresponding to a higher resistance in the AP state. The resistance increases sharply when the soft layer is reversed. This is followed by a decrease in resistance when the hard layer is reversed in turn.

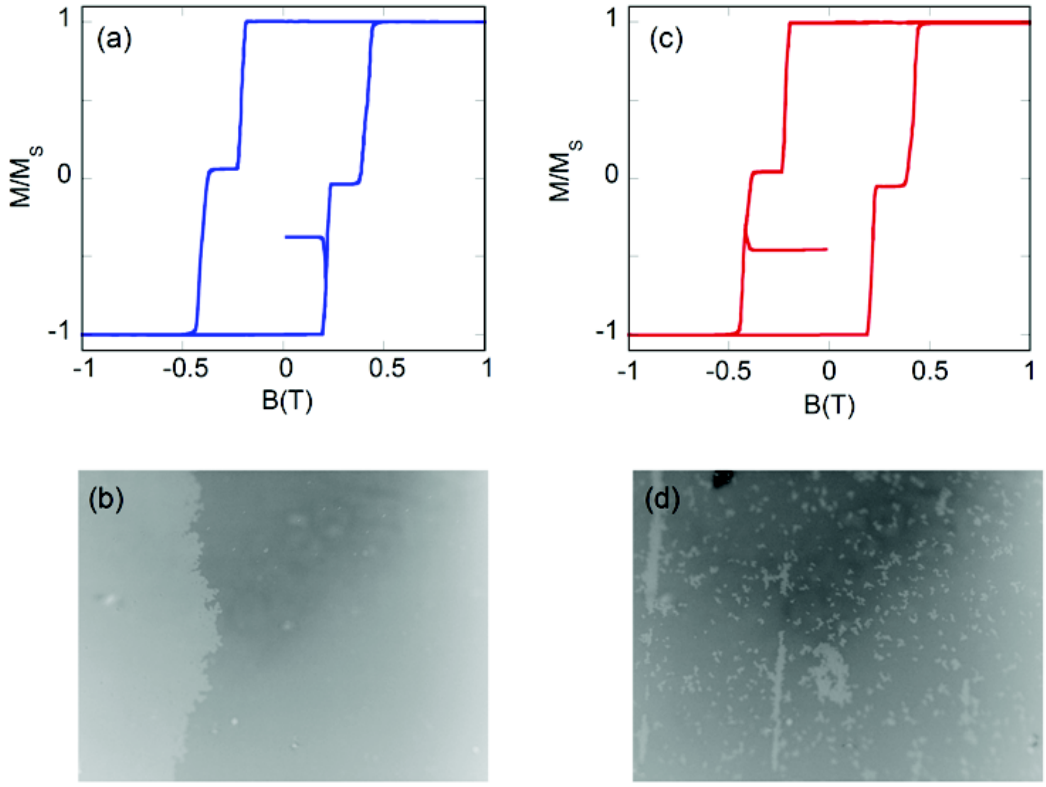

Figure 2.5: Major and minor hysteresis loop of FePt(5nm)/Pd(2.4nm)/FePt(5nm) spin valve for (a) soft layer and (c) hard layer. The direct observation of the magnetization reversal process using Kerr microscopy measurement for soft layer (b) and hard layer (d). The reversed domain is white. The size of each MOKE image is 170×130 μm^2.

Interestingly, in this study, two different coercivities are obtained for similar thicknesses of two FePt electrodes. In order to understand the origin of this different coercitive field, we studied the magnetization reversal process of the two FePt layer using polar Kerr microscopy (*cf.*, fig. 2.5). Thanks to the high magnetic anisotropy, the magnetization of FePt layer can be stable when the applied field is reduced to zero fields as shown in the minor loop of EHE measurements (*cf.*, fig. 2.5 a, c). This specific properties of FePt layer allows the observation of intermediate states during the reversal process. As proposed in the previous part, the magnetization reversal of FePt layers occurs by nucleation of reversed domains and

propagation of DW in which the DW is pinned on defects [89]. Kerr microscopy allows imaging both FePt layer thanks to the thin overlayer and spacer.

Kerr image in partial reversal state of soft layer in fig. 2.5b shows that the reversed domain ("white domain") is connected and expand with a dendritic structure. As it has been observed previously in single FePt layers, this suggests that the nucleation is extrinsic and rare. Then it is followed by propagation of the DWs on the whole surface. Whereas, in the case of the hard layer (*cf.*, fig. 2.5 d), a large number of nucleation sites are observed revealing that the propagation field is higher than the intrinsic nucleation field. Both FePt layers contain a number of interfacial and structural defects, *i.e.*, interfacial dislocations, antiphase boundaries, microtwins and so on that act as pinning sites for DW motion [89]. The value of the coercitive field in the FePt layers is found in the balance of several factors such as chemical ordering, anisotropy, and pinning strength.

We suggest that the difference in the coercive fields between the two FePt layers originates either from the variation in the type and density of the pinning defects in the different layers or from a lower anisotropy of the bottom electrode.

This lower anisotropy might be due to the high misfit between the FePt and the MgO substrate ($\sim$ 10 %) and the subsequent difficulty to obtain a high chemical order. Thus, an AP state of the two electrodes, even for similar thicknesses ratio of the two electrodes can be obtained.

In order to optimize the spin valves, we study structures with various thicknesses of the Pd spacer so that a magnetic decoupling could be achieved without depolarizing the electrons passing through it. In order to improve the GMR, the thickness of the spacer has been reduced down to almost the thickness limit below which no AP state can be stabilized.

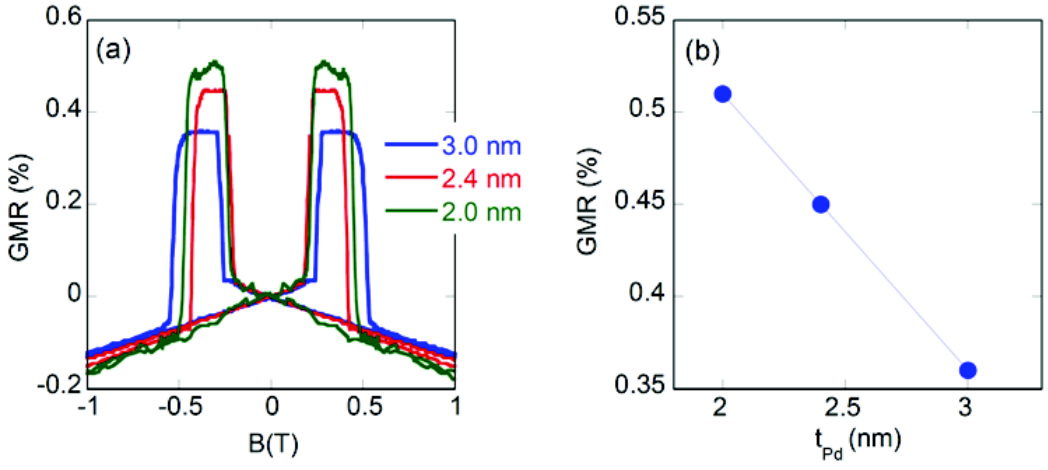

Figure 2.6: (a) GMR measurement of FePt based spin valve layer with different thickness of Pd spacer and (b) thickness dependence of the amplitude of GMR.

An example of an GMR measurement of spin valve structure with different thickness of Pd

is shown in fig. 2.6. The highest value of GMR is obtained ($\sim 0.5\%$) for the case of 2 nm Pd spacer and this is decreased down to 0.35 $\%$ when increasing the thickness to 3 nm (*cf.,* fig. 2.6b). The sample with highest GMR will be used for nanofabrication process for next studies concerning the DW propagation in nanowires.

2.2 Magnetization reversal of FePt based nanowires

Recent progress in nanofabrication allows creating structures whose dimensions get smaller than characteristic lengths of magnetism. Novel properties can thus arise when crossing spin-dependent transport lengths (*e.g.,* the spin-diffusion length [96]), micromagnetic lengths (*e.g.,* the exchange length, DW width), or microstructural lengths (*e.g.,* the distance between defects). In particular, the magnetization reversal, which has to be controlled thoroughly, is known to be very sensitive to the dimensions and aspect ratio of the nanowires [97, 98]. Moreover the technological implementation of DW based spintronics devices, such as DW-RAM memories, motivates the control of the magnetic properties at wire widths of 30 nm or smaller in order to compete with actual technology node.

This part will present the dimensionality effect on magnetization reversal modes of FePt nanowires. For this purpose, we have studied the magnetization reversal in wire of widths ranging from 2 μm to 30 nm. We show that the reversal process of FePt nanowires can be determined by the comparison of the wire dimensions with four characteristic lengths: the dendrite width, the disorder length, the mean edge roughness and the nucleation distance [81].

We first show that the magnetization reversal modes vary from the growth of a dendritic structure to the propagation of a single DW when reducing the wire width below than the dendrite width. Secondly, we show the enhancement of the coercitive field at low sizes which are mostly attributed to the suppression of the available paths for DW propagation [80]. An invasion percolation model, as well as simulations, is proposed to describe this coercivity enhancement. Additionally, the mean edge roughness is also found to contribute to the increase of coercivity in narrow nanowires. Finally, we show that the coercivity increase leads to the decrease of the nucleation distance which results in a mix of nucleation and DW propagation during magnetization reversal.

2.2.1 Effect of magnetic dendrite width on the magnetization reversal mode of FePt nanowires

The first characteristic length which affects the magnetization reversal modes of FePt nanowires is the dendrite width, which can be defined as the mean width of the magnetic domains appearing during the reversal. In our experiments, we observed the dendritic structure of the

domains of 10 nm thick FePt/MgO(001) films which are chemically ordered in the L_{10} phase. As analyzed in Kerr images above (*cf.,* fig. 2.2b), at large scale, the demagnetizing energy is much smaller than the disorder strength, the reversed domains are known to lead to fractal configurations. At low scale, in partially reversed zones, the reversed domain grows in dendritic structures, *i.e.*, existence of small unreversed domain embedded within the reversed domain. Basically, the effect of the demagnetizing field is found to be crucial since it is responsible for the dendritic pattern [89]. Indeed, at the short distance, the demagnetizing energy becomes relatively strong in comparison with DW energy. The growth of reversed domain is thus dominated by the geometry of the pinning centers in the equilibrium conditions.

In the following, we observe the dendritic growth of the reversed domain at low scale using Magnetic Force Microscopy (MFM). Fig. 2.7a presents the major and minor hysteresis loops of the FePt layer measured by EHE at room temperature.

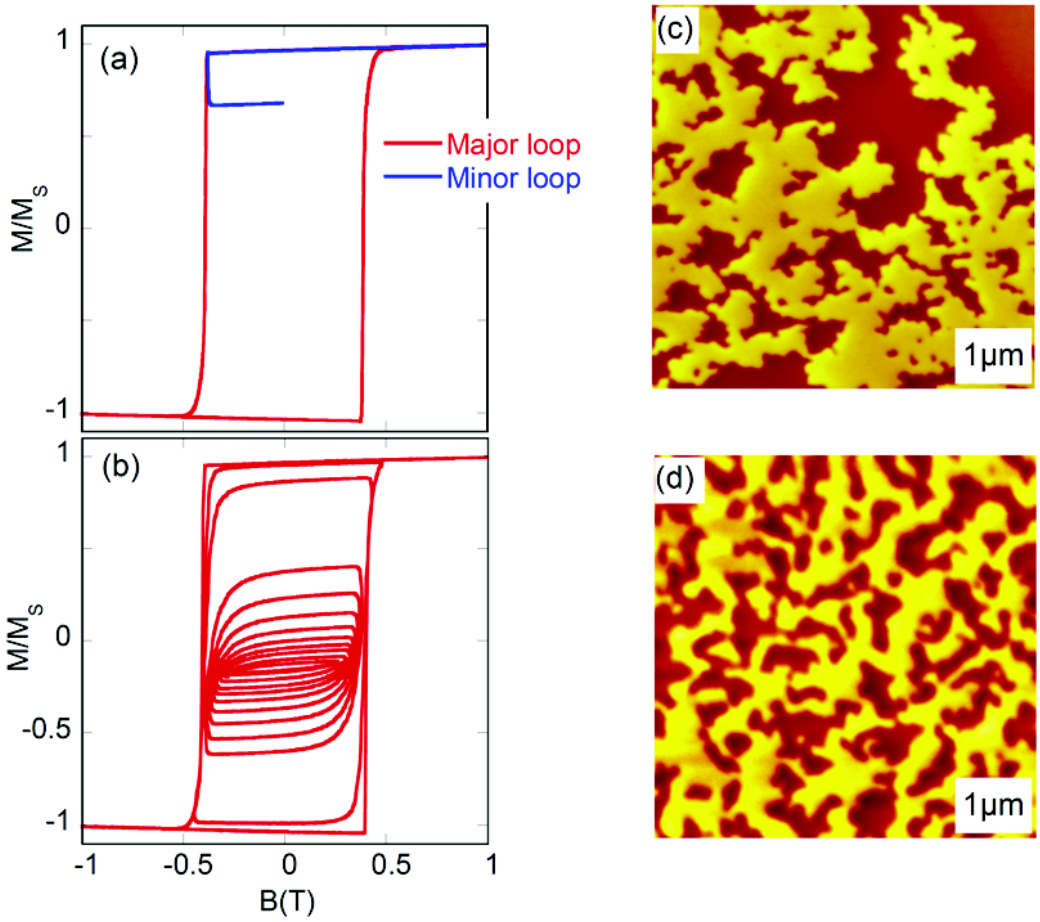

Figure 2.7: (a) Major and minor hysteresis loop of a 10 nm thick FePt thin film, measured by EHE. (c) 5μm $\times$ 5μm MFM image observed in a partially reversed magnetic state after realizing the minor loop. (c) Hysteresis loop corresponding to the demagnetization of the layer, done in order to obtain a magnetic state as close as possible to the equilibrium magnetic state. (d) 5 μm $\times$ 5 μm MFM image obtained at zero field after the demagnetizing process.

For an external field applied perpendicularly to the layer, the magnetic hysteresis exhibits a square loop and a full remanence at any stage of the magnetization reversal. Fig. 2.7c shows the MFM image obtained in a partially reversed state ($M/M_S \sim 0.7$) after realizing the minor loop of fig. 2.7a. The reversed domain ("white domain") is connected and exhibits a dendritic structure.

The mean width of these dendrites is about 300 nm. This dendrites width is basically close to the equilibrium domain width, which is determined by the competition between demagnetizing field energy and DW energy. Note that the equilibrium configuration is difficult to obtain in these strongly remanent layers. A quasi-equilibrium state of magnetization can be obtained using a demagnetization process in an oscillating field of decreasing amplitude (*cf.*, fig. 2.7b) [99].

The domain width estimated using this process and measured by MFM (*cf.,* fig. 2.7d) is around 260 nm. This value is also close to the width of the domains in an as-deposited sample (w=200 nm), which corresponds also to a near-equilibrium state.

Note that contrarily to the equilibrium domain width, the dendrite width is also affected by the disorder. Indeed, in our layers, the strong disorder can distort the DW: previous analysis of the fractal configurations of magnetic domains in these layers [89] showed that the DW elasticity is weak in front of the pinning disorder. In material with strong disorder, the competition between DW elasticity, demagnetizing field and disorder can lead to a characteristic dendrite width slightly larger than the equilibrium DW width, as the disorder prevents DW propagation. Following the layer growth, nanowires have been prepared by means of e-beam lithography and ion milling techniques (*cf.*, appendix A), of widths ranging from 2 μm to 30 nm. As seen in fig. 2.8a, a large magnetic area at one end of the wire acts as a DW reservoir that allows injecting a single DW into the 15 μm long wires. A magnetic coil is used to apply 7 μs long perpendicular field pulses that reverse the magnetization. The MFM observations are then realized at zero field. At the beginning of the experiment, the magnetic structure is saturated by a strong perpendicular field. Field pulses are applied to introduce a DW into the wire.

Fig. 2.8b shows MFM images of partially reversed wires for widths above 500 nm (first three MFM images in fig. 2.8b). The structure of the reversed magnetic domains appears to be similar to those of the layer (*cf.*, fig. 2.7c): small non-reversed parts (in dark) remain embedded inside the reversed domain (in white). The existence of such non-reversed areas is basically due to the phenomena creating the dendritic structure in the thin films, *i.e.*, demagnetizing field effect and selection of the easiest paths by the DW [89, 100].

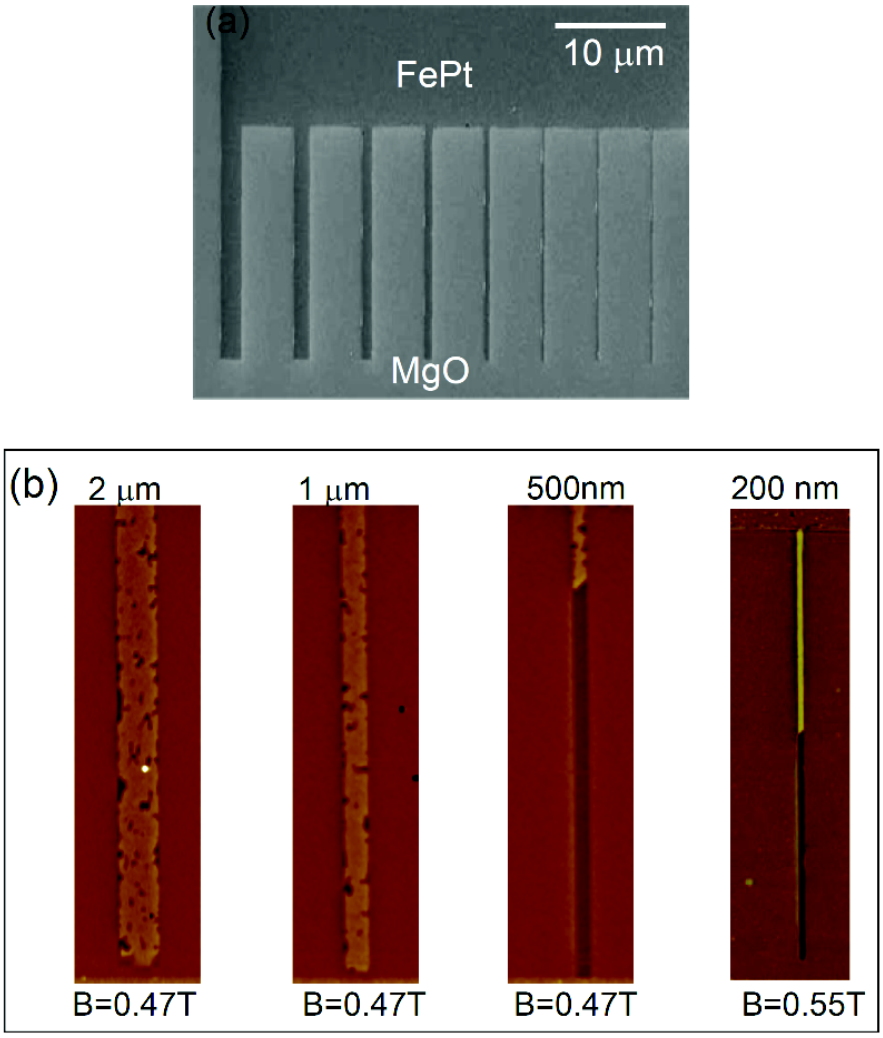

Figure 2.8: (a) SEM image of the nanodevice used for MFM observations, with a nucleation pad connected to wires of various widths, ranging from 2 μm to 150 nm. (b) MFM observations of various wires showing that the reversal mode changes with the width of the wires: above 500 nm, the wire is not completely reversed, and there remains unreversed domains (dark parts). For 200 nm wide wires, the complete reversal occurs by propagation of a single DW: the reversed part is entirely white.

When decreasing the widths of the wires below 500 nm, the magnetization reversal takes place by the motion of a single DW which reverses the whole wire magnetization. As an example, fig. 2.8b (last MFM image) shows the propagation of a single DW along a 200 nm wide nanowire. The characteristic length associated to this transition between partial and full reversal is basically the average width of the dendrites observed during the reversal of the continuous film. Reducing the width below the dendrite width, we can get a single DW propagation along the nanowire which is important for future studies of this thesis.

2.2.2 Enhancement of coercive field in FePt nanowires

This part will show the enhancement of coercive field when reducing the wire width. Basically, the characteristic length linked to coercivity enhancement is the disorder length, which is the mean distance between pinning defects. A simple computation has been realized to describe the DW propagation process which is based on the percolation model. Finally, we show that the mean edge roughness of the wire also contribute to the coercivity enhancement in such narrow nanowires.

2.2.2.1 Experimental observation of coercivity enhancement in FePt nanowires

In our experiments, the coercivity is measured using magneto-transport measurements. Nanowires are here again prepared by E-beam lithography, a second lithography step being used to create Ti/Au electrical contacts, and Hall crosses are disposed along the wires. Fig. 2.9a shows an optical microscopy image of FePt nanodevice for magnetotransport measurements. A low scale SEM image of Hall cross in fig. 2.9b shows that the edge roughness is smaller than 10 % of the width, even for 30 nm wide Hall crosses.

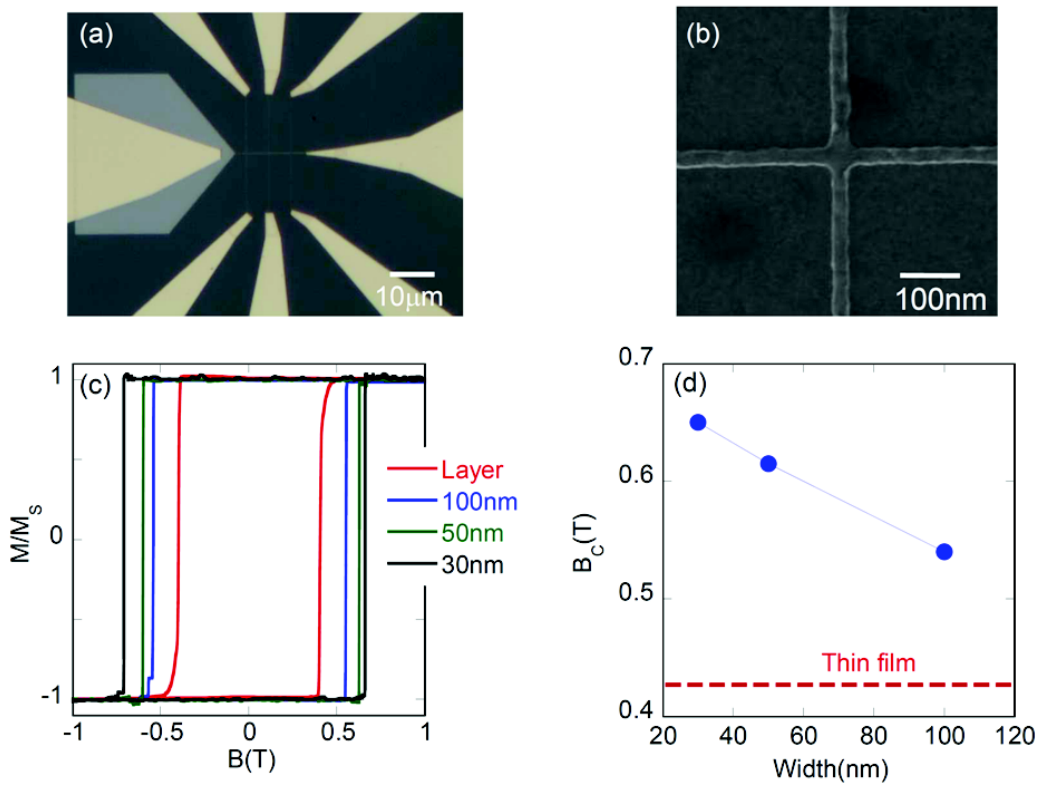

Figure 2.9: (a) Optical microscopy image of 50 nm wide FePt nanowire with a set of Au contacts for magneto-transport measurement and (b) SEM image of the 30 nm wide Hall cross. (c) EHE loops measured in perpendicular field of a FePt thin film and of 100, 50 and 30 nm wide FePt Hall crosses. (c) Coercivity dependence with the width of FePt nanowires.

Perpendicularly magnetized systems give rise to high EHE and the Hall voltage is proportional to the perpendicular component of the local magnetization within the cross. Such EHE measurement allows detecting precisely the value of the switching field of a single nanodevice. In this measurement, a small ac current ($J = 2.10^9\ A/m^2$, $f = 1023\ Hz$) is injected along the wire. The voltage drop is measured using the lock-in technique at room temperature. The EHE measurements for different wire widths in fig. 2.9c show that all hysteresis loops are squared, and that the coercivity is gradually increased when reducing widths. It is found that the switching field increases with decreasing width, from 0.4 T to 0.68 T for the continuous layer to 30 nm wide, respectively.

Coercivity enhancement for low widths have already been reported and discussed in both systems with planar and perpendicular magnetization [*e.g.,* [101]]. As discussed in details in ref.[80] for larger wires (w>200 nm), the coercivity increase in L_{10} FePt nanowires can be partly attributed to the suppression of the available paths for DW propagation. The defects of the layer induce a distribution of local pinning fields. The DW somehow follows the easiest path during its propagation, which means that it gets around the defects with higher pinning strengths. For small wire widths, the number of available paths for the DW is geometrically reduced: the DW can not get around the strongest defects. As a result, to reverse narrow wires the DW has to cross the defects possessing the largest pinning strengths, which leads to an increase of the coercive field. To give qualitatively account of this phenomenon, the width of the wire has to be compared to the characteristic length of the disorder, below which the DW has to cross all defects sequentially.

2.2.2.2 Modeling the enhancement of the coercivity in FePt nanowire

Taking into account similar magnetic behavior between both FePt/Pt and FePt/MgO system as presented in previous part, we use the invasion percolation model [80] to describe the coercivity enhancement in FePt/MgO based nanowires. In the case of FePt/Pt system, the existence of a quasi-square lattice of structural defects, namely microtwins [87], is responsible for the magnetic coercivity. Based on the percolation model proposed in ref. [102], but applied in this case to describe the confinement of the DW, we can qualitatively give account of the observed phenomena. The nanostructures are described as perfect two-dimensional square lattices, each side of a cell corresponding to one microtwin.

In the case of FePt/Pt sample, the size of the cells which obtained by AFM [87] corresponds to an average distance between microtwins of ∼70 nm. This is physically the length scale to which the width of the cross has to be compared. The disorder corresponds to the distribution of the propagation fields of the microtwins. Previous AFM observations made in [102] provided the distribution of sizes of microtwins (*i.e.,* the number of dislocations that created each microtwin), which is spread out. It is difficult to accurately extract the correspondence between

the size of a microtwin and its pinning field using micromagnetic simulations [88, 102].

However, we can assume that the field distribution, like the microtwin size distribution, is spread out. It is limited to positive fields, as there can be no depinning at negative fields, and by a maximal field H (corresponding to the biggest microtwins). Also, in the proposed model, the median field of the distribution corresponds to percolation and is thus equal to the coercitive field of the layer [89]. For simplicity, propagation fields are assumed to be uniformly distributed between 0 and 1. Each microtwin can be represented as a bond between two adjacent cells. At a given applied field, each link can be blocking or nonblocking, depending on its associated propagation field, and a nucleation center is set in one branch, far from the cross. When the applied field increases, blocking bonds become nonblocking, allowing the reversed domain to spread on the neighboring cells, always choosing the path of least resistance.

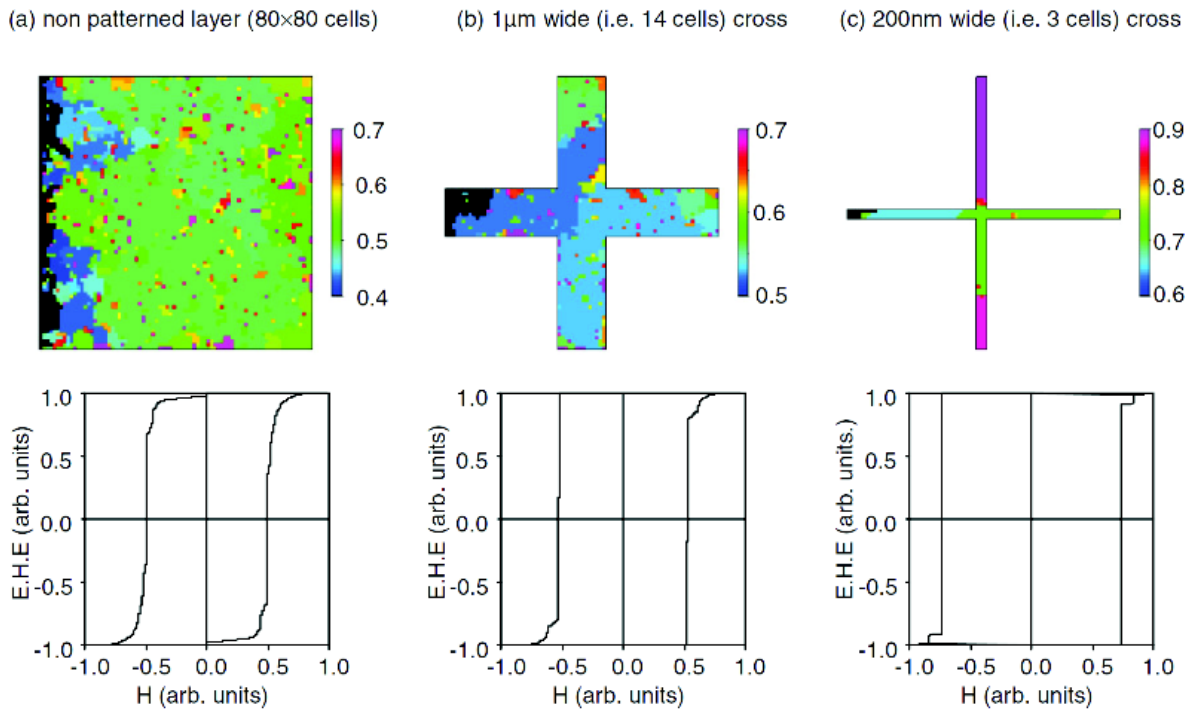

Figure 2.10: Results of computations based on an invasion percolation without trapping model. The top row shows the reversal process in crosses of different widths, where (a) corresponds to a continuous layer. Each pixel corresponds to an elementary cell delimited by four microtwins. The scale of colors indicates the field at which the pixel was reversed: dark blue pixels were reversed at low fields, and red and purple pixels were reversed at higher fields. Larges zones of uniform color were reversed by avalanches. The number of avalanches in the cross diminishes with the cross width, and they mainly occur in the branches. The smaller cross (c) is nearly completely reversed by a single avalanche. In the bottom row, the corresponding hysteresis loop for each panel's top image is shown as it would appear if measured by EHE. When going toward small dimensions, the reversal is sharper, and the coercitive field increases [80].

This description is an invasion percolation without trapping problem [90] in a lattice of bonds, which describe the displacement of one fluid by another fluid in a porous medium. In the original version of this percolation problem, bonds represent throats between pores and are of random sizes, whereas in our case bonds correspond to defects of various pinning strength. In our computations, the reversal occurs from a nucleation center located in one branch of the cross. The Hall effect sensitivity function [103] is taken into account: the cells'contributions are summed up to calculate the total Hall voltage. When increasing the applied field from negative values, the DW is blocked in the branch, progressing by avalanches, until an avalanche reverse a large part of the cross, inducing a large jump of magnetization in the cross. Then, the remaining cells are reversed progressively. Results of these simulations are shown in fig. 2.10, which presents the reversal modes of a nonpatterned thin layer and a cross of various widths, with the corresponding hysteresis loops. For the nonpatterned thin layer, or when the width of the branches is large (1 μm; *i.e.*, 14 cells), the cross is partially reversed at a field close to $H_P = 0.5$ (*i.e.*, 50% of defects can be crossed; (*cf.,* Fig. 2.10a, b), which corresponds to the percolation threshold in a square lattice of bonds. The hysteresis loop thus consists in a steep reversal followed by a slow saturation, as was observed experimentally. When reducing the width, the number of available propagation paths is limited. As the path is imposed, the DW gets blocked by microtwins whose pinning fields are larger than H_P, which accounts for the observed increase of the coercitive field in small crosses. Finally, the biggest defect of the path of least resistance is crossed, and a huge avalanche reverses the whole cross, as can be seen in fig. 2.10c. This explains the amplitude of the sudden magnetization reversal at the coercitive field, which is experimentally bigger for smaller crosses.

To give qualitatively account to this phenomenon, the width of the wire has to be compared to a length characteristic of the disorder, below which the DW has to cross all defects sequentially. In first approximation, this disorder length is close to the distance between pinning defects. In the lattice models proposed above, this disorder length would be the microtwin lattice parameter, whereas in a continuous model, where a pinning field is associated to each point of the layer, the relevant length would be the correlation length of the pinning field. In any case, this disorder length is difficult to measure precisely, however, structural and magnetic observations suggest [88, 80] that it is in these layers of a few tens of nanometers. This simple picture can simply explain the increase of coercivity of our sample as the wire width is decreased taking into account that natural pinning center are always present in our wires as observed in dynamic measurement.

2.2.2.3 Contribution of the mean edge roughness to the coercivity

After the dendrite width and disorder length, the third important length scale which can effect on the magnetization reversal mode of FePt narrow wires is the mean edge roughness of the

wire, which is below 5 nm in our 30 nm-wide wires. In ref. [80], which concerned wires wider than 200nm, it was shown that roughness effects could be neglected. However, when the width of the wire gets close to the edge roughness, the total length of the DW has to change strongly during its propagation. As the process of extending the DW costs surface energy, the roughness can contribute to the coercivity. For a given roughness, this increase is supposed to scale with $1/W$, W being the width of the wire. It has been shown [48] that in a simple 2D model, a straight wall moves in direction x of the wire, the roughness being represented by fluctuations of width $W(x)$ of the wire. The coercivity increase due to the roughness can be written:

$$\triangle H = \frac{\sigma}{2M_S W}\left(\frac{dW}{dx}\right)_{max}$$

where $\sigma = 4\sqrt{AK}$, A, K, M_S are DW areal energy, exchange energy, anisotropy constant and saturation magnetization, respectively. W is width of nanowire, $(dW/dx)_{max}$ is the tangent of the maximal angle made by the edges with the longitudinal direction. With $\sigma = 23.10^{-3}\ J/m^2$, M_S=1030.10$^3 A/m$. The limitation $\frac{dW}{dx} < 0.2$ can be estimated from SEM observations of the 100 and 30 nm wide nanowires.

Note that this 2D model assumes that the DW width $\sqrt{\frac{A}{K}}$(∼1 nm in our samples) is much smaller than the width of the wire. Based on this model, we can estimate that the additional coercivity due to the roughness is 0.02 T for 100 nm and 0.07T at 30 nm wide wires. These values are smaller than the observed coercivity increase, probably because it is mostly due to the suppression of propagation paths; however the roughness contribution to the coercivity is no longer negligible as it was for nanowires much wider than the mean edge roughness.

2.2.2.4 Effect of nucleation distance on the magnetization reversal modes in narrow FePt nanowires

The last important length scale which can change the magnetization reversal mode in narrow FePt nanowires is the nucleation distance, *i.e.,* the mean distance between nucleation centers. Indeed, for very narrow widths, a new behavior of magnetization reversal appears, involving a mix of DW nucleation and propagation. The reversal is no longer associated to the propagation of a single DW, as new nucleated domains appear within the wires. This can be seen in MFM images of 40 and 30 nm wide FePt (*cf.,* fig. 2.11), showing the presence of several reversed domains along the nanowires.

This phenomenon is due to the decrease of the nucleation distance with the applied field. Basically, to each point of a magnetic thin film can be associated a nucleation field. The distribution of these nucleation fields is known to be spread: for example, if small pulsed fields are applied to a continuous layer, there are usually few nucleation centers. On the contrary,

if short pulsed fields larger than a few Tesla are applied, any small defect within the layer is expected to behave as a nucleation center (*e.g.*, [104]). In this case, the nucleation density is large and thus the nucleation distance is small.

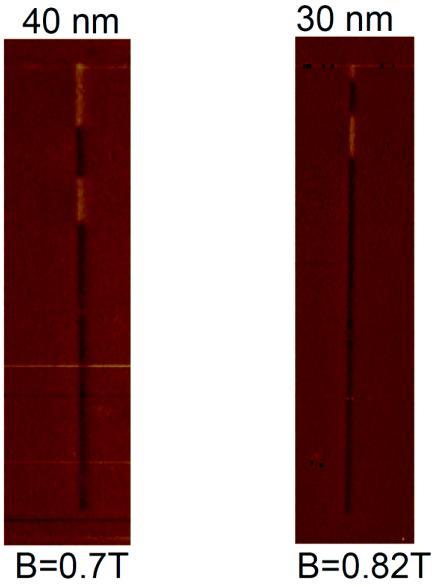

Figure 2.11: MFM observation of the nanowires with the widths smaller than 50 nm. In both case, one white domains nucleated along the wires.

The dependence of the nucleation distance with the applied field is also relevant in the case of nanowires. When the wire is large, the wire is reversed by the propagation of a single DW created in the pad, and the switching field corresponds to the propagation field of the DW. When the wire gets narrower, the propagation field increases. The probability to find some new nucleation site within the wire increases, because the characteristic distance between nucleation centers at higher field becomes smaller than the length of the wire. Then, the reversal consists of a mix of nucleation and DW propagation, which might prevent the use of such ultra-small wires for DW based spintronic devices: further decrease of nanowire width requires more homogeneous samples with few extrinsic nucleation centers.

Conclusions

In this chapter has been shortly presented the growth of FePt thin film on MgO substrate using MBE. Magnetization reversal of such layer showed that at large scale the structure of reversed domain leads to fractal configuration which was described by invasion percolation without trapping model. At the short distance regime, the effect of the demagnetizing field is found to be crucial, creating the dendritic pattern.

We also demonstrated that spin valves effect can be obtained using FePt material with high perpendicular anisotropy, without conventional antiferromagnetic pinning layer. A high CIP-GMR amplitude has been found at room temperature in the optimized structures, thanks to the different reversal field of the two FePt layers.

We have studied the magnetization reversal of FePt nanowires with perpendicular magnetization, for width down to 30 nm. The results show that in perpendicularly magnetized systems, the magnetization reversal mode is strongly dependent on the dimensions of the nanowires. Below the dendritic width, magnetization reversal occurs by propagation of a single DW that reverse the whole volume of the wire. Decreasing the width towards the disorder length and/or the mean edge roughness leads to a large increase of coercivity. This coercivity increase is associated to a decrease of the nucleation length, which can become prohibitive for applications if it gets smaller than the wire length. Note that there exist materials in which the role of structural defects and/or demagnetizing field is weaker (CoNi, CoFeB...). The DW is then smoother, with a bubble-like growth. By tuning carefully the microstructure of the layer, a weak dispersion of the pinning fields can be achieved, in order to push the scalability of DW-based devices towards ultimate sizes. This weak dispersion should indeed lead to longer disorder lengths, which would partly avoids the increase of coercivity at low widths, and the associated decrease of the nucleation distance. Still, we anticipate that in sub-50 nm nanowires DW elasticity and edges defects should lead to an increase of propagation fields, and to the appearance of the mix of propagation and nucleation.

Chapter 3

Detection of magnetization reversal in FePt nanowires using Magnon magnetoresistance

In this chapter, we demonstrate that the detection of magnetization reversal for nanostructures can be achieved using magnon magnetoresistance (MMR), *i.e.,* the contribution of magnons to the resistivity [105]. Following a short description on the observation of MMR in FePt thin film with high perpendicular anisotropy, we will show that MMR can be used to dectect magnetization reversal in nanostructures, including the detection of DW position and DW motion along a nanowire. Finally, we show that a contribution of Hall resistance appears in a four probes longitudinal resistance measurement when a DW is located within two contact probes.

3.1 Observation of Magnon magnetoresistance in FePt thin films

Magnon is the quasi-particles associated to spin waves, *i.e.,* small amplitude magnetic excitation, as phonons are for the lattice vibrations. The dispersion relation of magnon has a quadratic form, with an energy gap proportional to the effective magnetic field felt by the magnons:

$$E(k) = Dk^2 + g\mu_B B_{eff} \tag{3.1}$$

where D, μ_B and g are the material-dependent exchange stiffness constant, the Bohr magneton and the Landé factor, respectively. When the magnetization and the applied field are parallel, an increase of the applied field induces a shift of the dispersion curve towards

higher energies, and consequently a decrease of the magnon population. This phenomenon can be simply described: when the applied field increases, the spin lattice becomes more rigid, and the magnon population thus decreases. In 2002, Raquet *et al.,* showed that up to high fields ($\sim 30\ T$), the resistivity of *3d* metallic layers decreases linearly with the applied field. They related this effect to the decreasing number of electron-magnon diffusion events [106]. In previous study [107, 86], Mihai *et al.*, pointed that in FePt thin layers, the huge anisotropy field ($\sim 10\ T$) is associated to a large gap in the dispersion relation. At zero applied field, the dispersion curve is thus shifted by the anisotropy field. When an external field is applied parallel to the magnetization, this field adds to the anisotropy field, shifting the dispersion curve towards higher energies and decreasing the resistivity. Due to the high anisotropy and coercivity of FePt sample, a configuration in which the applied field is anti-parallel to the magnetization can be stable. In such anti-parallel state, the applied field subtracts to the anisotropy field: the dispersion curve is shifted towards lower energies, hence increasing the resistivity. Therefore, at a given field, the resistivity depends on the orientation of the magnetization relatively to the field: this property is at the heart of the MMR. One part of this thesis focus on studying the change of resistance during magnetization reversal in nanostructures. We will show that such MMR measurement can be used as a tool to study quantitatively the magnetization reversal in nanostructures.

Experimentally, 10 nm thick FePt thin film deposited on MgO substrate using MBE. As presented in detailed in the chapter 2, this film is chemically ordered within the L_{10} structure and the magnetization reversal is dominated by DW propagation rather than DW nucleation. In the following, EHE and MR measurements have been carried out using an external magnetic field applied perpendicularly to the layer. Magnetotransport measurement configurations are schematically shown in fig. 3.1a. The EHE hysteresis loop in the fig. 3.1b reveals a square loop and perfectly separates two states of magnetization. The corresponding longitudinal MR measurement is presented in the fig. 3.1c. Obviously, fig. 3.1b and 3.1c show that above saturated state, the magnetization is stable while the resistance evolves linearly with the applied field in both magnetically saturated and remanent states. At the coercitive field, the resistance is abruptly reduced of about 0.2 % in both positive and negative half loops. Note that this MR curve shows a different behavior from that of AMR effect. Indeed, AMR shows that above the saturation the resistance is constant with the applied field. Also, in this measurement configuration, the applied current is always perpendicular to the magnetization within magnetic domain and there is consequently no AMR contribution.

As demonstrated by Raquet *et al.*, the linear dependence of resistance in the magnetic saturate state is due to spin-wave damping in high fields, which corresponds to a decrease of the intrinsic spin disorder [106]. Increasing the applied field leads to the lowering of the magnon population and thus of the resistivity.

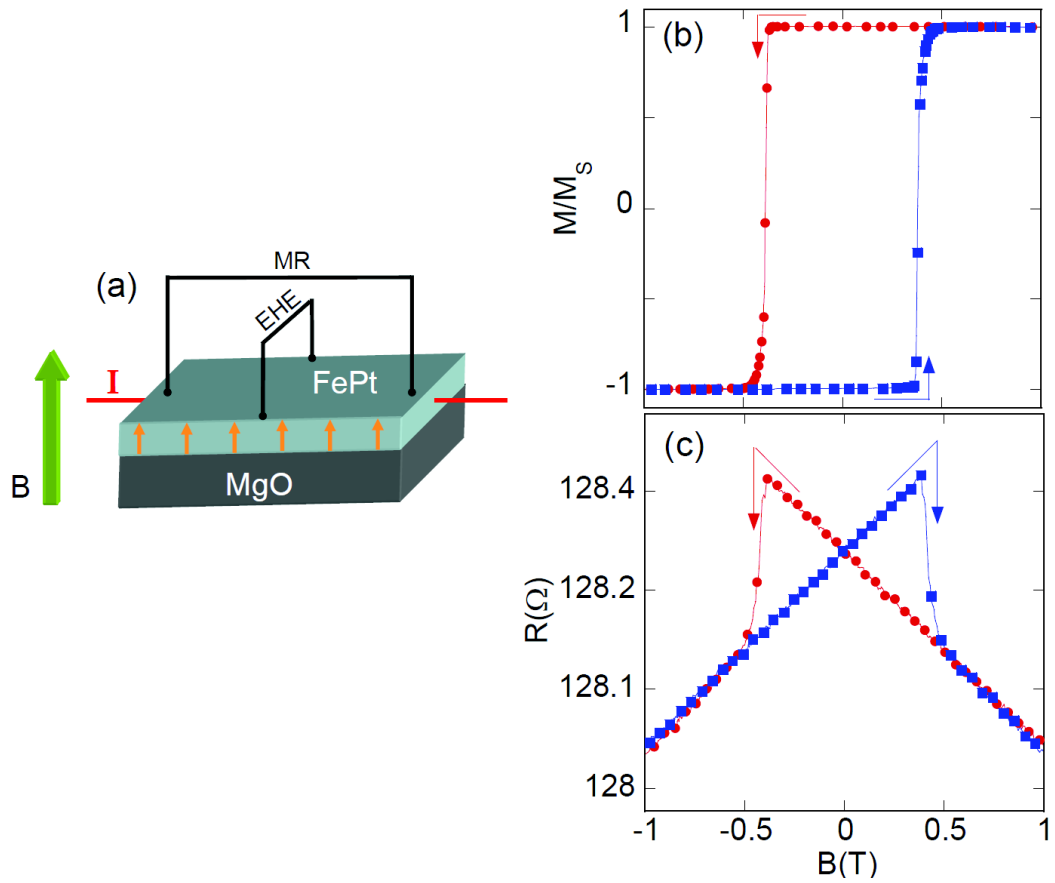

Figure 3.1: (a) Schematic of EHE and MR measurements configuration of the FePt thin film deposited on MgO substrate. (b) Room temperature EHE hysteresis loop and (c) MR measurement in perpendicular field of a 10 nm thick FePt thin film.

Interestingly, in our FePt layers with high perpendicular anisotropy, the linear dependence of resistance with the field is preserved in the remanent state where the direction of magnetization and applied field are anti-parallel. Indeed, in the anti-parallel configuration, the anisotropy field tends to maintain the magnetization direction, while the applied field tends to destabilize it, increasing the magnon population and the resistivity. At the coercive field, the magnetization switch from one state to the opposite one. The magnetization and applied field thus switch from an anti-parallel to a parallel configuration. This results in an abrupt change of the magnon population and consequently to a drop of resistivity (*cf.*, fig. 3.1b,c).

Previously, Mihai *et al.*, [107, 86] also confirmed the magnon origin of this resistivity by measuring temperature dependence of this effect. As expected from theoretical model of electron-magnon scattering [106], the effect decreases and finally disappears when decreasing the temperature to very low values. Here, we mainly study how the MMR can be used to detect the magnetization reversal in nanostructures.

The MMR curve reveals two interesting features. Firstly, the sharp decrease of resistance corresponds to the switching field, and secondly, the slope of $\rho(B)$ provides an information on

the magnetization orientation with respect to the applied field.

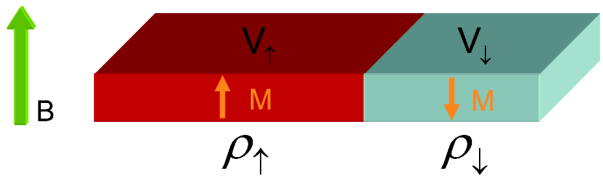

Figure 3.2: Schematic of MMR measurement in a partial reversed state. $V_\uparrow$, $V_\downarrow$ are the volume occupied by domain up and down. $\rho_\uparrow$, $\rho_\downarrow$ are the resisitivity of these domains.

We will now analyze qualitatively the change of resistance associated with the magnetization reversal when the magnetization proceeds by DW motion in systems with strong uniaxial anisotropy, *i.e.,* with two states of magnetization. As showed in the previous chapter, magnetization reversal in FePt layer occurs by nucleation of a few reversed domains, followed by DW propagation over the whole layer. Due the high anisotropy and hence to the large size of the involved domains, the contribution of the DW-related resistances can be neglected in a first approach. Thus, MR in a partially reversed state can be considered as due to two different contributions, arising from the reversed (*i.e.,* up domain) and unreversed domains (*i.e.,* down domain). It can be simply described in the schematic of fig. 3.2.

In the following, let us denote α the $\rho(B)$ slope taken in saturated state of magnetization ($\alpha < 0$), ρ_0 the resisitivity at zero field and B the applied along the direction of the anisotropy axis. The value of α can be easily obtained from MR measurements above saturation. In the parallel configuration (of applied field and magnetization), increasing the applied field leads to a decrease of resistance (the slope α is negative):$\rho_\uparrow = \rho_0 - \alpha B$. On the contrary, for anti-parallel configuration (remanent state), the slope is positive and $\rho_\downarrow = \rho_0 + \alpha B$. The global resistivity of the layer can be expressed as the average of up and down resistivities weighted by the volume fraction of the corresponding domains:

$$\rho = \frac{\rho_\uparrow V_\uparrow + \rho_\downarrow V\downarrow}{V_0} \tag{3.2}$$

where V_0 is the total volume of the sample ($V_0 = V_\uparrow + V_\downarrow$) decomposed in $V_\uparrow$ and $V_\downarrow$, the volume parallel and anti-parallel to the field, respectively.

On the other hand, the normalized magnetization of the layer corresponds to the volume fraction difference can be expressed as:

$$\frac{M}{M_S} = \frac{V_\uparrow - V_\downarrow}{V_0} \tag{3.3}$$

where M is the global magnetization along the anisotropy axis, M_S is the saturation magnetization. The volume covered by up and down domains are thus given by:

$$V_{\uparrow} = \frac{V_0}{2}\left(1 - \frac{M}{M_S}\right) \tag{3.4}$$

$$V_{\downarrow} = \frac{V_0}{2}\left(1 + \frac{M}{M_S}\right) \tag{3.5}$$

Based on this simple model, we can link the dependence of resistance on the magnetization by the following formula:

$$\rho = \rho_0 + \alpha \frac{M}{M_S} B \tag{3.6}$$

This formula underlines that MMR is proportional to the magnetization. In other words, such MMR measurement can give quantitatively access to the magnetization. The following section will show that MMR can be used to detect magnetization reversal in nanowires, in particular, to detect DW position.

3.2 Detection of magnetization reversal and domain wall position in FePt nanowires

3.2.1 Detection of magnetization switching in FePt nanowires

Following the layer growth, FePt nanowires have been prepared by means of e-beam lithography and ion milling techniques. A detailed description of the nanofabrication process is presented in appendix A. A representative optical microscope image of the device with a set of electrical contacts is showed in fig. 3.3a.

A large magnetic pad at one end of the wire acts as a DW reservoir that allows injecting a single DW into the wire from the same side. Fig. 3.3b shows an example of low scale SEM image of a typical FePt nanowire. Such a device allows simultaneous EHE and MR measurements.

To perform magneto-transport measurements, a small ac current ($J = 2.10^9 A/m^2$, $f = 1023\ Hz$) is injected along the wire. The voltage drop is measured using lock-in technique at room temperature.

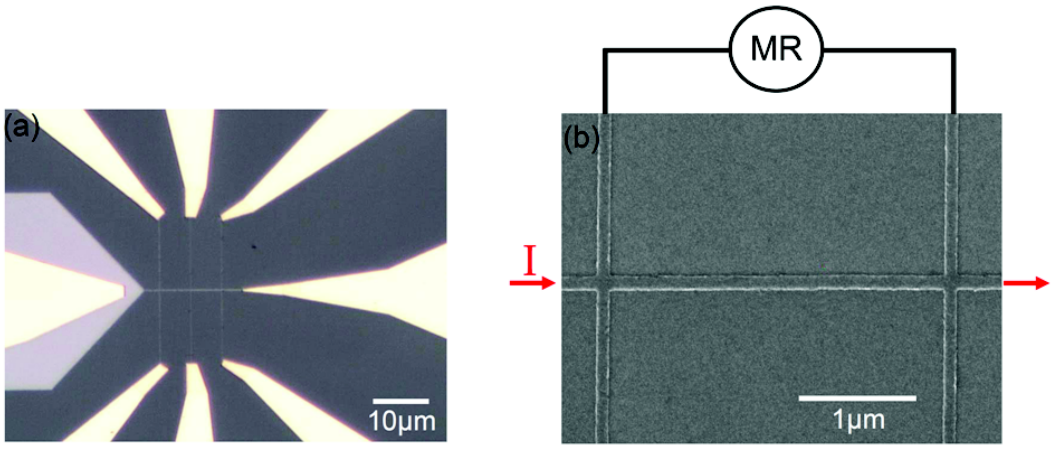

Figure 3.3: (a) Optical microscopy image of a FePt nanodevice, with a set of electrical leads designed to carry out magnetotransport measurements. A large magnetic area at one end of the wire acts as a nucleation pad, allowing injecting a single DW into the wire. (b) Representative SEM image of a 100 nm wide FePt nanowire, two Hall crosses are disposed along the $3\mu m$ long segment of the wire.

An example of EHE and MR measurements of a 50 nm wide FePt nanowires are showed in fig. 3.4. For applied fields perpendicular to the layer, the EHE hysteresis loop of Hall cross exhibits a square loop (*cf.*, fig. 3.4a), with a coercive field of about 0.6 T.

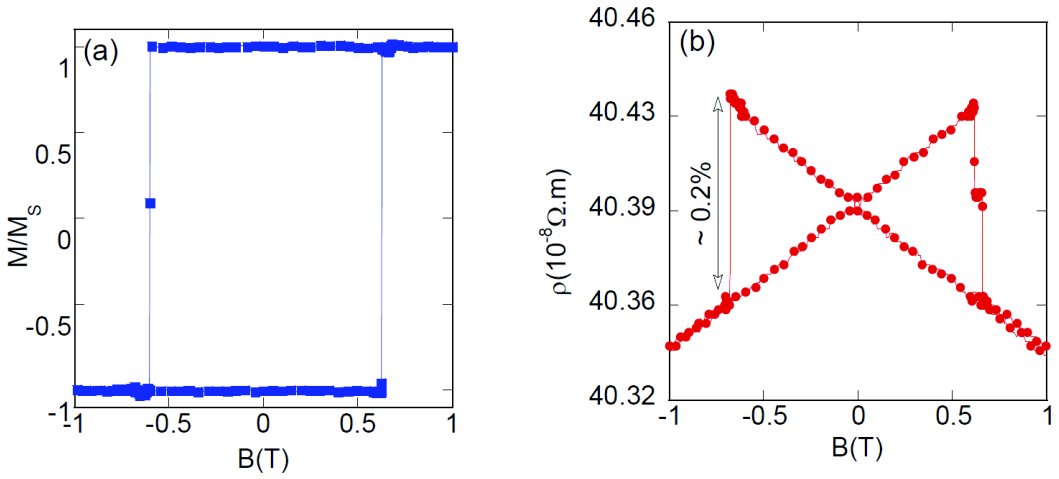

Figure 3.4: (a) EHE hysteresis loop of the 50 nm wide Hall cross and (b) corresponding MR in perpendicular field and at room temperature.

Fig. 3.4b shows the four-probe MR measurement of the 6 μm long nanowire located between two Hall crosses. It shows MMR can also be observed in 50 nm wide nanowire. As previously seen in FePt thin films, a drop of resistivity of 0.2 %, due to the abrupt change of magnon density, appears in both positive and negative half loops, revealing the magnetization switching of the nanowire. The obtained values of the switching field using EHE and MMR

measurements are well corresponding.

As seen above, the MMR signal is proportional to both the magnetization and the applied field. The amplitude of the MMR effect associated with magnetization reversal is thus null at zero field, and increases with the applied field. As a result, the magnetization reversal corresponding to large coercive fields will provide a higher signal. In the FePt case, where the coercive field is high, the MMR is about 0.2 %, which is easily measurable using lock-in techniques.

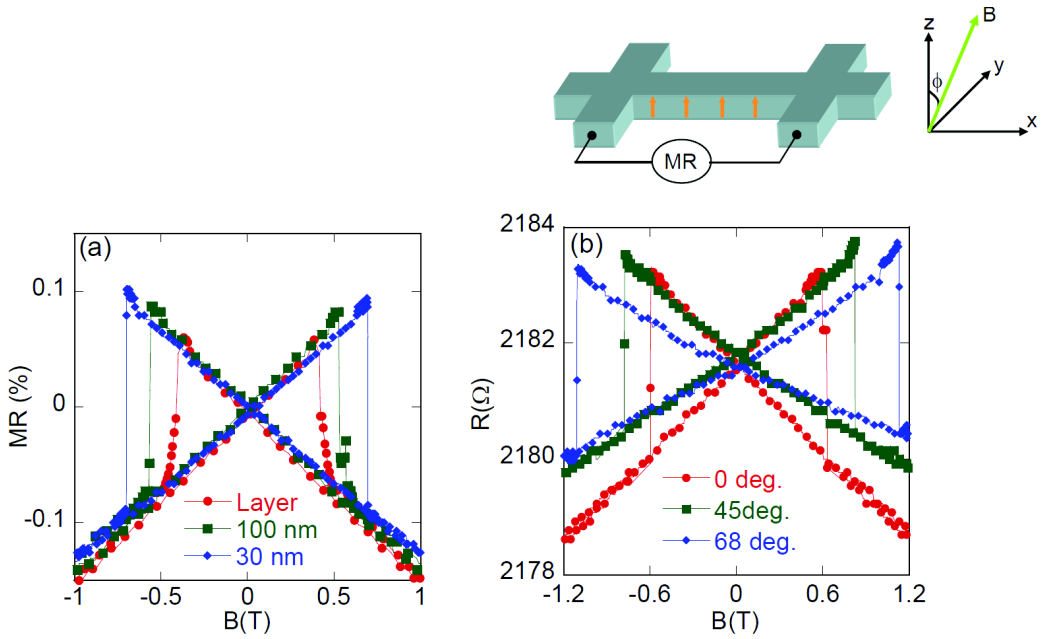

Figure 3.5: (a) MMR measurements in perpendicular field of a FePt thin film and of 100 and 30 nm wide FePt nanowires. (b) Schematic of MMR measurements configuration for different rotation of the applied field (ϕ) where the rotation plane belongs to the plane of the anisotropy field (yz plane) and always orthogonal to the wire axis to avoid AMR. (c) MMR measurement of 100 nm wide FePt nanowire with different angles.

The MMR measurement allows studying magnetization switching of FePt nanowires with different widths (*cf.*, fig. 3.5a). The obtained values of the switching field using MMR measurements for different wire widths are in agreement with EHE measurements as presented in the last chapter (*cf.*, fig. 2.9): the switching field increases with decreasing width, from 0.4 T for the full layer to 0.68 T for a 30 nm wide wire. Moreover, fig. 3.5b shows the MR measurement of a 100 nm wide FePt nanowire, for different orientations of the applied field. The curves show a gradual increase of the switching field from 0.6 T for 0° to 1.1 T for 68°. Measurements for the larger angles are not available because the switching field is higher than the field limit of our electromagnet. Note that the slope of MMR decrease when the applied field rotates from 0 to 68º. It is basically due to the fact that the strong anisotropy in FePt allows magnetization stay perpendicularly to the layer, then the projection of the applied field

on the magnetization is close to $cos(\phi)$, the effective field is decreased of $B_{ext.}cos(\phi)$ instead of $B_{ext.}$. So, a larger field is need to get the same effect as in the case of staying parallel to anisotropy plane. A simple analytic model to describe more precisely these measurements will be presented in appendix B. In any case, these MR curves show that the MMR effect can be used to detect the magnetization reversal for various field orientations, as the anisotropy is strong in comparison to the switching fields. Finally, note that MMR measurement detects the magnetization reversal of the whole wire, whereas EHE is sensitive to the reversal only within the Hall cross.

3.2.2 Measurement of domain wall position and motion along FePt nanowires

As shown in the chapter 2, from 200 down to 50 nm wide FePt nanowires, the magnetization reversal occurs by propagation of a single DW. This result is important for studying the detection of DW position and motion in this chapter.

We will now show that the MMR can be used to detect quantitatively the magnetization reversal of a nanowire, including the detection of DW position and DW propagation along a FePt nanowire [105]. According to Eq. 3.6, the MMR signal allows measuring the ratio $\frac{M}{M_S}$ which can be related to the position of the DW along the wire.

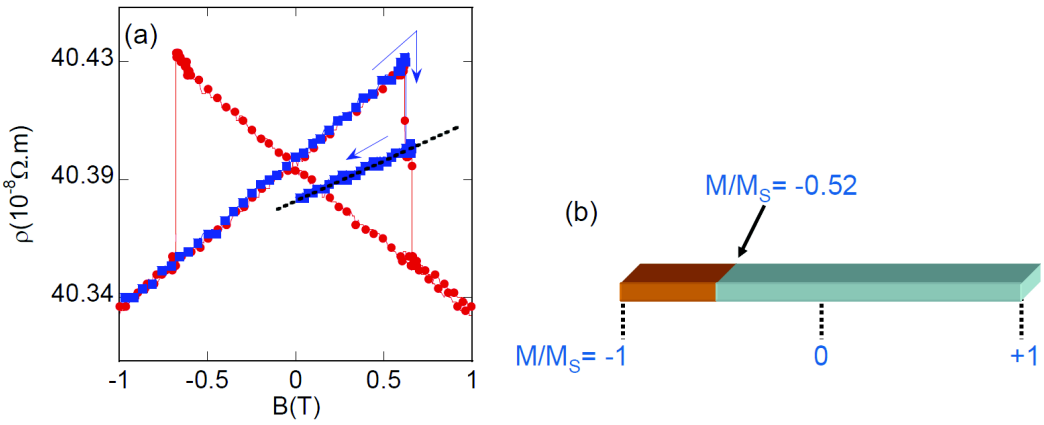

Figure 3.6: Detection of the DW position along a FePt nanowire. (a) Major and minor MMR loops. The wire is partially reversed at $+0.645$ T. The slope of the minor loop corresponds to $\frac{M}{M_S} \sim -0.52$, *i.e.*, to the reversal of around $24 \pm 1\%$ of the length of the wire. (b) Schematic showing the partial reversal of the FePt nanowire after measuring the minor loop, the reversed domain is illustrated in brown.

To confirm that hypothesis, a major MMR loop has been measured, followed by a minor loop in which a DW is introduced within the wire (*cf.*, fig. 3.6a).

As seen in the previous experiments [49], the DW gets pinned on a structural defect, which allows to go back to zero field without inducing DW motion. According to Eq. 3.6, the slope

of the minor loop $\left(\frac{\partial\rho}{\partial B}\right)$ during the return to zero field is equal to $\alpha\frac{M}{M_S}$ (α is the MMR slope in the saturated state). This results in a value of $\frac{M}{M_S} \sim -0.52$. In this field sweep direction, the ratio $\frac{M}{M_S}$ switches from -1 to +1, this value thus corresponds to the reversal of $24 \pm 1\%$ of the length of the wire (*cf.*, schematic illustration in fig. 3.6b)

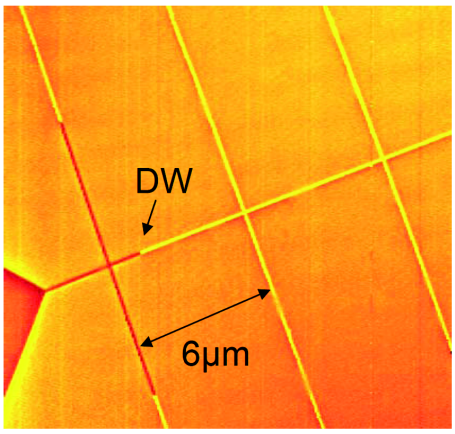

Figure 3.7: MFM image realized after measuring the minor loop showing that a single DW is located at around $23 \pm 1\%$ of the length of the wire. The reversed domain appears in dark brown.

To verify this result, we then measured the DW position using MFM. The MFM image in fig. 3.7 shows that a single DW is located at 1.4 μm distance from the first Hall cross which corresponds to the reversal of $23 \pm 1\%$ of the 6 μm long wire, in very good agreement with the MMR measurement.

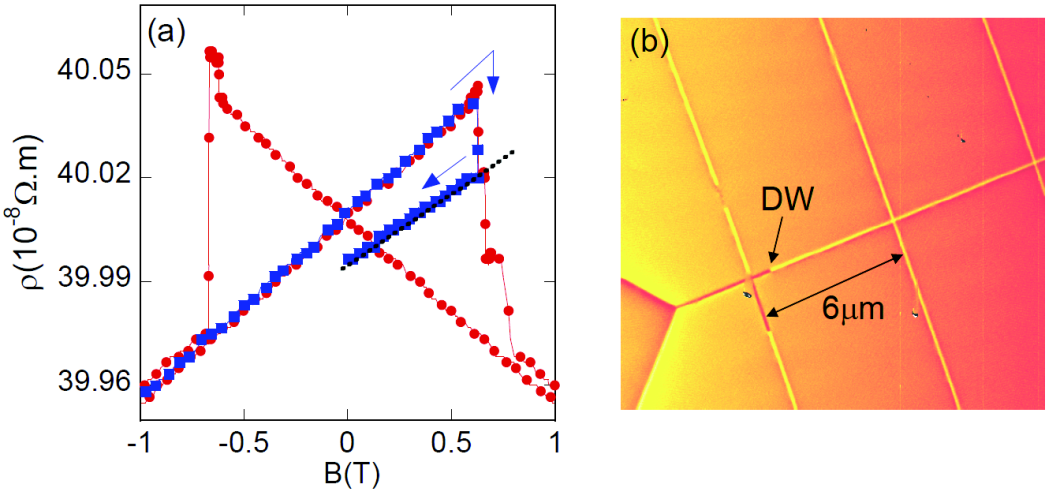

Figure 3.8: (a) Major and minor MMR loops. The slope of the minor loop corresponds to $\frac{M}{M_S} \sim -0.76$, *i.e.*, to the reversal of around $12 \pm 1\%$ of the length of the wire. (b) MFM image realized after measuring the minor loop revealing that a single DW is located at $13 \pm 1\%$ of the length of the wire.

In fig. 3.8, we show another example of the detection of the DW position for a different device. The slope of the minor loop leads to the value of $\frac{M}{M_S} \sim -0.76$, i.e., to the reversal of 13$\pm$ 1 % of the length of the wire. It is also in agreement with the observation of the DW position by MFM (cf., fig. 3.8b): the MFM image indeed shows a single DW located at 0.78 μm from the first Hall cross corresponding to the reversal of 13$\pm$1% of the6 μm long wire. These results clearly proved that the MMR allows measuring precisely the position of DW along nanowires.

As an example of application, MMR measurement can provide a way to investigate the dynamics of DW motion along a nanowire. In this measurement, the sample is initially saturated in a strong negative field (-1.2 T). A positive constant field (+0.65 T) is then applied to create a partial reversal of magnetization, and we simultaneously record the variation of the resistance as function of time. Fig. 3.9 shows the resistivity of a 50 nm wide FePt wire as a function of time and under a constant field.

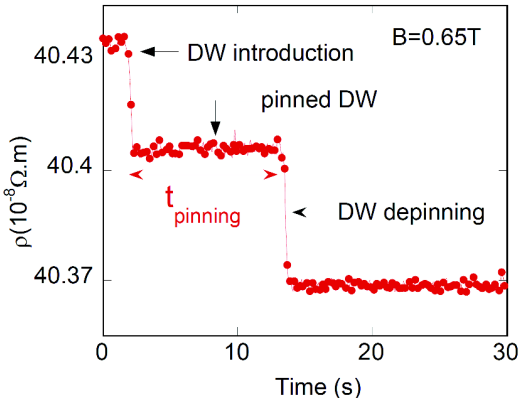

Figure 3.9: Resistivity of the nanowire as a function of time under a constant field

The first sharp decrease of resistance corresponds to the introduction and motion of the DW into the wire. It then gets pinned on a defect for a while, which correspond to the observed MMR plateau. The DW is finally depinned due to thermal activation, leading to the magnetic saturation of the wire. Such measurement allows extracting the pinning time of DW on the defect. This behavior is exactly similar to what was measured in ref. [33] using GMR, which emphasizes that MMR measurements provide, although with lower signals, the same information as TMR and GMR measurements [*e.g.,* [9, 108]]. However, MMR do not need an additional magnetic reference layer that may change the involved physics (DW dynamics, spin-transfer torque. . .) because of stray fields or spin accumulation effects [109, 110, 111]. Also, MMR obviously offers a more accurate description of the reversal than AMR, which only detect the presence of a DW in the nanowire, and EHE, which only detects the presence of the DW in the Hall crosses. The detailed study of DW dynamic will be discussed in chapter 5.

3.3 Hall contribution to the MMR measurement

The field dependence of longitudinal MR is expected to be symmetric with respect to the sign of the magnetic field while transverse Hall resistivity being asymmetric with respect to applied field. This part will show that an asymmetric contribution of resistance on the applied field appears in a longitudinal MR measurement when a DW is located between the voltage probes of the MR measurement.

3.3.1 Introduction

The asymmetric longitudinal MR behavior has been observed in several systems with perpendicular anisotropy as metallic thin films [112, 113, 114] or ferromagnetic semiconductors [115, 116].

As an example, Cheng *et al.*,[112] showed that the asymmetric behavior appears in longitudinal MR measurement of Co/Pt thin film when a single DW is located between the voltage probes. They suggested that the effect was due to the electrical fields generated by EHE which have opposite polarities on both sides of the DW, which can produce a circulating current loop at vicinity of the DW and resulting in an additional voltage contribution. According to their analysis, the resistance arising from the nonuniform current around the DW varies, depending on the position of DW between the two probes (the maximum resistance is attained when the DW is located at center of the two probe voltages).

Based on another experiment, Segal *et al.,* [113] claimed that a non-uniform variation in the Hall voltage along the sample arising from the variation of thickness, Hall coefficient, and non-uniform magnetization reversal generates an additional asymmetric signal in longitudinal voltage. For the systems with perpendicular anisotropy, this additional signal becomes significant due to a large change of the Hall voltage at the magnetization reversal.

However, most experiments or the theoretical analysis have been studied on the large thin film samples or microdevices. In such systems, the distribution of current lines is complicated which make the precise understanding the phenomenon more difficult.

In this part, we show that in the case of narrow nanowires with perpendicular magnetization, this asymmetric behaviour which appears in longitudinal MR measurement arise from EHE. This is due to the different magnetization orientation within two contact probes. It does not depend on the position of DW within the probes (each voltage probes giving an additional Hall voltage).

3.3.2 Asymmetric signal in longitudinal MMR measurement

Fig. 3.10 shows a SEM image of 50 nm wide FePt Hall cross and the corresponding EHE hysteresis loop of Hall crosses. As expected, the transverse Hall resistance appears with an asymmetric behavior with respect to the applied field.

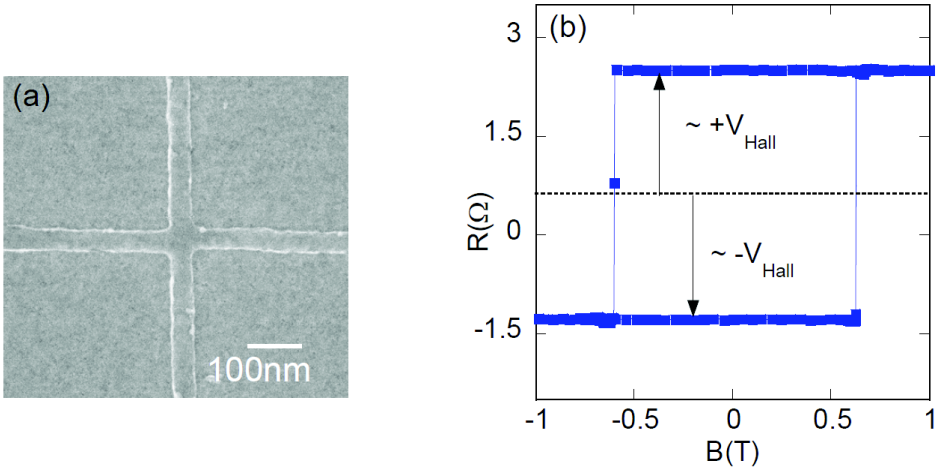

Figure 3.10: (a) Representative SEM image and (b) corresponding EHE measurement of 50 nm wide FePt Hall cross.

In the following, we show in fig. 3.11a major and minor MMR loop of 50 nm wide FePt nanowires between contact 1 and 2 (*cf.*, fig. 3.11b). As analyzed in the previous part, the slope of the minor loop $\left(\frac{\partial \rho}{\partial B}\right)$ allows measuring the value of $\frac{M}{M_S} \sim -0.84$, corresponding to the reversal $8 \pm 1\%$ the length of the wire.

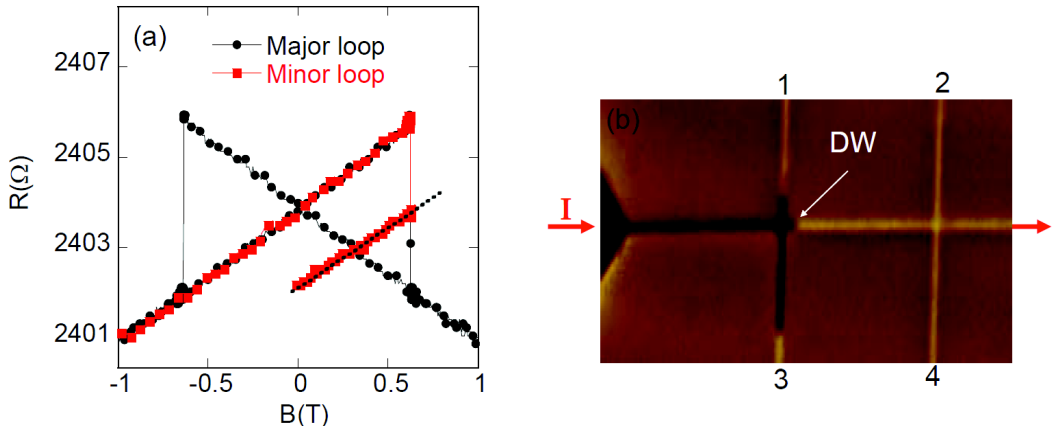

Figure 3.11: (a) Major and minor MMR loop of a FePt nanowire, the voltage being probe between contacts 1 and 2. The minor loop corresponds to a partially reversed state at $+0.64$T and shows an offset resistance at zero field. (b) MFM image after realizing the minor loop reveals a single DW located at $7 \pm 1\%$ of the length of the wire.

This value is in agreement with the MFM image in Fig. 3.11b. The MFM image shows

that a single DW is located at $0.21\ \mu m$ of the first Hall cross, which corresponds to the reversal of $7 \pm 1\%$ of the $3\ \mu m$ long wire.

We will now analyze the existence of an offset of resistance at zero field during the minor loop. Indeed, according to the eq. 3.6, the MMR signal is proportional to both the magnetization and the applied field, it means that the resistance should be always the same at zero field. However, the minor loop in fig. 3.11a shows that there exists an offset resistance ($\sim -1.9\Omega$) at zero field. We emphasize that this does not prevent using the MMR to detect DW position because the DW position only depends on the slope of the minor loop.

To elucidate this behaviour, we measured the minor loop (between contacts 1 and 2) in the opposite direction of the applied field as displayed in the fig. 3.12a. In this case, the slope of the minor loop allows measuring the value of $\frac{M}{M_S} \sim +0.86$ (with this field sweep direction, the ratio $\frac{M}{M_S}$ switches from $+1$ to -1), corresponding to the reversal of $7 \pm 1\%$ the length of the wire. This means that in both cases, the DW position being given by MMR slope is the same. There also exist an offset resistance ($\sim +2.2\Omega$) at zero field but here it is positive. Moreover, the polarity of these offset resistances is also reversed (*cf.*, fig. 3.12b) if the longitudinal MR measurement is performed along the opposite side of the wire (*i.e.*, measurement between contacts 1 and 2 compare to 3 and 4 (*cf.*, fig. 3.11b)).

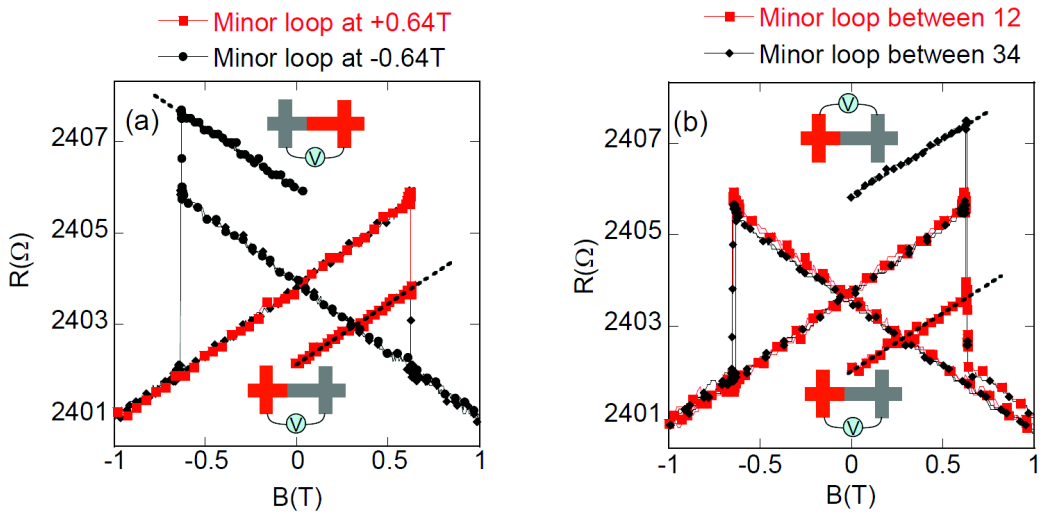

Figure 3.12: (a) Major and minor loop of MMR measurement probed between contacts 1 and 2. The minor loops correspond to a partially reversed state in the both signs of applied field. They show an opposite polarity of the offset resistance. (b) The minor MMR loops are recorded along opposite side of the wire (red curve is probed between contacts 1 and 2 and black curve between 3 and 4) also showing an opposite polarity of the offset resistance.

On the contrary to what was previously reported [112, 116], this asymmetric behaviour is found to be independent on the position of DW between two contact probes. As an example, fig. 3.13 shows the same effect for another device where a DW is located at 24 % of the length

of the wire. To understand such behavior in nanowires, we show in the following a simple model to explain the existence of an asymmetric signal in longitudinal MR measurement.

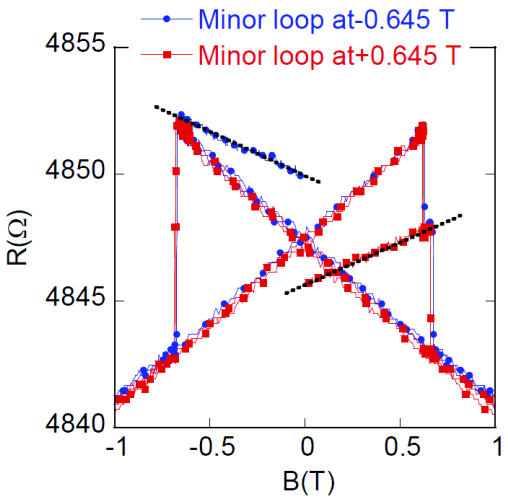

Figure 3.13: The minor loops of 50 nm wide FePt nanowire in the both signs of applied field showing an opposite polarity of the offset resistance. In this measurement, the slope of minor loops correspond to the location of a DW at 24 % of the length of the wire.

3.3.3 Model of Hall contribution to MMR measurement

In our measurement configuration, the current is applied along the nanowires. The interpretation of the measurements can be schematically illustrated in the fig. 3.14. In the saturated state (*cf.,* fig. 3.14a), the electrical field generated by the EHE is oriented in the same direction in the whole wire. The longitudinal MR measurement exhibits thus a symmetrical behavior, as seen from the major MMR loop of fig. 3.11a (black curve). However, the presence of a DW between the two voltage probes will separates the device into two domains of opposite magnetization (*cf.,* fig. 3.14b). As a result, the electrical field in one of the contacts points now in the opposite directions. For example, if one measures the EHE of the Hall cross in one side of the DW, *i.e.,* with the up domain $(+M)$, the EHE signal will be proportional to $+M$. Whereas, if measuring in the cross on the other side of the DW, the EHE signal gives an opposite result, being proportional to $-M$. In this case, the longitudinal MR measurement between two contacts probes having different magnetization orientation will deviate from the value measured in the saturated state. In one cross, the additional voltage in MR measurement is thus half of Hall voltage in EHE measurement. The contributions in the two contacts add up when a DW is present and the voltage probes are on the same side of the wire. Then the total contribution of the EHE to the longitudinal measurement is equivalent to the voltage obtained in a single EHE measurement.

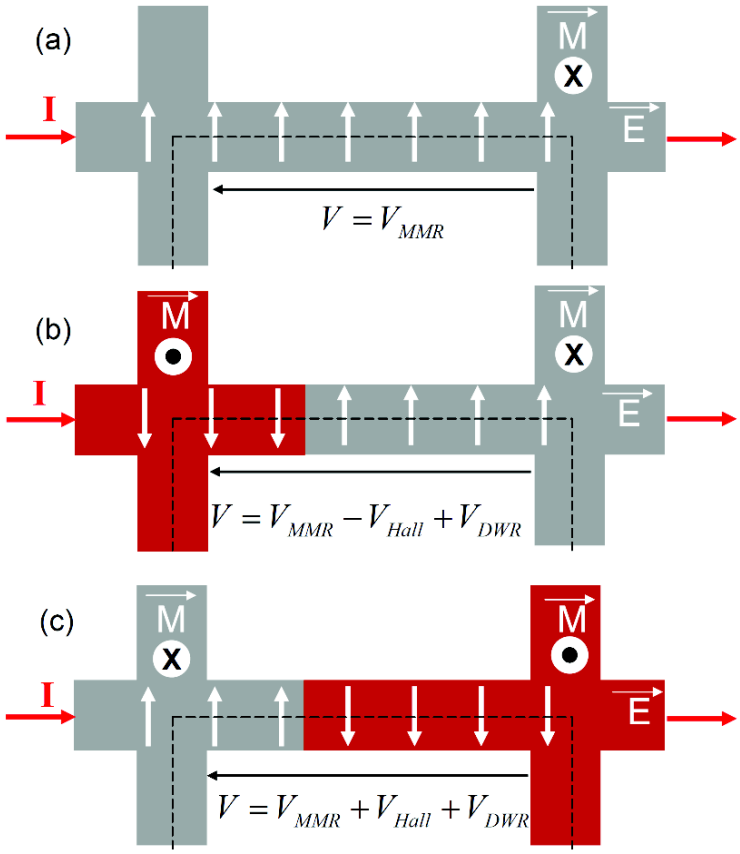

Figure 3.14: Schematics presenting the magnetic state of a perpendicularly magnetized nanowire and the associated distribution of the transverse electrical field when applying the current along the nanowire. White arrows present the transverse electrical field. To calculate the voltage different between the contact, one has to calculate the circulation of $\overrightarrow{E}$ ($\int \overrightarrow{E}\,\overrightarrow{dl}$) along the dotted line. (a) saturated state. (b) the presence of a DW in the positive field give a negative Hall contribution and (c) a positive Hall contribution when sweeping in negative field. In (a) the half Hall resistance in each cross cancel each other.

In figs. 3.15 are plotted major and two minor MMR loops (red and black curve) and the EHE loop of a full Hall cross (blue curve). In our model (*cf.*, figs. 3.14), the comparison of the resistance value of a full Hall cross and the additional resistance arising from MMR measurement have the same magnitude. However, as shown in the fig. 3.15, the offset resistances at zero fields during the minor loop of the MMR measurement in both sign of the applied field are not symmetric to zero ($+2.2\Omega$ for reversing in the negative side and -1.9Ω for the positive side) as expected for the solely contribution of the Hall effect.

The additional resistance is due to the contribution from intrinsic DW resistance, which is mainly attributed to spin mistracking [117, 118]. Indeed, FePt epitaxial films with strong perpendicular magnetic anisotropy, results in Bloch type DW. Therefore, the magnetization inside the DW is always perpendicular to the current, which exclude the AMR contribution arising from the rotation of magnetization within the DW. In the present case, the DW resistance is

roughly estimated by comparing the middle point of the 2 minor loops at zero fields with the full loop. The middle point is presented by a black cycle dot in the fig. 3.15.

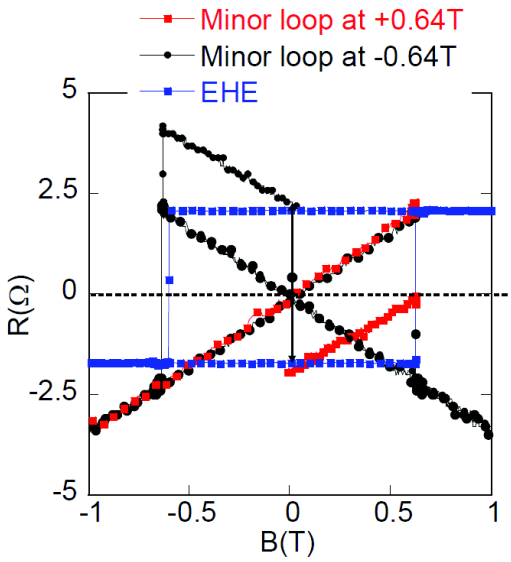

Figure 3.15: Comparison of the Hall resistance measured for a single Hall cross. The offset resistance during the minor loops in MMR measurement shows a DW resistance contribution. The middle point of the 2 minor loops at H=0 is presented by a black dot and is shifted compared to the saturated case.

The DW resistance of a single DW is found to be around 0.15 Ω, corresponding to the resistance area product of $7.5.10^{-17}\ \Omega.m^2$ for 50 nm wide and 10 nm thick FePt nanowire. This value is of the same order of magnitude with the previously reported value of $2.6.10^{-16}\ \Omega.m^2$ for 900 nm wide and 18 nm thick FePt wire [119].

In summary, we have shown the existence of Hall and DW resistance in longitudinal MR measurement when a DW is located between the voltage probes. However, this does not modify the slope of the MMR measurement, it only contributes to an additional resistance on the MMR measurement. In fact, this behavior generally happens in the perpendicularly magnetized systems based nanostructures. Indeed, we also found the same behavior in the CIP FePt based spin valve structures. In partially reversed state, *i.e.,* a DW is located between two voltage probes of GMR measurement, it also exits an offset of resistance due to the Hall resistance. This result underlines that one has to take into account the offset due to the Hall resistance when measuring the DW position using GMR measurement in system with perpendicular anisotropy.

Conclusions

We have demonstrated that MMR measurement can provide a way to probe magnetization reversal in FePt nanowires. In particular, we showed that it can be used to detect DW position and to follow the dynamic of DW propagation in a nanowire made of a single layer. Note that these quantitative measurements of DW position and motion in ferromagnetic nanostripes have been only achieved using multilayers with GMR or TMR but they require an additional magnetic reference layer. In comparison to MMR, AMR only indicate whether or not the DW is present in between the contacts. Similarly, EHE only points out the presence of a DW within a Hall cross. Therefore, the MMR provide a promising tool to study magnetization reversal in nanostructures.

Finally, we showed the existence of an asymmetric behavior in longitudinal MR measurement of FePt nanowires when a DW is located between the voltage probes. This is due to an additional Hall resistance arising from the perpendicularly magnetized contacts. By comparing with a single Hall cross measurement, this allows deducing the intrinsic DW resistance in FePt nanowires.

Chapter 4

Magnon magnetoresistance in NiFe nanowires and nanomagnets

In the previous chapter, we showed that MMR allows measuring quantitatively the magnetization reversal in nanowires with perpendicular magnetization. In the following works, we prove that such MMR measurement can be extended to systems with in plane magnetization such as NiFe nanowires [105]. We indeed show that the replacement of the magneto-crystalline anisotropy by a shape anisotropy leads to very similar MMR properties. NiFe nanowires constitute model systems in which the magnetization reversal is governed by the shape anisotropy, and provide the basis of most experiments on field-induced DW dynamics [54] and current-induced DW motion [26]. They are also used in numerous experiments and are the most commonly used spin injector in non-magnetic nanowires [120, 121]. Up to now, the MR of NiFe nanowires has always been interpreted in term of AMR [71, 122]. In this chapter, we will show that the enhancement of the shape anisotropy in narrow wires leads to the disappearance of the AMR signal, the remaining contribution to the MR being that of the magnons. Particularly, by using a constriction to pin the DW, we prove that the MMR signal can give access to the position of a DW along the wire [72]. Finally, we will present the study of the magnetization switching of a single NiFe nanomagnet using MMR measurement. Also, the measurement of the angular dependence on the magnetization switching allows studying the magnetization reversal mode in a single NiFe nanomagnet. Finally, we suggest and studied ways to enhance MMR signal.

4.1 Observation of the Magnon magnetoresistance in NiFe nanowires

NiFe nanowires with widths ranging from 500 to 50 nm have been patterned by means of e-beam lithography on Si substrate. For that purpose, a 30 nm thick NiFe layer was e-beam evaporated from an alloy target of nominal composition $Ni_{80}Fe_{20}$. The composition of the layer, measured by energy-dispersive X-ray spectroscopy, is $Ni_{84}Fe_{16}$. The NiFe nanowires were then obtained using a lift-off process. The detail of the nanofabrication process can be found in the appendix A. Fig. 4.1 displays the representative SEM image of a 200 nm wide NiFe nanowire with a set of Au contacts for electrical characterizations. MR measurements were carried out at room temperature in a four-probe configuration, using standard lock-in techniques. An *ac* current ($J = 3.10^{10} A/m^2$, $f = 6700\ Hz$) was then injected along the wire, and the voltage drop is measured at different positions on the 20 μm long nanowire.

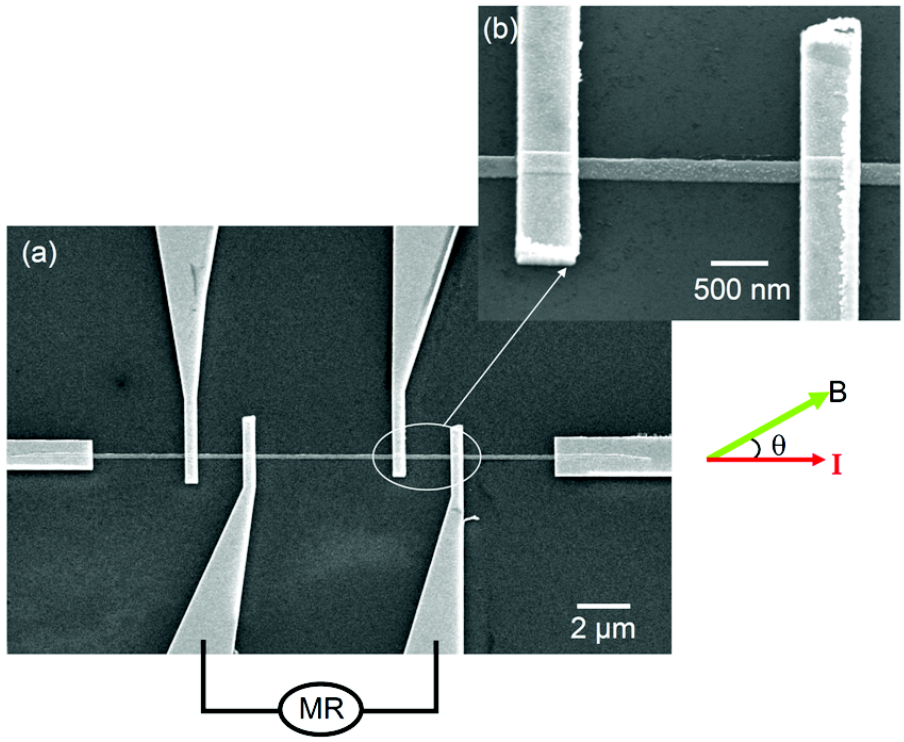

Figure 4.1: (a) SEM micrograph of a 200 nm wide NiFe nanowire, with a set of Au contacts to perform four-probe resistance measurements. (b) Low scale SEM image of the 200 nm wide NiFe nanowire.

Fig. 4.2 shows the MR curves of a 50 nm wide NiFe nanowire, for different orientations of the applied field (the rotation axis belongs to the sample plane, and is perpendicular to the wire). If the applied field is perpendicular to the wire ($\theta = 90°$) (*cf.*, fig. 4.2a), one observes the classical AMR curve, the bell shape curve indicates the rotation of magnetization with

the applied field [122, 71]. The total amplitude of resistance change is 2%, as expected for NiFe. However, at zero degree, the resistivity decreases linearly with the applied field, whereas according to AMR theory it should be constant. We attribute this non negligible decrease of the resistance with the applied field to the electron-magnon diffusion. An alternative explanation based on AMR can be disregarded as it would require a misalignment of ∼20° to give account of the observed slope (∼ 0.2 % in 1 T).

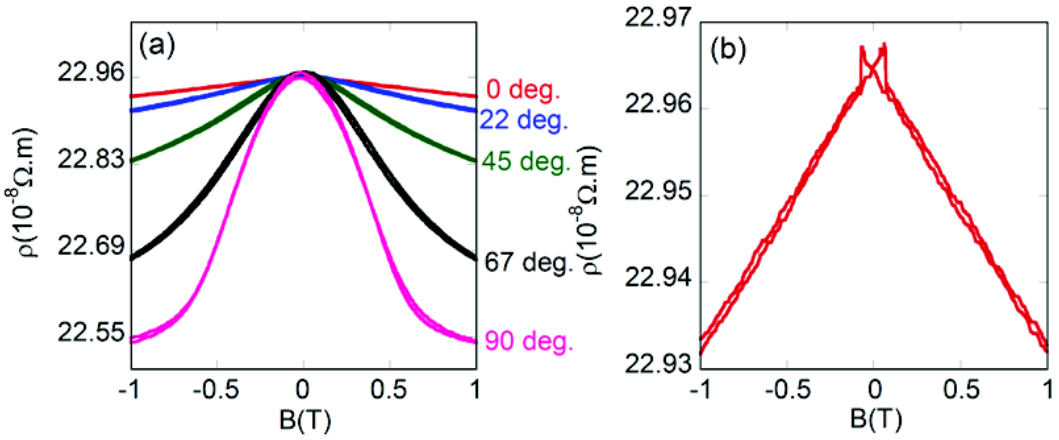

Figure 4.2: (a) MR curves of a 50 nm wide NiFe nanowire for different angles between the wire axis and the applied field. (b) MR curves for an applied field parallel to the wire.

Obviously, the MR curves at 0° (*cf.*, fig. 4.2b) have an aspect very similar to the MMR loop observed in FePt, with a sharp decrease of resistivity associate to the magnetization reversal. We state that the MR behaviour at 0° is dominated by the MMR.

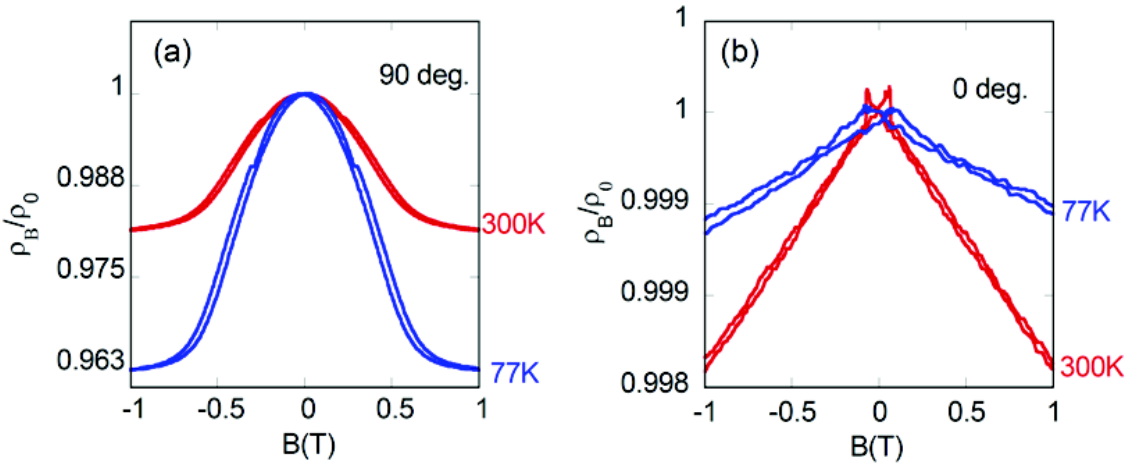

Figure 4.3: Normalized MR curves of a NiFe nanowire, for fields applied at (a) 90° and (b) 0° at 77K and 300K.

To corroborate this analysis, we studied temperature dependence on the MR behavior. Fig. 4.3 shows MR curves of 50nm wide NiFe nanowires at different temperature for 0 and

90°. Whereas AMR signal increases when temperature is lowered (*cf.*, fig. 4.3a), the MMR is reduced when the magnon population decreases (*cf.*, fig. 4.3b). This decrease of MMR signal at low temperature is similar to what has been previously observed in FePt [107].

Also, our interpretation is supported by the size dependence of the phenomenon. Fig. 4.4 shows the MR curves, for fields applied along the NiFe nanowires, and for widths ranging from 500 to 50 nm. It clearly shows that the MR behaviour changes when varying the widths. Note that for all widths, in the saturated state the resistance of the nanowires evolves linearly with the applied field. This effect observed at high fields is related to the MMR [106, 107].

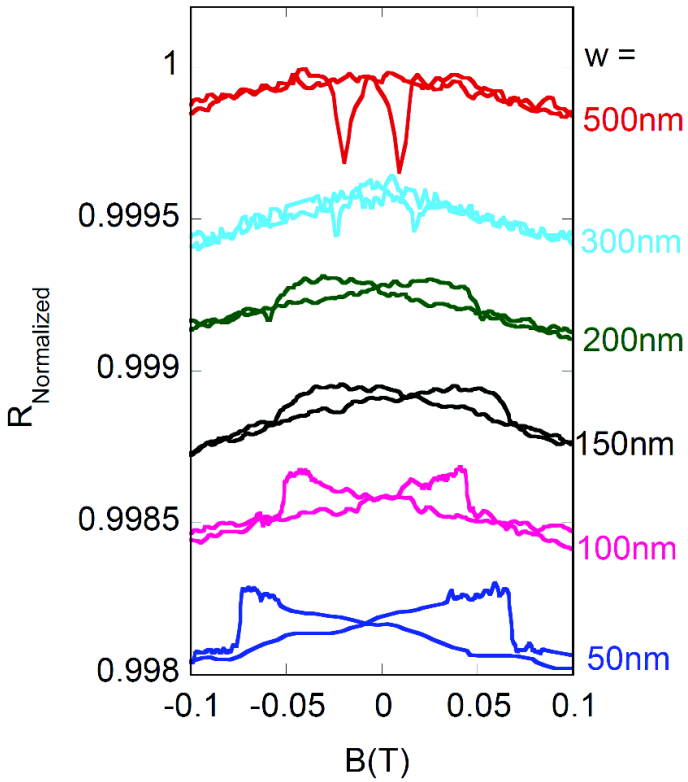

Figure 4.4: MR curves recorded on NiFe nanowires of various widths, as indicated on the curves, for a field applied along the nanowires. The usual decrease of resistance associated with the magnetization reversal measured by AMR becomes an increase of resistance for the smallest wires.

Indeed, in 500 nm wide wires, one can observe the classical AMR effect, where a decrease of resistance is at first observed after the field reversal, followed by a positive jump of resistance revealing the magnetization switching. This behaviour corresponds to the rotation of magnetization toward the reversed direction of applied field, generating a decrease of resistance. Surprisingly, when reducing the width of the nanowire, this decrease of resistance is changed into an increase of resistance, which appears as soon as the field direction is reversed. For widths smaller than 150 nm, the MR curves exhibit, after the field reversal (*i.e.*, when magnetization and applied field are anti-parallel), the same linear variation observed at high

field. This evidences that the AMR contribution has disappeared and that the MR is thus dominated by the MMR. As seen in FePt sample [107, 105], the MMR curves show a drop of resistance at the switching field, due to the abrupt change of magnon density. The disappearance of the AMR contribution in narrow NiFe wires is due to the enhancement of the shape anisotropy. As the width gets smaller, the increased importance of the demagnetizing energy keeps the magnetization along the wire axis. Consequently, the magnetization stays parallel to the wire. Apart during the reversal, the magnetization direction is always parallel to the current lines, thus the AMR contribution to the MR loop vanishes. The theoretical analysis of the MMR curve is the same as those provided for FePt [107] and described in detail in the previous chapter, except that the uniaxial magnetocrystalline anisotropy of FePt has simply to be replaced by the shape anisotropy of the NiFe nanowire.

4.2 Detection of magnetization reversal and domain wall position in NiFe nanowires

4.2.1 Detection of magnetization reversal in NiFe nanowires

The following work show that MMR measurement can be used to study quantitatively magnetization reversal in NiFe nanowires. The low field MMR curves on various lengths of a 50 nm wide NiFe nanowire in fig. 4.5a show a sharp decrease of resistivity about ∼0.02 % corresponding to the magnetization reversal of the nanowire. These MMR signals are quite small but as seen in fig. 4.5, they are nicely measurable using lock-in technique.

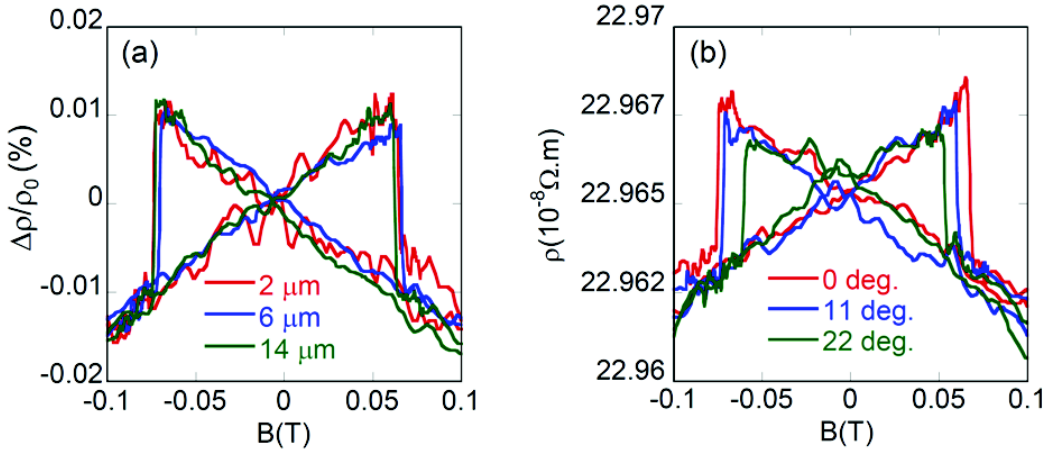

Figure 4.5: (a) MR curves of various lengths of a 50 nm wide NiFe nanowire for applied fields parallel to the wire. (b) MR curves of a 50 nm wide NiFe nanowire for different angles between the wire axis and the applied field.

Moreover, these loops also reveal that MMR curves do not vary with the distance between

contacts, even when using a two probes measurement (curve for the 14 μm long wire) which exclude any magnetoresistive contribution related to the contacts. Such a simple resistance measurement using a two probes configuration can be useful to detect the switching fields of ferromagnetic nanowires, in nanostructures possessing various geometries (*e.g.,* injection electrodes as in lateral spin valves [120, 121]).

Interestingly, the angular dependence of MMR curves in fig. 4.5b show that such measurement can be performed to detect magnetization reversal for various field orientations. As the shape anisotropy is strong in comparison with the switching fields, there is no significant AMR contribution at angles smaller than 20°, and the MMR measurements allow detecting precisely the switching fields. These curves also underline, here again, the fact that the observed loop is not due to an AMR contribution, which might come from a misalignment of the applied field and of the wire.

Remarkably, the MMR curves of NiFe nanowires in fig. 4.5 show that, by applying fields smaller than the switching fields, it is possible to detect the magnetization orientation without reversing it: the sign of the ρ(B) slope is negative if the magnetization is parallel to the field, and positive if it is anti-parallel.

4.2.2 Measurement of domain wall position along a NiFe nanowire

In materials with in-plane magnetization as NiFe nanowires, the AMR may be used to detect the presence of DWs along a nanowire [14, 123]. However, AMR measurements only indicate whether or not the DW is present in between the contacts. The presence of DW is associated to a decrease of resistance since the local magnetization has some transverse components. Here, we demonstrates that MMR measurements can measure precisely the position of a DW along the NiFe nanowires [72].

In order to pin a DW between two electrical contacts, we used a constriction as previously reported (*e.g.*, [123, 14]). Fig. 4.6a shows the SEM observation of a 100 nm wide NiFe nanowire with a 40 nm constriction. A large NiFe nucleation pad at the end of the wire allows injecting a single DW into the nanowire.

Fig. 4.6b shows the MR curves of different segments of the NiFe nanowire for an applied field parallel to the wire. One can observe that MR measurement between contacts 1 and 2, without constriction, shows clearly a MMR effect which is similar to the case of a straight NiFe wire. Note that in this case the switching field is considerably smaller ($B_C \sim$ 0.02 T) than the case of straight wire ($B_C \sim$ 0.05 T) as presented above. It is due to the fact that DW has already been nucleated in the nucleation pad at the end of the wire: the switching field is determined by propagation rather than nucleation field. The MR curve recorded between contacts 3 and 4 where a constriction is located shows a slightly different behavior (*cf.,* fig. 4.6b). Above magnetization saturation, one can observe a linear dependence of the resistance

on the applied field which is due to MMR.

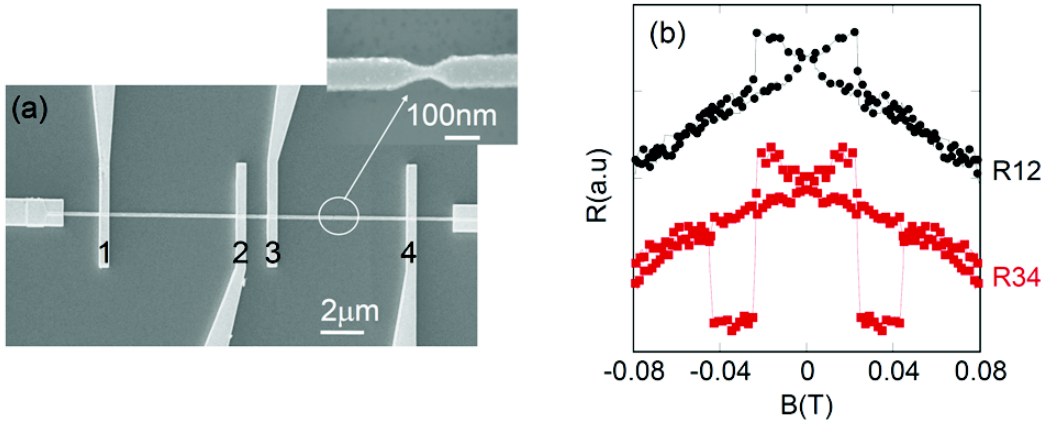

Figure 4.6: (a) SEM images of a 100 nm wide permalloy nanowire with a 40 nm wide constriction. (b) MR measurements of different segments with the field swept along the wire axis, *i.e.*, without constriction between contact 1 and 2 (R12), and with constriction between contacts 3 and 4 (R34) of the 100 nm NiFe nanowire.

The MR curve shows a sharp downwards drop of resistance at the switching field (∼0.02 T), followed by a sharp resistance jump upwards at a field of 0.044 T. By further increasing the applied field, a linear dependence of the resistance is again observed. The different MR behavior in this case arises from a pinned DW between contact 3 and 4. In this case, an additional contribution to the resistance must be considered. It is due to the AMR arising from the rotation of magnetization within the DW and to the intrinsic DW resistance [42, 124].

Let's just assume that the AMR contribution of the pinned DW and intrinsic DW does not vary during the partial reversal (in fact, the pinned DW only contribute to an offset of resistance, not to the slope of MMR measurement). As shown previously in chapter 3 the contribution of MMR to the resistivity can be written as:

$$\rho = \alpha \frac{M}{M_S} B \tag{4.1}$$

where M is the total magnetization of the wire along the effective field axis, M_S is the magnetization at saturation, B is the applied magnetic field, and $\alpha = \left(\frac{\partial \rho}{\partial B}\right)_{sat.}$ is the slope of $\rho(B)$ taken in the saturated magnetic state ($\alpha < 0$)

As in the analysis of the previous chapter, eq. 4.1 implies that the slope of $\rho(B)$ in a given partially reversed state allows extracting $\frac{M}{M_S}$ and thus the DW position.

To demonstrate that MMR measurements provide the position of a DW along the NiFe nanowires, we followed the method used in the last chapter for FePt nanowires, based on the analysis of the slope during a minor loop. Fig. 4.7 show the recorded MR minor loop, in which a DW is injected into the nanowire and then gets pinned on the constriction. The applied field

is then swept back to positive values and the $\rho(B)$ slope is measured until the magnetization reverse on the other side.

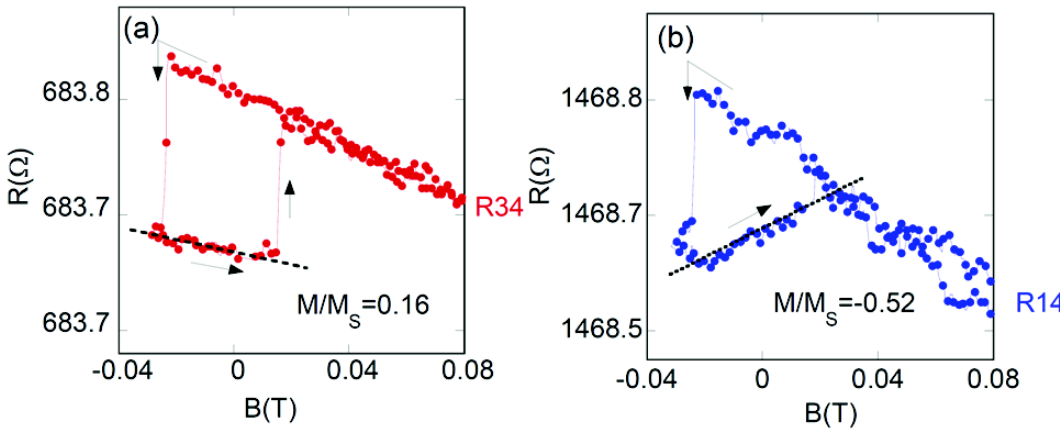

Figure 4.7: Extraction of magnetization from the slope of minor loops. (a) Minor MR loops measured between contacts 3 and 4. The slope of the minor MR loop allows measuring the value $\frac{M}{M_S}\sim$ 0.16, *i.e.*, to the reversal of around 42±5% of the length of this part of the wire. (b) Similarly, the minor loop of MR measured between contacts 1 and 4 showing the reversal of 76±5% the length of the wire.

According to eq. 4.1, the slope of the MR minor loop measured between contacts 3 and 4 (*cf.*, fig. 4.7a) leads to $\frac{M}{M_S}\sim$0.16 (with this field sweep direction, the ratio $\frac{M}{M_S}$ switches from +1 to -1), *i.e.*, the DW has reversed 42±5% of the length of the wire. This corresponds to the position of the constriction as observed in the SEM image, corresponding to ~44±2% of the length of the wire.

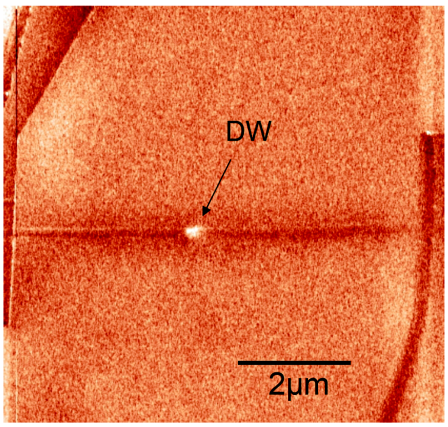

Figure 4.8: MFM image realized after the minor loop, showing that a single DW is located on the constriction. It is in agreement with the MMR measurement.

Furthermore, the slope of the minor loop measured between contacts 1 and 4 (*cf.*, fig. 4.7b) provides the value $\frac{M}{M_S}\sim -0.52$, *i.e.*, the DW has reversed $76\pm2\%$ of the length of the

wire. It also corresponds exactly to the position of the constriction as observed with SEM (at $74\pm$ 2% of the wire segment).

In both cases, the pinned DW position given by MMR measurement is in excellent agreement with the position of the constriction. Finally, we examined the DW position using MFM. Fig. 4.8 shows that a single DW is indeed located on the constriction. We emphasize again that such a detection of the DW position is not accessible using AMR measurements. Although the MMR amplitude is relatively small, MMR measurements thus provide in simple systems similar information to those obtained in multilayers using GMR or TMR.

4.3 Detection of magnetization reversal of a single nanomagnet

Due to tiny magnetic moment of nanostructure, the conventional magnetometers as VSM or SQUID are limited to study magnetization reversal of individual nanostructure. This emphasizes the need of measurement techniques to detect the magnetization reversal of a single nanostructure. MFM measurement with high spatial resolution have been used to detect magnetization reversal of a single nanomagnet, but this measurement is limited for time or field dependent measurement [125]. Also, the micro-superconducting quantum interference device (μ-SQUID), which has been developed to study the magnetization reversal of a single nanostructure, possess an excellent spatial and temporal resolution, however, this technique is limited to very low temperatures [126]. This part will shows that such a detection can be realized at room temperature using MMR measurement for a single 32 $\times$ 30 $\times$ 200 nm NiFe nanomagnet.

200 nm long ellipsoidal NiFe nanomagnets have been prepared using e-beam lithography and evaporation from a NiFe target on a patterned resist, the deposition being followed by a lift-off process.

This is basically the same nanofabrication process of NiFe nanowires as presented above. The NiFe layer is 30 nm thick, and the width of the nanomagnets ranges from 109 to 32 nm. Fig. 4.9a shows a representative SEM image of the nanodevice with a set of Au contacts. On each device, there are 3 separated nanomagnets that possess identical geometries and can be measured independently. Low scale SEM images of NiFe nanomagnets with different sizes (as indicated on each image) are showed in fig. 4.9b. The alignment of the Au contact on each nanomagnet has been done precisely, as the overlap with the nanomagnet is around 50 nm. MR measurements were carried out at room temperature using a two-probe measurement configuration (*cf.,* fig. 4.9a). An *ac* current ($I = 50\ \mu A,\ f = 6700\ Hz$) is injected, while the voltage drop is measured using a lock-in. Note that the Au contacts are made deliberately larges, to reduce the contribution of the Au pads to the measured voltage drop.

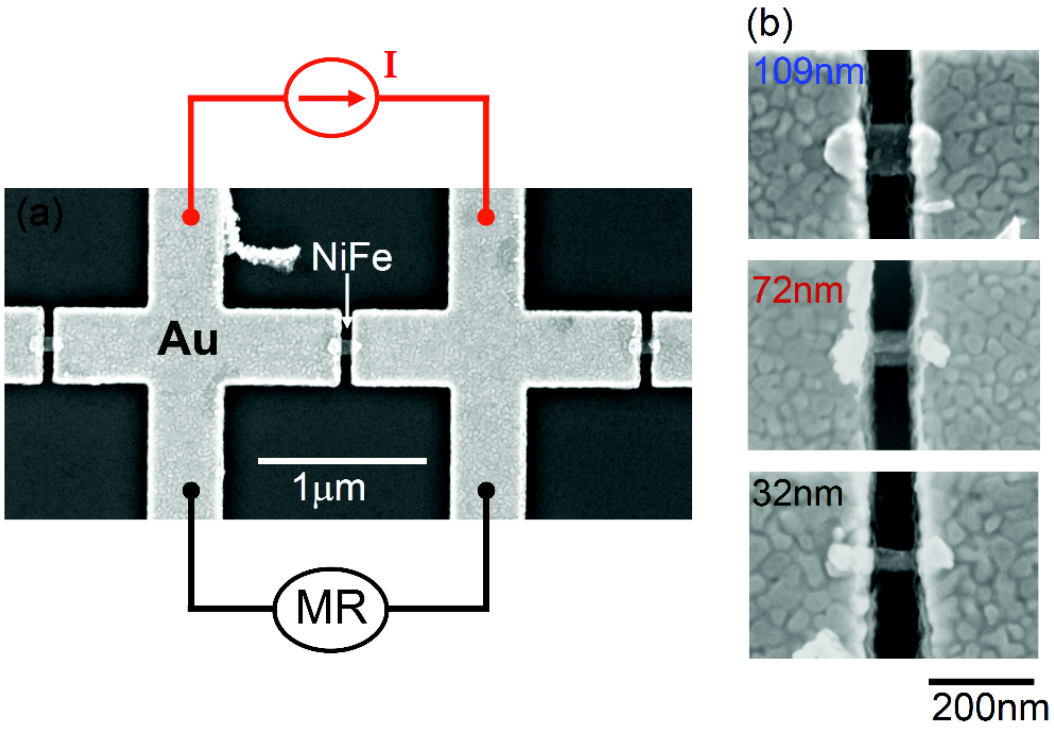

Figure 4.9: (a) Representative SEM images of 109 nm wide NiFe nanomagnets, with a set of Au electrical contacts to perform magnetotransport measurements. (b) SEM image of different size of NiFe nanomagnets. Their widths are indicated in each image.

Fig. 4.10a presents the MR measurements for nanomagnets of different sizes, for an applied field direction along the anisotropy axis of the nanomagnet. The MR behaviour varies when reducing the width from 109 to 32 nm. The MR behaviour of 109 nm wide nanomagnet is dominated by the AMR. The resistance first decreases and is followed by a sudden increase of resistance corresponding to the magnetization switching. When the width is reduced, the AMR contribution disappears, as shown in the MR curves of 72 and 32 nm wide. Here again is observed the transition of MR phenomenon from AMR to MMR. Note that above the magnetization saturation, the only remaining MR is the MMR, with a linear dependence of the resistivity with the applied field for all nanomagnets. The value of this slope (0.15 % at 1 T) is similar to that of a nanowire or layers despite of the two-probe measurement. It emphasizes that the contribution of magnons to the resistivity does not change from thin layer to very small nanomagnets. The disappearance of AMR in NiFe nanomagnets can be here again attributed to the enhancement of the shape anisotropy, as in the case of NiFe nanowires. A high aspect ratio in small nanomagnets leads to an increase of demagnetizing energy which tends to confine the magnetization along the easy axis. In our measurement configuration, the current lines are consequently always parallel to the magnetization direction, which is why the AMR contribution vanishes completely.

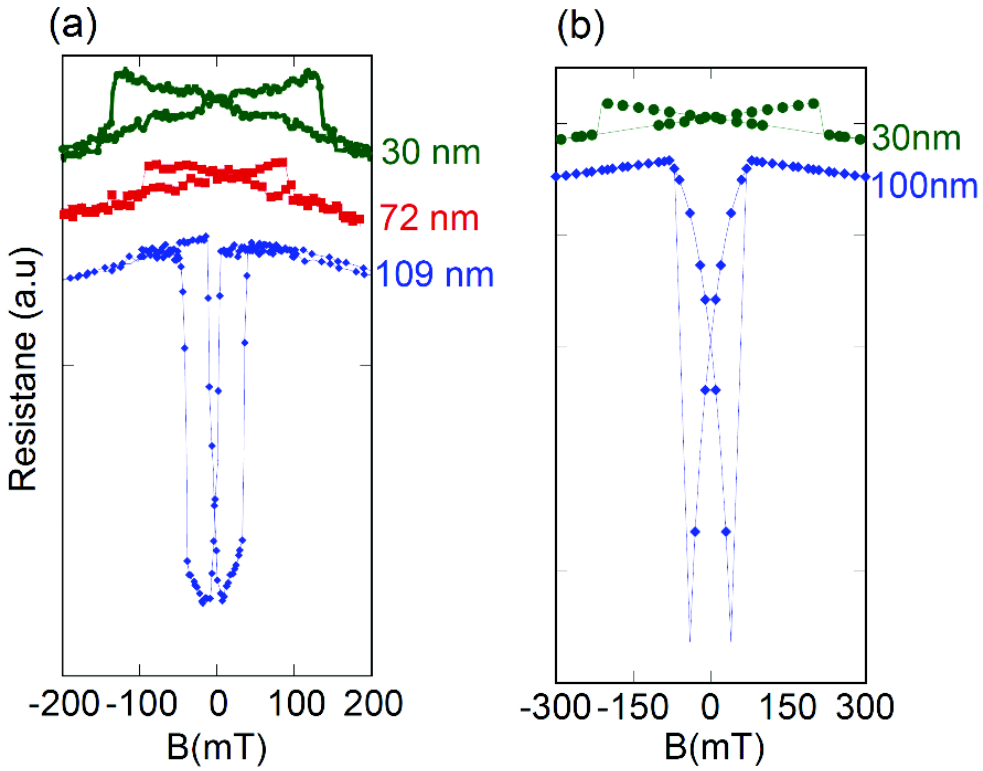

Figure 4.10: (a) MR curves recorded on NiFe nanomagnets of different widths (indicated on the curves), for a field applied along the easy axis of the nanomagnet. At small widths, the usual decrease of resistance associated to the AMR contribution disappears, replaced by an increase of resistance due to the MMR. (b) MR curves of NiFe nanomagnets calculated on the basis of OOMMF simulations.

The experimental curves are in good agreement with the behavior predicted by micromagnetic simulations [127], using the magnetic parameters of NiFe (M_S=800.10^3 A/m, A=13.10^{12} J/m, and negligible magneto-crystalline anisotropy). The simulated nanomagnets possess ellipsoidal geometries (30 nm thick, 200 nm long, and 30 to 100 nm wide). The cell size is chosen to be 5 $\times$ 5 $\times$ 5 nm^3, which is close to the exchange length of NiFe. The hysteresis behavior is then computed using discrete field steps. Finally, the MR behavior is extracted from the simulation data by taking into account both the AMR and the MMR contributions. It is assumed that each cell of the nanomagnet possess its own contribution to the MR, which depends on its magnetization direction. The current density is supposed to be homogeneous in the whole nanomagnet, and oriented along the easy axis. The AMR effect due to spin-orbit scattering can be written [11]:

$$\rho_{AMR} = \rho_{\perp} + (\rho_{\parallel} - \rho_{\perp})cos^2\theta \tag{4.2}$$

Where $\rho_{\perp}$and $\rho_{\parallel}$ are the resistivities obtained when the magnetization is perpendicular or parallel to the current direction. θ is the angle between the magnetization and the current

direction. The values of $\rho_\perp$and $\rho_\parallel$ are experimentally determined using MR measurement in parallel and perpendicular direction respect to the easy axis (the typical value $\frac{\rho_\parallel - \rho_\perp}{\rho_\perp}$ in our sample is ∼1.5 %)

As shown above, MMR works in every direction and can be expressed as:

$$\rho_{MMR} = \alpha \frac{M}{M_S} B \tag{4.3}$$

The typical value of the slope of $\rho(B)$ is 0.15 % in 1T at room temperature which is experimentally extracted from MR measurements at high fields.

Based on this expression the total resistivity of a cell can be written:

$$\rho_{total} = \rho_\perp + (\rho_\parallel - \rho_\perp) cos^2\theta + \alpha \frac{M}{M_S} B \tag{4.4}$$

Fig. 4.10b presents the calculated MR curves of 100 and 30 nm wide NiFe nanomagnets. The simulations reproduce the transition from AMR at large size to MMR at small sizes. It emphasizes that the high shape anisotropy in small nanomagnets leads to the disappearance of the AMR contribution, and that MR measurements in NiFe nanomagnets should take into account both the contribution of AMR and MMR. The simulations also reproduce, at low widths, the drop of MMR corresponding to the decrease of the magnon population at the switching field. Experimentally, MMR measurements allow detecting precisely the switching field of the NiFe nanomagnets at room temperature. This measurement is not restricted to the specific case where the applied field and the anisotropy axis are parallel: it is indeed possible to study the complete angular dependence of the switching field.

Fig. 4.11b shows the MR curves of a 32 nm wide nanomagnet for various angles (the rotation axis is perpendicular to the sample plane as schematically illustrated in fig.4.11a). It shows that the MR behaviour strongly depends on the direction of applied field and the shape anisotropy. One can see in fig. 4.11, at zero degree, and more generally for angles smaller than 20°, the magnetization is nearly parallel to the current lines, until the applied field reaches the switching field. In this configuration, the AMR variations are thus weak, but it is possible to measure the switching field using MMR. For larger angles, the AMR contribution increases and finally dominates over the MMR contribution. For example, the MR curve at 45º (*cf.,* fig. 4.11b) exhibits at low fields a positive jump of resistance due to AMR and revealing the magnetization switching. When the applied field is perpendicular to the easy axis of the nanomagnet, one observes the classical parabolic behaviour due to AMR [122], which is induced by the coherent rotation of the magnetization. Whatever the direction of the applied field, the switching field of the 32 nm NiFe nanomagnets can be detected, using MMR at small angle and AMR otherwise. Note that for 0 and 90° orientations, there is above the magnetization saturation a linear dependence of the resistance with the applied field due

to the MMR.

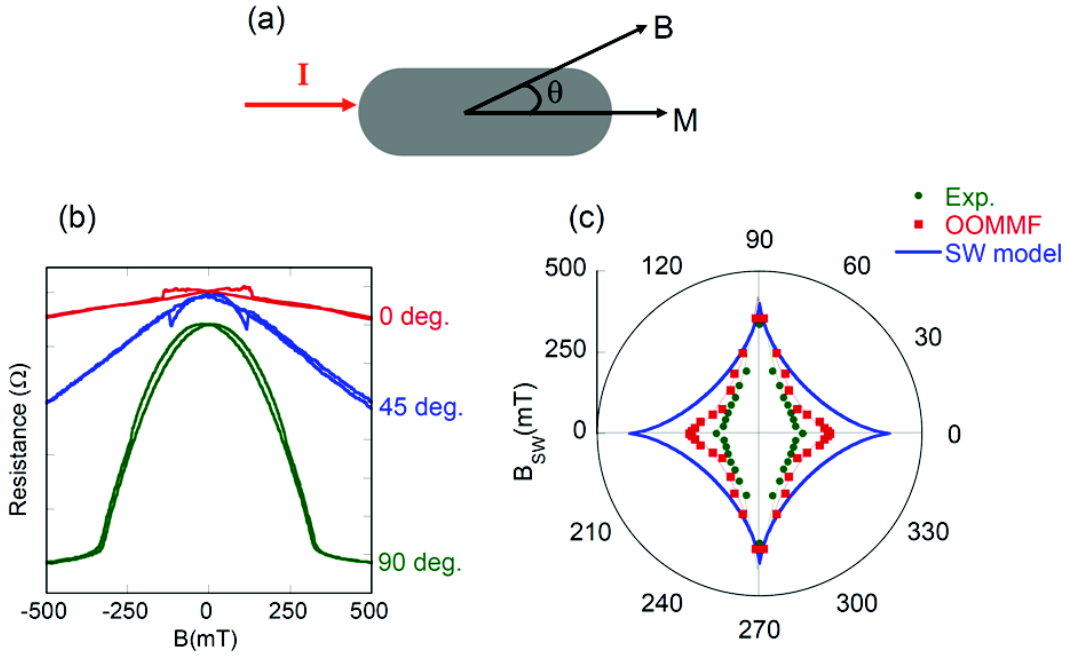

Figure 4.11: (a) Schematic showing the direction of the applied field respect to the easy axis. (b) MR curves of a 32 nm wide NiFe nanomagnet for different angles between the applied field direction and the easy axis of magnetization. (c) Switching field of the 32 nm wide NiFe nanomagnet as a function of the angle between the applied field direction and the easy axis of magnetization, extracted from the MR measurements (green cycles), from OOMMF calculations (red squares). The continuous blue curve corresponds to the Stone-Wohlfarth model.

The angular dependence of the switching field extracted from MR measurement is presented in Fig. 4.11c (green cycles). For a comparison, we added the prediction of the Stoner-Wohlfarth model by drawing the corresponding astroid curve. The differences between the two curves arise from the fact that here the reversal is probably non-uniform [128, 129], as the characteristic size of the nanomagnet is significantly larger than the exchange length ($l_0 = \sqrt{\frac{A}{\mu_0 M_S^2}} \approx 5nm$). In our measurement, the size of NiFe nanomagnet is about∼200 nm long, thus its magnetization mode seems to be dominated by non-uniform reversal. The angular dependence of the switching field has been computed using OOMMF simulations. The switching is found to be non uniform, and the obtained angular dependence is close to the experimental one. Note that OOMMF simulations corresponds to T=0 K calculation. The switching of a single NiFe nano element can be thus measured using magneto-transport measurements at room temperature. For applied fields nearly parallel to the anisotropy axis, the reversal has to be detected using the MMR. These results suggest that MMR measurements can be a tool to study the dynamics of magnetization reversal of a single nanomagnet.

4.4 Enhancement of MMR signal

As presented above, MMR measurement might become a versatile tool for realizing transport experiments in magnetic nanostructures, and has to be taken into consideration when interpreting MR curves of magnetic materials. Even though its magnitude is small for applications, it can be easily and precisely measured using standard lock-in techniques.

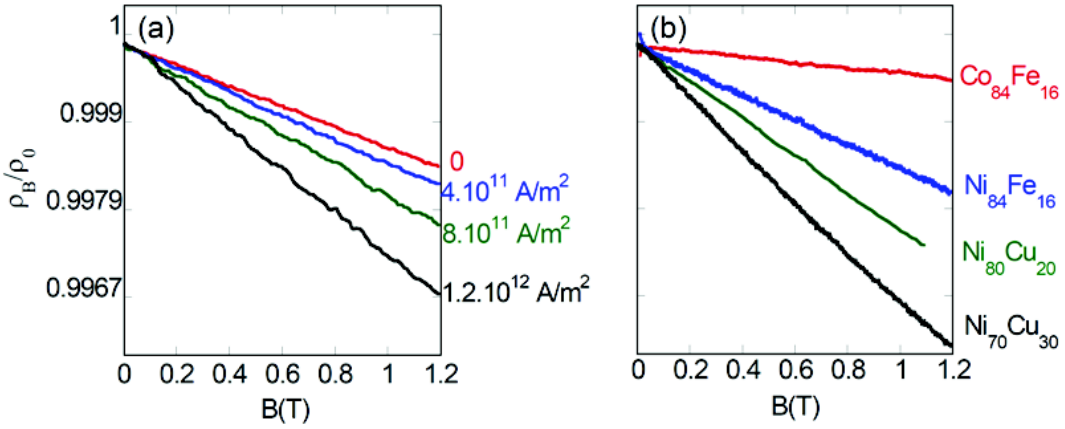

Figure 4.12: (a) MR curves of a NiFe nanowire, heated by different offset of current densities. The slope of the curves give the amplitude of the MMR effect, which increases with the temperature. (b) MR curves of different thin films at room temperature. One can see the amplitude of the MMR increasing for the sample whose Curie temperature is close to room temperature.

Also, magnitude of MMR can be enhanced: as seen in fig. 4.12a, that might be simply done by heating. These experiments were carried out by adding an *dc* offset current to MR measurements. For example, at current density $J_{dc} = 1.2.10^{12}\ A/m^2$, the slope of MMR is increased by a factor of 2 compared to $J_{dc} = 0$. Moreover, the magnitude of the MMR is strongly material dependent [106], and materials engineering may provide samples with high MMR signals.

Indeed, the normalized slope of MMR for different materials in fig. 4.12b show an enhancement of the MMR signal when measuring the sample with Curie temperature closer to the room temperature. The largest slope is obtained for the $Ni_{70}Cu_{30}$ sample whose Curie temperature is around 300 K. When the temperature approaches the Curie temperature, the MMR slope is significantly increased, as the magnon contribution to resistivity increases relatively to other sources of resistivity (phonons,. . .).

Conclusions

We have shown that MMR measurements are not restricted to systems with strong perpendicular anisotropy. In particular, for certain field directions the magnon contribution dominates the magnetoresistance, clearly overcoming the AMR. Consequently, MMR can be used to study magnetization reversal in nanowires with in-plane magnetization.

We found that the MR behavior varies strongly when reducing the wire widths. In small NiFe nanowires (w$<$150 nm), and for fields nearly parallel to the wire axis, the AMR contribution disappears and the remaining contribution to the MR then has to be understood in terms of MMR. This underlines that the explanation of MR measurements in NiFe nanowires should take into account both the AMR and MMR contributions.

We also proved that MMR can be used as a tool to detect precisely the DW position in NiFe nanowires. Therefore, it will provide a quantitative way to follow the magnetization reversal in ultra narrow wires with in-plane anisotropy, including DW position and motion. In the chapter 5, we will present the results on dynamic of DW pinning in NiFe nanowires using this new technique.

Moreover, we showed that MMR measurements can be used to detect the magnetization switching of a single nanomagnet down to 200 nm in length and 32 nm in width (order 10^7 of atoms). The angular dependence of the switching field can be measured, thus allowing the study of reversal modes of such nanomagnets.

The MMR signal can be enhanced when getting closer to the Curie temperature. Finally, we suggest that it could also be used as a tool to probe the magnon population: when the magnon population increases, the resistivity should vary with the number of electron-magnon diffusion events.

Chapter 5

Stochasticity of domain wall depinning in ferromagnetic nanowires

Precise control of DW pinning and depinning in nanowires is crucial for the operation of new spintronics devices: race track memory or DW-RAM. However, the existence of the random behavior of DW depinning is a major challenge for practical applications. The stochastic behaviors of DW depinning have been experimentally studied in systems with perpendicular [49, 33, 130] and planar magnetization [123, 131, 132, 133]. This behavior has been also investigated using simulations [134] or analytical models [135]. It has been shown that two sources of randomness exist: thermal activation and different configurations of the pinned DW. In this chapter, we will first discuss on state of the art of field and current induced DW depinning in nanowires. In the following, we will show our experimental results in which we focus on the three different behaviors of DW depinning which have been similarly observed in both FePt and NiFe nanowires using different class of pinning site.

5.1 State of the art of field and current induced domain wall depinning

5.1.1 Stochasticity of domain wall depinning under applied field

The first origin of the stochastic behavior of DW depinning arises from thermal activation. The thermally activated regime can be observed at an applied field below the propagation field where the DW motion is characterized by discrete jumps between metastable states. Experimentally, time resolved measurements have been mostly used to study the thermally assisted DW depinning [49, 44, 33, 133, 130, 67]. Due to the broad distribution of switching fields, the measurement process is usually repeated several hundred times in order to get a good estimation of the distribution of pinning time. Finally, the probability to depin the DW

is measured at different applied fields or at different currents which allow studying the nature of pinning barriers.

Using EHE measurements to detect DW depinning from a single structural defect in FePt nanowires, Attané *et al.*, [49] have observed the stochastic behavior of DW depinning under applied field. The results showed that the DW pinning time is random and follows an exponential probability law (*cf.*, fig. 5.1). This demonstrated that the DW motion in the wire is dominated by a thermally activated process over a single energy barrier.

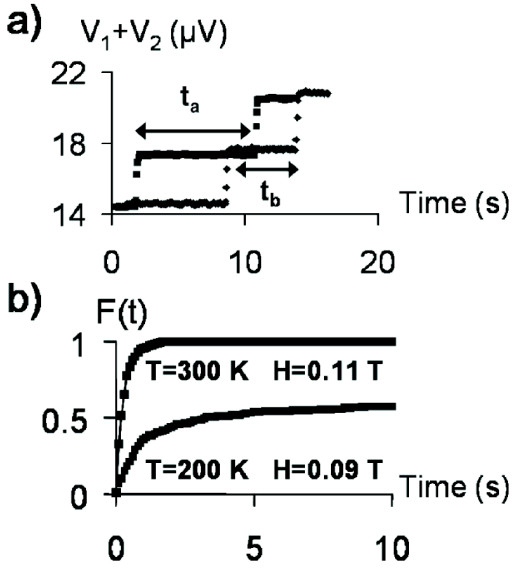

Figure 5.1: (a) Two independent measurements of the sum of Hall voltages V1+ V2 (the two Hall crosses are separated by $10\ \mu m$) as a function of time under the same constant field and leading to different propagation times t_a and t_b. (b) Cumulative distribution functions of the propagation time at T=300 K and 200 K, resulting from 400 independent measurements. At 300 K, the curve can be fitted by an exponential law (Figures are reproduced from ref.[49]).

For systems with in-plane magnetization as Py nanowires and using transmission electron imaging of DW motion between two positions in real time, Eltschka *et al.*, [133] showed that the motion of DWs is assisted by thermal activation and well described by an Arrhenius law.

The second source of stochasticity arise from the different configurations of the pinned DW. The reason is that several metastable structures of a pinned DW exist, each one corresponding to different pinning potential. Hayashi *et al.*, [42, 15] showed an interesting example where a DW is injected and pinned at a notch in 300 nm wide Py nanowires. Combining AMR, MFM measurements and micromagnetic simulations, they found four different DW states corresponding to two vortex walls and two transverse walls, each one having different chirality, either clockwise or anticlockwise (*cf.*, fig. 5.2).

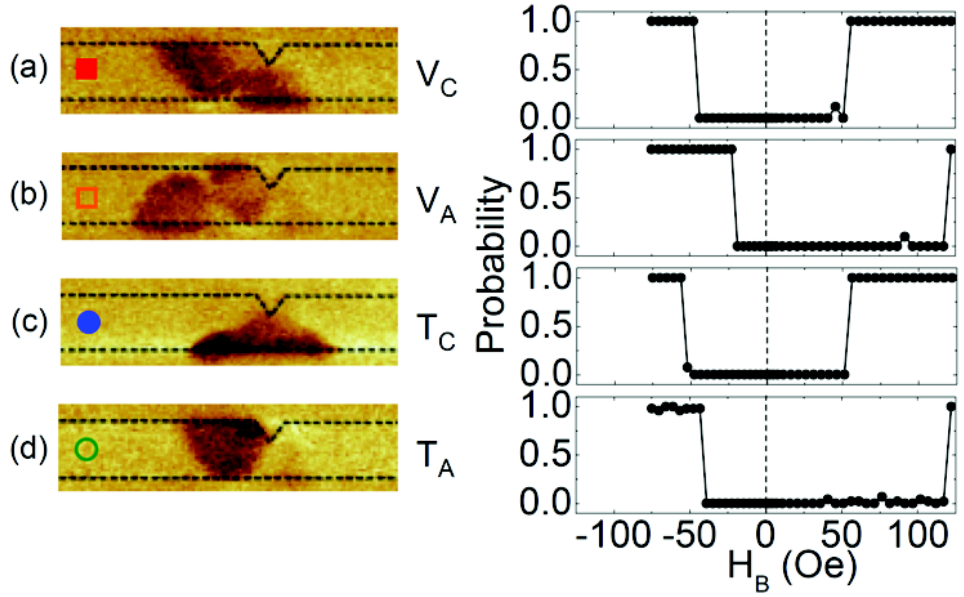

Figure 5.2: Left panels: MFM images showing the four different DW configurations pinned at the notch of a Py nanowire. (a-d) Vortex and transverse DWs with different chirality: clockwise (V_C, T_C) and anticlockwise (V_A, T_A). Right panels: Field driven depinning probability vs applied field showing different depinning fields for different DW types (Figures are reproduced from ref. [42]).

Interestingly, the results showed that the DWs can have four different internal spin structures each one corresponding to the different depinning fields (*cf.,* figs. 5.2). In another experiment, Im *et al.* [132] observed by magnetic soft X-ray transmission microscopy the stochasticity of the DW depinning field at the notch of Py wire. They showed that such stochastic behavior depends on the wire width and the notch depth which induces the generation of various DW types in the vicinity of the notch. Similarly, Akerman *et al.*, [123] showed that the microstructure of the pinned DW depends not only on the geometry or the quality of the patterned notch, but also on the structure of the moving DW approaching the notch.

In some cases, the stochasticity have been observed due to both thermal activation and configuration multiplicity of DW which induced a more complex mechanism of depinning [67, 131].

5.1.2 Domain wall depinning under applied current

Experimentally, current-induced DW dynamic can be usually studied based on two kinds of experiments, current-induced DW propagation and current-induced DW depinning. In the first one, the DW position in the nanowire is detected before and after the application of currents. Thus, the critical current and the velocity of DW motion can be estimate. In the second one, DW depinning is measured as a function of the applied current which allows studying the

nature of pinning barrier under the influence of currents. A few review papers on the topic of current induced DW dynamic can be found in the refs. [43, 26] and the references therein. Here, we will mention on recent experimental results of current induced DW depinning in nanowires.

A simple technique is to measure the depinning field as a function of the applied currents. In most experiments, a linear dependence of the depinning field on the applied currents is found [45, 18]. As an example, Boulle *et al.* [45] showed the variation of depinning field in (Pt/Co/Pt) Hall cross at constant sample temperature with different current polarities in which one current polarity assist the DW depinning whereas the other one hinders the depinning (*cf.*, Figs. 5.3).

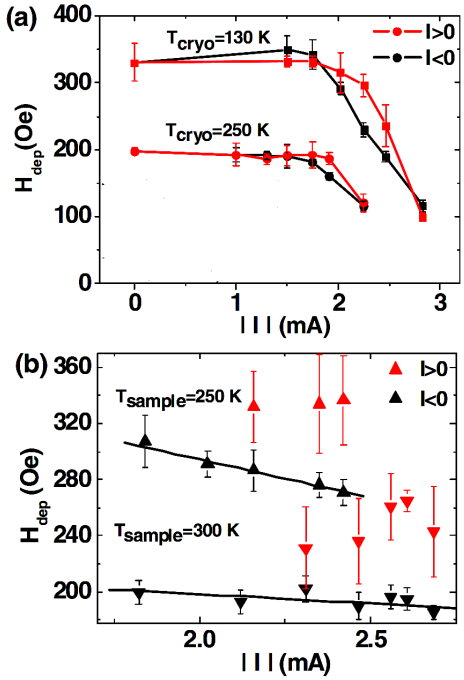

Figure 5.3: (a) Variation of the depinning field, measured by EHE as a function of the applied current for a constant cryostat temperature. (b) A linear dependence of depinning field on the applied current allows extracting the spin torque efficiency of this system (Figures are reproduced from [26])

From the evolution of the depinning field versus current, they can derive a spin torque efficiency, $\xi = 2.5 \pm 0.35 \times 10^{-14} T.m^2/A$ for Tsample = 250 K and $\xi = 6 \pm 1.5 \times 15^{-15} T.m^2/A$ for Tsample = 300 K. Furthermore, using simulation based on a 1D model including thermal activation and nonadiabatic torque as an effective field $\mu_0 H = \xi I$. This allows deducing the nonadiabatic term $\beta = 1.45 \pm 0.25$ for Tsample = 250 K and $\beta = 0.35 \pm 0.08$ for Tsample = 300 K. For the systems with a complex DW structure as in in-plane magnetized materials, to improve the description, experimental studies are usually combined with micromagnetic

simulations that includes applied fields and currents. One can then compare the measured depinning field as a function of current density with simulations using different values for β and spin polarization P [136].

The second approach is based on the time-resolved measurements. Assuming that a DW can be described as a quasiparticle in a 1D potential landscape, Kim *et al*. [137] showed theoretically that the mean depinning time due to thermal activation process that follows an Arrhenius law over a single energy barrier. As the result, the pinning time can be expressed as:

$$\frac{1}{\tau} = f_0 exp\left[\frac{-E(I)}{k_B T}\right] \tag{5.1}$$

where f_0 is the attempt frequency and $E(I)$ is the energy barrier under the application of current I .

As generally observed in the experiments, the model assume that the action of the current on the energy barrier is equivalent to an external effective magnetic field $H_{eff} = \xi I$. The energy barrier change due to current induced spin-torque is thus linear with the applied current:

$$E(I) = E_0 - 2M_S V_a(H + \xi I) \tag{5.2}$$

where V_a, E_0, I are the activation volume, the potential barrier in the absence of current, the applied current, respectively. ξ represents the spin torque efficiency. Experimentally, the value of ξ can be obtained by comparing the influence of the applied current and the applied field on DW depinning. As consequence, the model showed that ξ is proportional to the non-adiabatic spin torque term and is given by:

$$\xi = \beta P \frac{h}{e} \frac{\Delta x}{\lambda} \tag{5.3}$$

where β is the nonadiabatic spin torque term, P is current polarization,Δx is the width of the pinning potential and λ is the DW width. The experimental values of beta are determined by fitting the slopes of $ln\tau$ as a function of current and by assuming that $\triangle x = \lambda$.

Experimentally, time resolved measurements have been used to study DW depinning under influence of currents in both perpendicular magnetization [44, 33, 67] and planar magnetization systems [133].

Performing the time resolved experiments of DW depinning based on EHE and GMR measurements, the refs. [67, 33] showed that the application of a current and an applied field affects on the stochastic behavior of DW depinning in the same way. The characteristic depinning time τ was found to vary exponentially with the current which suggested that the spin torque acts as an effective field (*cf.*, figs. 5.4).

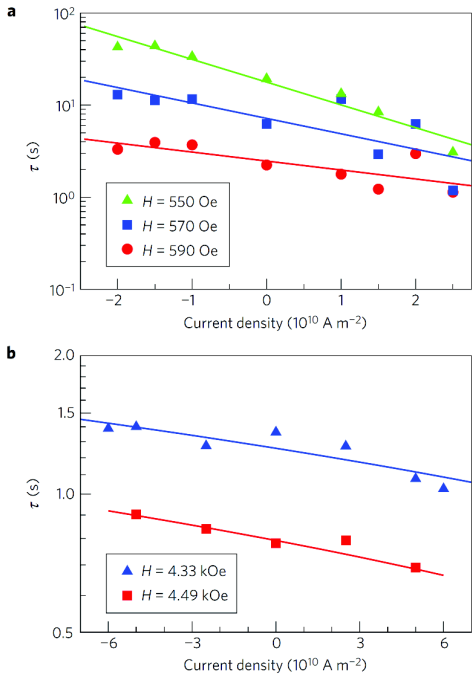

Figure 5.4: Mean pinning time of DW as a function of the applied current density for different magnetic field values for (a) CoNi and (b) FePt. The symbols represent experimental data and the solid lines represent a linear fit on a log scale (Figures are reproduced from ref. [33]).

The variation of the mean pinning time is equivalent under applied fields and currents and allows one to define the spin torque efficiency in such systems. For instance, Mihai *et al.*, [67] found the same values of spin torque efficiency $\xi = 1.10^{-13} T.m^2/A$ for both FePt single layer and FePt based spin valve. Furthermore, Burrowes *et al.* [33] calculated the nonadiabatic term $\beta = 0.022 \pm 0.002$ for CoNi and $\beta = 0.06 \pm 0.03$ for FePt which are close to the value of the Gilbert damping constant, $\alpha_{CoNi} = 0.032 \pm 0.006$ and $\alpha_{FePt} = 0.1$. As the DW width in FePt ($\sim$ 1 nm) is much smaller than in Co/Ni (~10 nm), the authors conclude that β seem to be independent of the DW width. The origin of β could then be due to the magnetic dissipation processes. In those experiments, the current density was small and heating effect can be supposed to be negligible.

Another case, using real time Lorentz microscopy to image the hopping of DW between two metastable states in NiFe nanowires, Eltschka *et al.* [133] also found that the characteristic time of DW depinning evolves linearly with the applied current. This result allows deducing the $\beta = 0.01$ for transverse wall and$\beta = 0.073$ for a vortex wall. The larger value for the vortex wall is attributed to a larger non-adiabatic contribution due to the large gradient of magnetization at the vicinity of the vortex core.

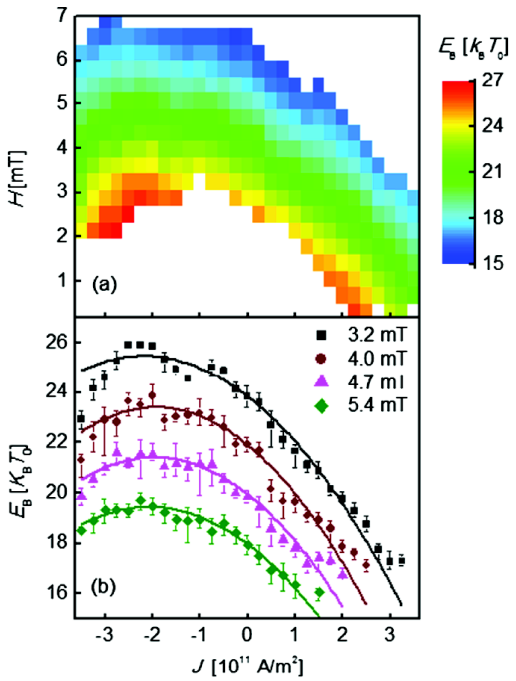

Figure 5.5: (a) Two-dimensional map of the energy barrier as a function of applied field and current which reveals a quadratic behavior. (b) Energy barrier as a function of current at several applied field values (Figures are reproduced from ref. [130]).

Recently, Kim *et al.* [130], showed that when the experimental range of the applied current is wide enough, the current dependence of the energy barrier is found to be the sum of a linear and a quadratic terms (*cf.*, fig. 5.5). The quadratic contribution of the current mainly comes from the adiabatic spin torque rather than nonadiabatic spin torque. They underlined that the analyses based solely on the linear contribution might overestimate the effect of the nonadiabatic spin torque and thus should be carefully reexamined.

5.2 Studying field and current induced domain wall depinning in FePt and NiFe nanowires

5.2.1 Detection of domain wall depinning using transport measurements

FePt-based spin-valves [FePt(5 nm)/Pd(2 nm)/FePt(5 nm)//MgO] with high perpendicular anisotropy have been grown by molecular beam epitaxy at high temperature as presented in the chapter 2. NiFe samples with 30 nm thickness were deposited by e-beam evaporation from a NiFe alloy target. Nanowires have then been processed in both kinds of layers using e-beam lithography techniques, with gold electrical contacts.

The FePt and NiFe nanowires are respectively 200 and 100 nm wide. Each device possesses a nucleation pad, used to inject a DW through the main wire (*cf.*, fig. 5.6a,c). As shown in [49, 80, 81], the coercivity of FePt nanowires is usually controlled by structural defects disposed along the wire. In narrow wires, the DW has to cross all those pinning centers sequentially, and the coercivity depend on the defect possessing the highest pinning strength.

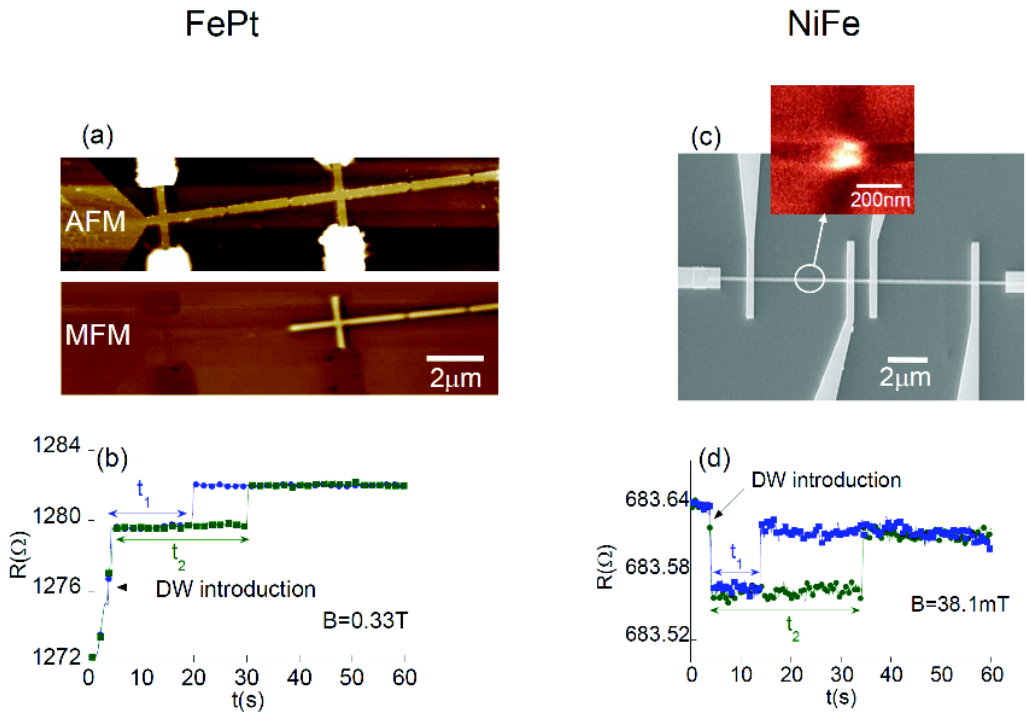

Figure 5.6: (a) AFM and MFM images of 200 nm wide FePt/Pd/FePt nanowires. The MFM image shows a single DW pinned on the constriction of the main wire. (b) Variation of the GMR as a function of time associates to the motion of DW between the two contacts. The two different pinning times obtained by repeating the measurement process illustrate the stochastic of DW depinning. (c) SEM image of 100 nm wide NiFe nanowire with a constriction, MFM image (the inset) show a DW pinned on the constriction. (d) The DW motion is probed by combining AMR and MMR measurements which also reveals the stochastic nature of the DW depinning .

At the vicinity of the coercive field, the DW thus gets pinned on this particular defect. Here, constrictions have also been disposed along the nanowire: the constriction then adds a pinning force due to DW elasticity to the already existing pinning force due to the defects present within the constriction. Several types of constrictions have been prepared: long, sharp and smooth. Indeed, MFM observations reveal that, even though in FePt DW elasticity effects are usually weak in front of intrinsic coercivity [102, 80, 81], constrictions can be used to pin reproducibly the DW at a given position (*cf.*, fig. 5.6a). In NiFe, the coercivity is essentially governed by DW elasticity (*i.e.*, the geometry of the wire), and constrictions are also patterned in order to pin the DW (*cf.*, fig. 5.6b). The position of the DW along the wire is detected

using transport techniques: small ac current ($J = 2.10^9 A/m^2, f = 1023\ Hz$ for FePt and $J = 3.10^{10} A/m^2,\ f = 6700\ Hz$ for NiFe) is injected in the main wire, while the voltage drop between two contacts is registered with lock-in technique. A field close to the depinning field of the constriction is applied along the easy magnetization axis, *i.e.,* either perpendicularly to the layer (FePt) or along the main wire direction (NiFe).

The DW position is then detected using the Giant Magneto-Resistance (GMR) effect for FePt based spin valve (*cf.,* fig. 5.6b), or a combination of Anisotropic Magneto-Resistance (AMR) and Magnon Magneto-Resistance (MMR) for NiFe (*cf.,* fig. 5.6d) [105, 72]. In both case, the observed signals indicate that a DW is injected from the nucleation pad, gets quickly pinned on the constriction where it stays for a while, before a depinning event occurs, followed by DW propagation. The applied field is adjusted so that the pinning time is around a few seconds. As observed in refs. [67, 49, 130, 33], the pinning time is found to be stochastic, and the measurement has to be repeated several times (usually 400) in order to determine the probability law associated to the pinning time.

Such probability laws can be represented using the cumulative distribution function of the pinning time $P(t)$, *i.e.*, the probability to be depinned at time t. Several series of measurements have been realized using different geometries of the constriction. The data analysis shows that, for both the FePt and the NiFe systems, three different kinds of probability laws can be identified. We indeed show that the P(t) curves can follow the regular exponential law. But also that the derivative of P(t) can be zero at t=0, or that $\lim_{t \to infinity} P(t) \neq 1$ which cannot be interpreted using a single exponential. We will show in the following that these three types of behaviors, which can be qualitatively compared correspond to three basic depinning mechanisms: the DW depinning occurs along either a simple path, serial paths, or alternative paths.

5.2.2 Simple path

As seen in figs. 5.7b, c, in the case of a simple path, the P(t) curve can be fitted by an exponential law [49]:

$$P(t) = 1 - exp\left[-\frac{t}{\tau}\right] \tag{5.4}$$

Where τ, the mean pinning time, depends on the attempt frequency f_0 and on the energy barrier height $E(H)$:

$$\frac{1}{\tau} = f_0 exp\left[\frac{E(H)}{k_B T}\right] \tag{5.5}$$

This stochasticity corresponds to the random crossing of a single energy barrier due to thermal activation. It has been already observed by Eltschka *et al.* in a system with planar

magnetization [133].

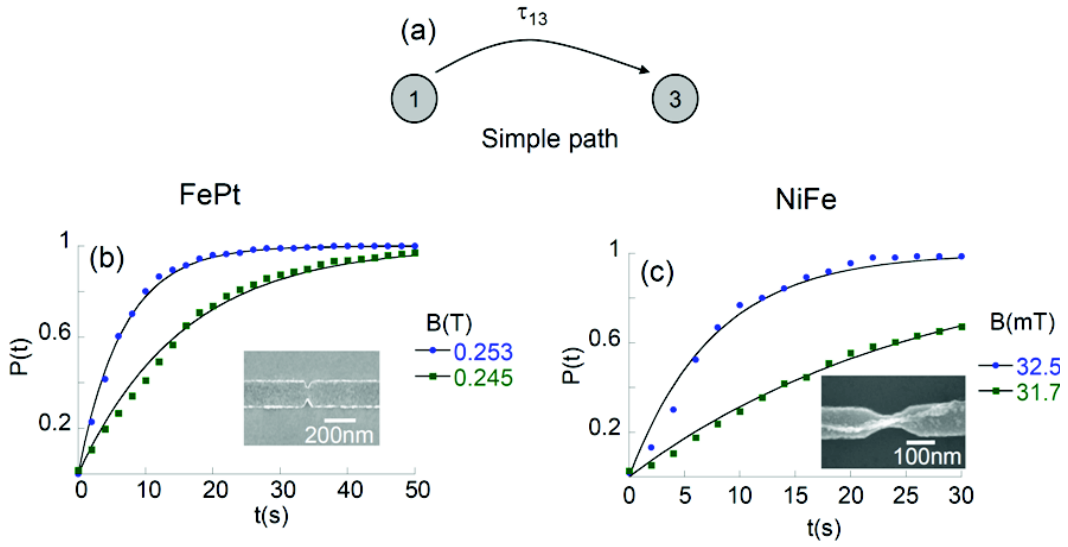

Figure 5.7: (a) Schematic illustration of DW depinning process following the simple path. Cumulative probability function P(t) of depinning at different constant magnetic field following the single exponential law for (b) FePt and (c) NiFe. For FePt, a sharp constriction is used and a smooth constriction for NiFe.

Such behaviour can also be reproduced by micromagnetic simulations taking into account thermal activation [135, 134]. In perpendicular systems, this behaviour has been observed in CoNi and CoPt with constrictions [33, 130]. However, the behaviour have never been observed in FePt nanowires without constrictions [49, 33, 67]. The appearance of a simple exponential law when using the constriction of fig. 5.7b is probably due to the fact that the constriction constrains the DW, reducing the number of available pinned configurations. Therefore, there remains only one configuration for the pinned state, and the depinning involves a single energy barrier.

In the range of studied fields, the energy barrier is found to vary linearly, accordingly to the simple 1D model,

$$E(H) = E_0 - 2HV_aM_S \tag{5.6}$$

with M_S (FePt) =1.03.10^6A/m, V_a being the magnetic volume reversed by the elementary depinning process in the activated state (activation volume) and E_0 the energy barrier at zero field.

This expression is linked to τ_{13} through Eq. 5.5 which is linearly dependent on the applied field (*cf.*, fig., 5.8). Based on this analysis, we then obtain: $V_a = 266\ nm^3$,$E_0 = 1.44\ eV$ and $V_a = 2613\ nm^3$,$J = 1.7\ eV$ for FePt and NiFe, respectively. The activation volume in NiFe is found to be one order of magnitude larger than that of FePt which might be due to the

larger DW width in NiFe.

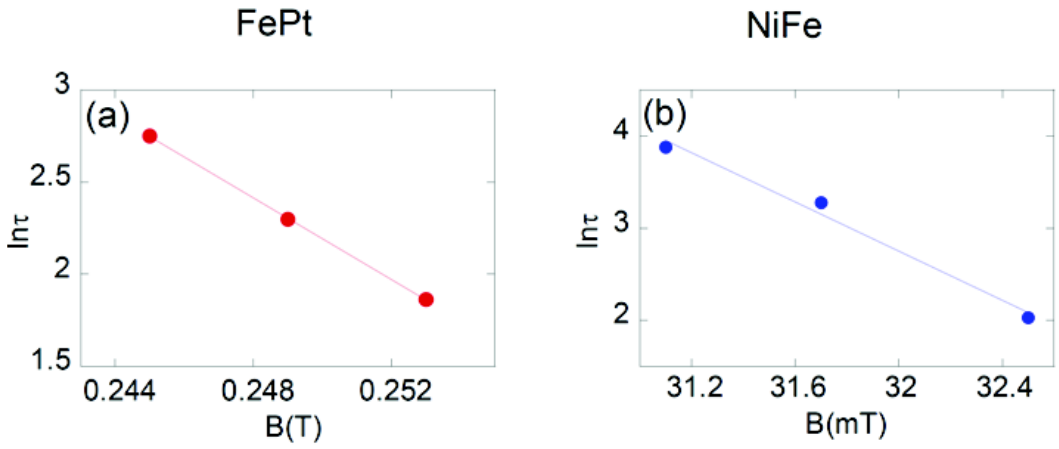

Figure 5.8: Characteristic pinning time as a function of the applied field for (a) FePt and (b) NiFe. The symbols represent experimental results and the solid lines illustrate a linear fit on a log scale .

5.2.3 Serial paths

In fig. 5.9b, c appear a yet unobserved behaviour, with a derivative of P(t) equal to zero at t=0. We propose that this behaviour is due to a depinning process along serial paths: the DW has to cross sequentially two energy barriers to get depinned, as schematically illustrated in fig. 5.9a.

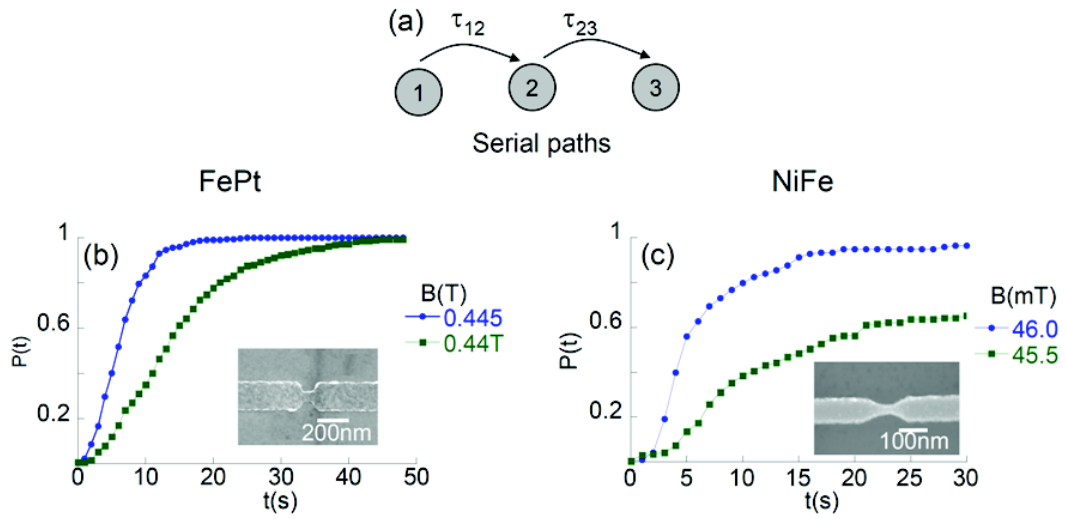

Figure 5.9: (a) Schematic illustration of depinning process following the serial paths. Cumulative probability function P(t) of depinning at different constant magnetic field for (b) FePt and (c) NiFe. For FePt a long constriction is used and a smooth constriction for NiFe.

In this figure, state 1 is the first pinned state, state 2 the second pinned state, and state 3 the depinned state. In both states 1 and 2, the DW is in the constriction, but they correspond to different micromagnetic configurations or position. It is possible to calculate P(t) using the fact that the depinning process is a Markov homogeneous process: under the influence of the applied field and of the temperature, the system jump stochastically from one state i to an other state j with a frequency $\frac{1}{\tau_{ij}}$. Let us note $\overrightarrow{\Omega}(t)$ the vector whose i_{th} component is the probability to be in the i^{th} state at time t. For example the DW is always pinned in state 1 at t=0, and thus the initial condition can be written $\overrightarrow{\Omega}(0)=\begin{bmatrix} 1 \\ 0 \\ 0 \end{bmatrix}$. The Markov matrix corresponding to this sequential paths case is:

$$M = \begin{bmatrix} -\frac{1}{\tau_{12}} & \frac{1}{\tau_{12}} & 0 \\ 0 & -\frac{1}{\tau_{23}} & \frac{1}{\tau_{23}} \\ 0 & 0 & 0 \end{bmatrix} \tag{5.7}$$

The evolution of the system is then given by the differential equation which leads to $\frac{d\overrightarrow{\Omega}(t)}{dt} = M.\Omega(t)$

$$P(t) = \overrightarrow{\Omega}(t) \begin{bmatrix} 0 \\ 0 \\ 1 \end{bmatrix} = \begin{bmatrix} 1 \\ 0 \\ 0 \end{bmatrix} exp\,[tM] \begin{bmatrix} 0 \\ 0 \\ 1 \end{bmatrix} \tag{5.8}$$

And finally:

$$P(t) = \frac{\tau_{12}\left(1 - e^{-\frac{t}{\tau_{12}}}\right) - \tau_{23}\left(1 - e^{-\frac{t}{\tau_{23}}}\right)}{\tau_{12} - \tau_{23}} \tag{5.9}$$

In one FePt device, we managed to observe more closely this phenomenon. The pinning on the constriction is evidenced by a plateau in the GMR signal. Low-noise measurements show that it is actually divided in two sub-plateaus, corresponding to two different micromagnetic states of the pinned DW, *i.e.,* to the states 1 and 2 of our analysis (*cf.,* fig. 5.10). A statistical analysis shows that, in accordance to our model, state 1 always appears before state 2, and that the pinning times in state 1 and in state 2 both follow exponential laws, whereas the overall pinning time on the constriction follow the probability law of equation 5.9 (*cf.,* fig. 5.10b) (Further analysis will be given in appendix C)

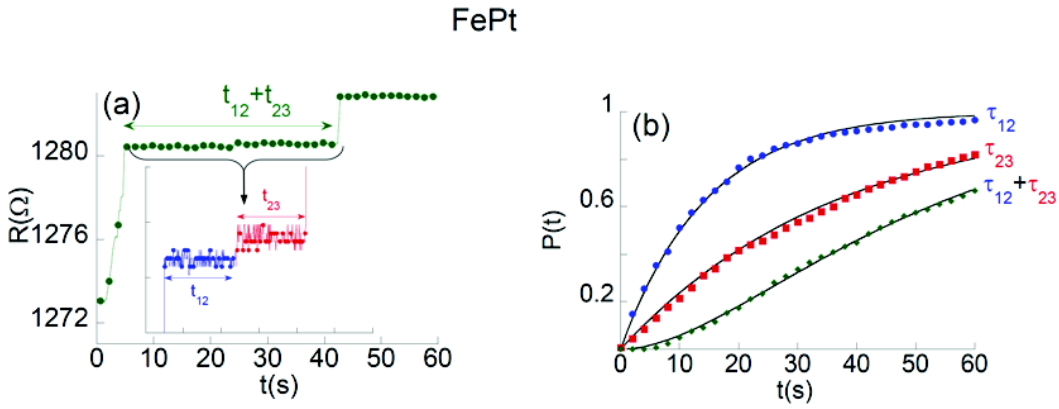

Figure 5.10: (a) Variation of GMR as a function of time showing two different steps of resistance which correspond to two different positions of the pinned DW. In this case, the variation of the resistance associated to the distance between two positions is approximately 30-100 nm. (b) Cumulative functions P(t) of DW pinned on the two different positions (blue and red curves). The corresponding processes follow a single exponential law with mean time τ_{12} and τ_{23}, respectively. The green curve is for the total pinning process .

5.2.4 Alternative paths

The third depinning behavior appears in Figs. 5.11 and corresponds to alternative path. This case also involves three states: in states 1 and 2, the DW is pinned on the constriction, but along different micromagnetic configurations, and in state 3 the DW is depinned.

It has been shown in planar systems that different kind of DW (chirality of the DW [138, 139, 140], or DW type [141, 123, 131, 132, 142] could lead to different depinning fields, or to different depinning currents [143, 42, 15].

Here, let us assume that the depinning field of state 1 is lower than that of state 2, and that the applied field is somehow in-between these depinning fields. If the DW is pinned in state 1, it can get depinned by thermal activation, which leads to the exponential-like behaviour of P(t). However, when pinned in state 2, it stays forever in state 2, which gives account of the non-saturation of P(t).

One question remains to be answered in order to fit our data: how can one calculate the probabilities to be pinned along state 1 or state 2? In refs. [49], it has been proposed that the whole phenomenon could be treated as a Markov process, as represented in fig. 5.12. In a sense, this alternative paths is similar to the crossing of two barriers in parallel.

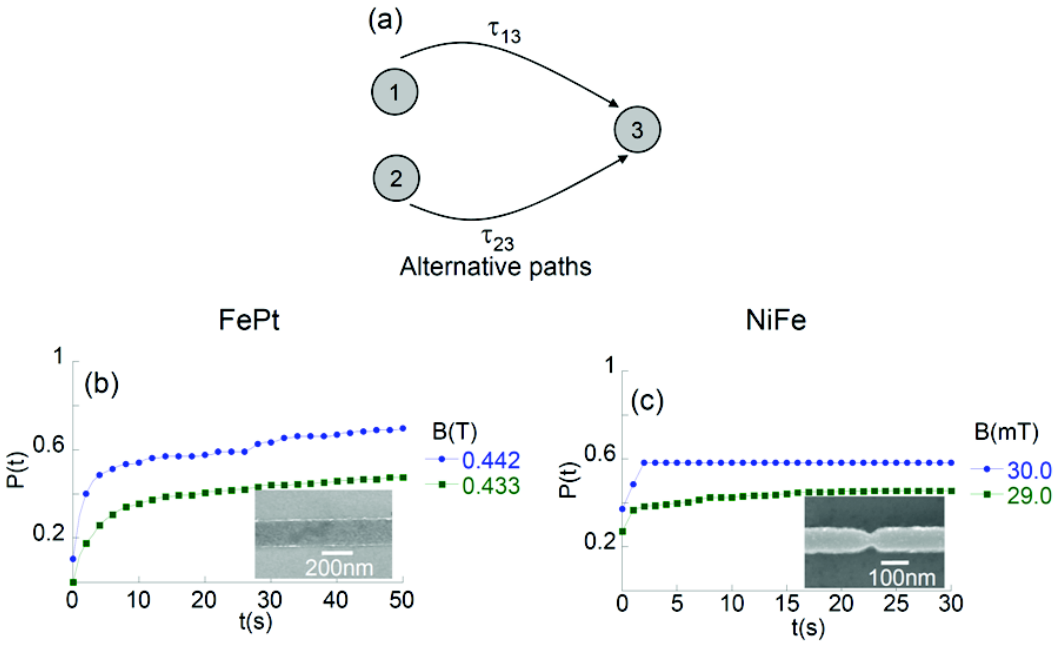

Figure 5.11: (a) Schematic illustration of depinning process following the alternative paths. Cumulative probability function P(t) of DW depinning at different constant magnetic field for (b) FePt and (c) NiFe .

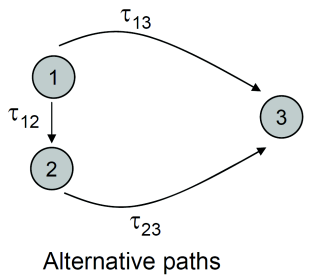

Figure 5.12: Scheme of the possible reversal states involved in the Markov process where DW begin in state 1 and jump to either state 2 or directly to state 3.

In this case, the DW begins in state 1 and jumps either to state 2, either to state 3. This model assumes that the DW can change its configuration from 1 to 2 while remaining pinned, in a way similar to the thermally activated transitions from one wall type to another (transverse-vortex) in ref. [141] or to the vortex switching process in ref. [144].

In our experiments, the transition rate from state 2 to state 3 being very low, on the time scale of the experiments, once in state 2 the DW is stuck. The probability to get stuck is thus given by the difference between τ_{12} and τ_{13}: If $\tau_{13} \ll \tau_{12}$ one retrieves an exponential law of parameter τ_{13}. If $\tau_{13} \gg \tau_{12}$ then P(t)=0.

In ref. [131], Briones *et al.* also observed a behavior corresponding to the alternative path, but found that in some devices the proportion of each type of DW, *i.e.*, the probability to be in

state 1 or 2, depended only on the injection process, and was therefore field independent. This is not what is seen in our experiments: for instance, in figs. 5.11b, c, where changes of the applied field give different probabilities for the DW to get stuck in state 2. In fig. 5.11c, the reported case for NiFe, τ_{13} is small with $P(t=0) \neq 0$. In both FePt and NiFe, our data can be fitted using the Markov process of fig. 5.12 [49], were the Markov matrix can be written:

$$M = \begin{bmatrix} -\left(\frac{1}{\tau_{12}} + \frac{1}{\tau_{13}}\right) & \frac{1}{\tau_{12}} & \frac{1}{\tau_{13}} \\ 0 & -\frac{1}{\tau_{23}} & \frac{1}{\tau_{23}} \\ 0 & 0 & 0 \end{bmatrix} \tag{5.10}$$

Leading to:

$$P(t) = 1 - (1-r)e^{-t\left(\frac{1}{\tau_{12}} + \frac{1}{\tau_{23}}\right)} - re^{-\frac{t}{\tau_{23}}} \tag{5.11}$$

where $r = \frac{\frac{1}{\tau_{12}}}{\frac{1}{\tau_{12}} + \frac{1}{\tau_{13}} - \frac{1}{\tau_{23}}}$

It is possible to imagine a more complex process with n states. In such case, it is possible to construct the corresponding $n \times n$ Markov matrix, and to solve the differential equation. Any possible process would combine both serial and alternative paths: the mechanisms observed here are therefore the elementary building block of any depinning mechanism. As an example, Fig. 5.13 shows a complex process with 4 states in which the pinning time can be calculated based on the Markov matrix 5.12.

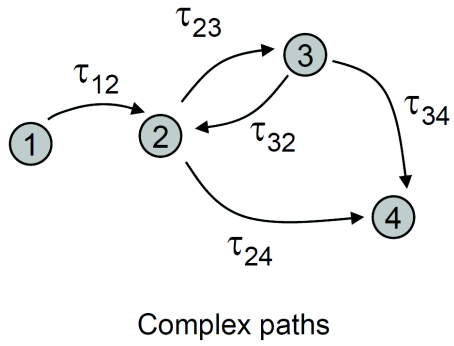

Figure 5.13: An example of a complex depinning process with 4 states which combines both serial and alternative paths.

$$M = \begin{bmatrix} -\frac{1}{\tau_{12}} & \frac{1}{\tau_{12}} & 0 & 0 \\ 0 & -\left(\frac{1}{\tau_{23}} + \frac{1}{\tau_{24}}\right) & \frac{1}{\tau_{23}} & \frac{1}{\tau_{24}} \\ 0 & \frac{1}{\tau_{32}} & -\left(\frac{1}{\tau_{34}} + \frac{1}{\tau_{32}}\right) & \frac{1}{\tau_{34}} \\ 0 & 0 & 0 & 0 \end{bmatrix} \tag{5.12}$$

Note that the proposed analysis can also deal with cases where both τ_{ij} and τ_{ji} are finites, which would lead to DW jumps forward and backward from state i to state j, and thus to

telegraphic noise as seen in [145, 146, 133]. In this case, τ_{ji} element should be introduced into the matrix. Also, for a process constituted of a large number N of sequential path of equal transition rates τ, the distribution of the total pinning time should resume to a narrow Gaussian distribution centered around $N\tau$. When N becomes large enough, there is consequently a transition from a stochastic to a reproducible behaviour, as seen in [147].

5.2.5 Effect of applied current on domain wall depinning in FePt and NiFe nanowires

The statistical analysis of pinning times thus provides an insight of the mechanisms involved during the field-induced DW depinning. It has been shown previously that it provided a way to measure the spin-torque efficiency [33, 67].

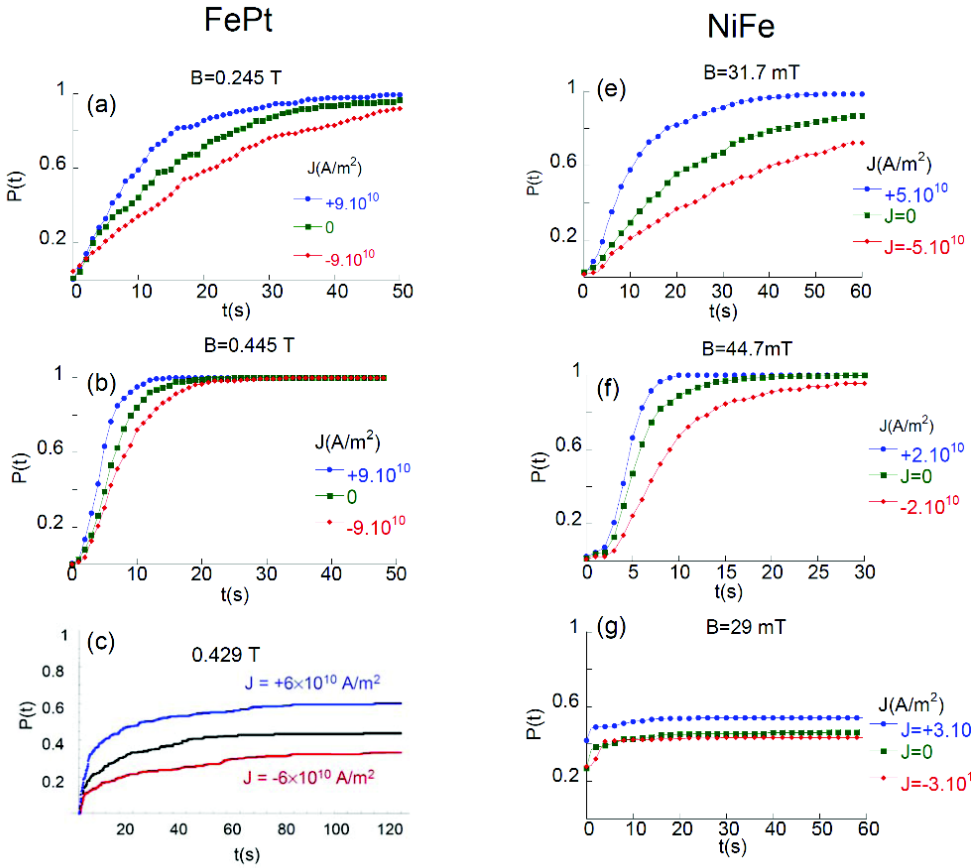

Figure 5.14: Cumulative probability functions P(t) of depinning at constant magnetic field for various currents. These curves show the bipolar effect of the current on the depinning probability by spin transfer torque. In both FePt and NiFe systems the current-field equivalence can be generalized for the three kind of paths, (a, e): simple path, (b, f): serial paths, (c, g): alternative paths.

In perpendicularly magnetized systems, and for the simple and alternative path, adding a

DC current was found to be equivalent to change of the applied field. A similar behaviour has been shown for a simple path in a planar system in ref. [133] (see ref.[148] for a review article addressing the field-current equivalence problem).

Here, we show in figs. 5.14 that in both systems the current-field equivalence can be generalized for the three kinds of paths. In our convention, a positive current adds to the action of applied field and decreases the pinning time whereas a negative current reduces this action and increases the pinning time. The bipolar effect is found probably because in such experiment the action of small current densities can be studied.

Extraction of the data obtained for the simple path show that $ln(\tau_{13})$ varies linearly with both the field and the applied current (*cf.*, fig. 5.15). Note that Kim *et al.* [130] recently observed in Co/Pt nanowires an additional quadratic dependence of $ln(\tau_{13})$ with the current, attributed to the adiabatic spin-transfer torque.

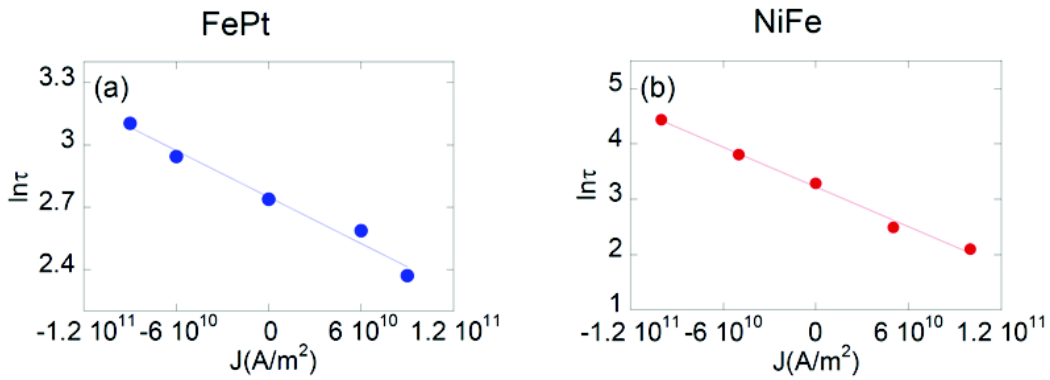

Figure 5.15: Characteristic pinning time as a function of the applied currents for (a) FePt and (b) NiFe. The symbols represent experimental results and the solid lines illustrate a linear fit on a log scale.

Here, we did not observe such effect, probably because of the weakness of the current densities applied to our systems. Whatever, we show that the efficiency of the spin transfer relatively to the applied field can be measured using the same experimental method in materials possessing very different coercivities. The obtained values are $\xi_{FePt} \sim 4.10^{-13}\ T.m^2/A$ in agreement with previous values measured in FePt [33, 67] and $\xi_{NiFe} \sim 1.10^{-14} T.m^2/A$ higher than that in ref. [149].

5.2.6 Effect of the constrictions on domain wall depinning

In fact, we have performed a large number of measurements for each kind of pinning site and we now try to conclude which depinning behaviour is associated for both systems. In the case of FePt nanowires having a Bloch wall, the mechanism is seem to be dependent on the geometry of the constrictions. As an example, the table 5.1 summaries the effect of

the type of defect on the depinning process in which each set of data is average of at least three different devices. This reveals that the DW depinning from a sharp constriction favors a simple path, that long constriction leads to serial paths and structural defects of straight wire are responsible for alternative paths. From the statistic analysis based on different models proposed above, we can estimate the basic parameters for thermal activation process which is also summed up in the table 5.1 (the data of serial paths are given for state 1). Although the mechanisms are very different, the activation volume and energy barrier are found to be of the same order of magnitude. This might suggests that the structural defect in FePt still affect on DW depinning process, having the same microscopic influence. The constriction acts as a filter that select one particular defect controlling the propagation as the width for the reversal modes in chapter 2.

On the other hand, in case of NiFe nanowires, due to different DW configurations, it is difficult to predict which kind of constriction is responsible for such depinning behaviors. We observed that the sharp constriction is quite reproducible with alternative paths while smooth constriction favors sometime either simple or serial path. In fact, the signal provided by the combination of AMR and MMR measurement of NiFe nanowires is quite small, we did not observe the displacement of DW between two different state as was observed in FePt based spin valve sample or the change of DW configuration (for example, from vortex to transverse). This discrepancy might be due to the much large size of the DW that can be less controlled by structural defects. Further studies are required for better understanding of such behavior.

Type of defects (FePt)	Depinning process	E_0(eV)	$V_a(nm^3)$	STT efficiency ξ(T.m^2/A)
Sharp constriction	Simple path	1.3	350	$4.5.10^{-13}$
Long constriction	Serial paths	1.6	230	5.10^{-13}
Structural defect [67]	Alternative paths	1.0	100	1.10^{-13}

Table 5.1: Evolution of DW depinning process for different type of defects for FePt nanowires.

Conclusions

In this chapter, we showed that the depinning mechanism is found to depend on the nature of the defect or of the geometry of the constriction. For wire dimensions where microscopy techniques become ineffective, and because the importance of intrinsic defects complicates the use of micromagnetic simulations, it is yet difficult to predict which kind of constriction should lead to which depinning behaviour. Here, we showed that the statistical study of DW depinning allows obtaining detailed information about the depinning mechanism. In both planar and perpendicular systems, the basic elements of any depinning mechanism have been observed and identified. It consists of the possibility of single, serial or alternative path. Their

signature on the statistic have been identified. Finally, all depinning mechanisms are found to react identically to variations of field or to the addition of a DC current.

Conclusions and perspectives

General conclusions

This thesis deals with two basic questions related to spintronics: the detection and the manipulation of the magnetization reversal in ferromagnetic nanostructures. The obtained results and the most significant contributions can be summarized as follows:

Controlling magnetization reversal modes in FePt nanowires: We thoroughly studied the magnetization reversal of FePt from thin films to ultra-narrow nanowires, having very high magnetocrystalline anisotropy, using magneto-transport and magnetic imaging techniques (chapter 2). We showed that the magnetization reversal of such layers is dominated by DW propagation and DW pinning on structural defects. For FePt nanowires, we found that the magnetization reversal process is strongly dependent on the wire dimensions with respect to four different length scales: the dendrite width, the disorder length, the mean edge roughness and the nucleation length. We indeed showed the transition of the reversal mode from incomplete reversal to the reversal by propagation of a single DW by decreasing the wire width below the dendrite width. Further deceasing the wire width towards the disorder length and/or the mean edge roughness leads to a large increase of coercivity. This coercivity increase is accompanied to a decrease of the nucleation length, which induces a mix of DW propagation and nucleation when it becomes smaller than the wire length.

Detection of magnetization reversal in nanostructures using magnon magnetoresistance: Following the observation of MMR in FePt thin films in our group in 2008, this thesis demonstrated that MMR measurement can be used to detect the magnetization reversal in nanostructures with either perpendicular (FePt) or planar magnetization (NiFe) (chapter 3 and 4). We showed that MMR can be used in nanowires and nanomagnets, in particularly, to detect DW position and to follow the dynamic of DW propagation along the nanowires processed in a single material.

Additionally, the expanding application of MMR measurement to NiFe nanowires will provide further understanding of the MR signature in ultra-narrow nanowires with in-plane magnetization in which the effect of AMR tends to disappear.

Dynamic of domain wall depinning in nanowires: We observed three different features of DW depinning under field and current actions in both FePt and NiFe systems which depend on the nature of defects or the geometry of the constriction. Statistical analysis using the cumulative distribution function of the pinning time P(t) showed that such depinning process can be described as simple path, serial paths or alternative paths.

Although, the results were statistically analyzed based on a large number of experiments, it is difficult to give a final conclusion on which kind of constriction is responsible for such depinning behaviors for both systems. Nevertheless, these statistical analysis of DW depinning using simple magneto-transports measurements provide an unique insight of the depinning process in narrow nanowires which might be impossible using the imaging techniques. Finally, the effect of DC current on all depinning mechanisms is found to be equivalent to the effect of applied field which allow one to extract the spin torque efficiency in these systems.

During this PhD thesis in experimental physics, I had the chance to learn different aspect in the nanofabrication, magneto-transport, characterization and modeling in the field of nanomagnetism and spintronics. I developed the fabrication process, from thin films deposition using e-beam evaporation and MBE, to the nanofabrication process using optical and e-beam lithographies, ion milling, lift-off.... Finally, I realized all the sample characterizations (SEM, AFM, MFM, Kerr...) and the transport measurements.

Perspectives

Although materials with perpendicular magnetization are very promising for spintronics applications, the appearance of the mix of propagation and nucleation due to the decrease of the nucleation length in narrow nanowires with strong disorder as FePt material can be an obstacle for application when pushing the scalability of the DW based devices towards ultimate sizes. The question is that which systems can be used to solve this problem? We suggest that systems with weaker disorders can be good candidates, for example CoNi, CoPt, CoFeB... These systems can partly avoid the increase of coercivity when reducing the width to narrow nanowires. However, in very narrow wires, DW elasticity and edges defects could lead to an increase of propagation fields which can give rise to the mix of different magnetization reversal modes. This aspect needs to be checked in the near future.

MMR signal is not so high for practical applications, but it can be an useful tool to study magnetization reversal in nanostructures since its variation depends on the magnetization orientation. Notably, it can be used for a single material, even measured using two probes configuration. For example, one can use it to probe magnetization switching, the magnetization orientation of narrow ferromagnetic nanowires in such complex geometry as lateral spin valves [39]. Time-resolved study of DW dynamic in novel perpendicular magnetization

systems for current-induced DW propagation as $CoNi$, $AlO_x/Co/Pt$, $CoFeB$... [66] are also promising since it is more versatile in comparison with commonly used EHE [32]. Moreover, the disappearance of AMR for narrow wire with in-plane magnetization will make MMR the only available tool to detect magnetization reversal in such nanowires. In any case, one need to take into account MMR when interpreting quantitatively the MR curves of ferromagnetic materials.

Spin torque studied using spin polarized currents face several problems as the additional contribution of Joule heating and Oersted field. Pure spin current arising from spin accumulation or spin Hall effect can be an efficient ways to eliminate them. Understanding the mechanism of DW depinning and using MMR to detect DW position during its propagation in nanowires can push forward the study of magnetization reversal and DW depinning based on pure spin current. The non-local geometries should be applied to the study of DW depinning by pure spin currents. Constrictions can be placed at such position in lateral spin valves that spin current could be absorbed at the vicinity of DW. Moreover, the spin torque could be then tested in other geometries, for example in the case of a vertical spin current.

Appendix A

Sample preparation

A.1 FePt thin films deposition

A.1.1 Description of the Molecular Beam Epitaxy system

In principle, Molecular Beam Epitaxy (MBE) uses atomic or molecular beams as a source of materials for deposition on the surface of a substrate.

MBE is considered as an ideal approach for thin film deposition since it can precisely control the beam fluxes and the growth conditions. Working in ultra high vacuum chamber (typically in order of 10^{-10} Torr) minimize the contamination of the deposition.

The system that we used consists of three main chambers: a load-lock chamber for the introduction of the sample without breaking the vacuum of the main chamber, a preparation chamber where substrates are degassed and a deposition chamber for growing samples (cf. fig.A.1)

For our growths, we used electron bombardment evaporators. The Fe and Pt targets are placed in copper crucibles cooled by a circulation of water to avoid the chemical interaction between the target and the crucible. The evaporation process is provided by an electron beam generated by a Tungsten filament raised to high temperature. Following, the electrons are accelerated by a high voltage (10 keV) to evaporate the material. The deflection of electron beam is done by two magnetic coils which allow scanning the beam on the surface of the target

Liquid N_2 is used to cool down some parts of the deposition chamber, in order to add some cryogenic pumping power and increase the pumping efficiency of Ti deposits. The deposition rate is regulated through the quartz balance receiving the flux of materials simultaneously with the substrate.

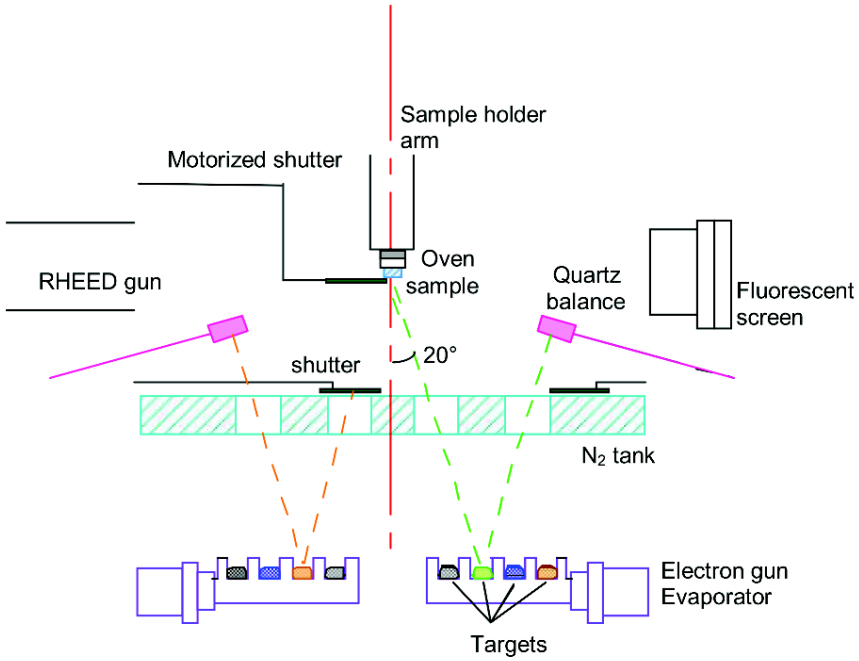

Figure A.1: Schematic of the MBE evaporation chamber.

In our MBE, reflection high energy electron diffraction (RHEED) with a electron source up to 30 kV is present. It allows characterizing the surface of crystalline films during and after deposition process.

A.1.2 FePt deposition process

We used MgO substrate because it can provide several advantages for our studies:

- It can be used at high temperature which is a requirement for the formation of L_{10} FePt phase.

- MgO has a lattice constant a = 4.219 Å which allows the epitaxial growth of FePt (a=3.86 Å)

- MgO is an insulating oxide. It will be good for transport measurements afterward since it can avoid the current flow into the substrate.

However, using MgO substrate has also occurred some difficulties as its surface is very sensitive with environment, discharging effect during nanofabrication process of electron beam lithography.

In our studies, we deposited directly FePt films on MgO substrates, therefore the preparation of substrate is important because it can affect easily the quality of samples, *e.g.*, the fluctuation of the coercivity field. The cleaning process of MgO substrate can be divided into two steps as follows:

Ex-situ cleaning: - Degreasing in boiling Dichloromethane

- Cleaning in an acetone bath

- Rinsing in an ethanol bath and it is finally dried up using flow of N_2 gas.

In-situ cleaning: - Following, MgO substrate is bonded on sample holder using Indium and introduced into the introduction chamber for degassing in few hours at high temperature under vacuum. This process is used to eliminate all adsorbed species as water, CO, hydrocarbon... being on the surface of MgO prior to the growth of FePt.

Our FePt films were deposited using co-deposition of Fe and Pt at 500^oC. The deposition rate is regulated around 0.6 Å/s. For FePt based spin valve films, Pd spacer layers were deposited at lower temperature (330^oC) to avoid the diffusion. The deposition process is followed in-situ using RHEED. Finally, prior to nanofabrication process, magnetic properties of FePt films were also checked ex-situ by hysteresis loop of EHE measurements.

A.2 Nanostructures fabrication

Almost all our nanodevices were studied by magneto-transport measurements, therefore, several steps of lithography are required to create electrical contacts and the nanowires. Basically, fabrication process of NiFe and FePt nanowires are similar except the last steps of mask remover. In the following, we will briefly explain step by step the nanofabrication process.

A.2.1 Optical lithography

We use optical lithography process to define the large electrical contacts and the alignment marks which are required for the e-beam lithography step. The process is basically similar as the process of e-beam lithography in fig. A.2 except the exposure is done with UV source instead of e-beam.

1. A photo-resist layer is firstly coated on either surface of silicon substrate for NiFe samples or FePt for FePt samples.

2. The design on the optical mask is then replicated on the resist using an UV with wave length $\lambda = 365nm$.

3. For positive resist, the exposure part is selectively removed in AZ photoresist developer in 30 second and rinsed in water in 30 second.

4. The patterns on the resists are used as a template for deposition of 5 nm of Ti and 100 nm of gold.

5. Finally, the remaining parts of the resist is removed in acetone using the lift-off process.

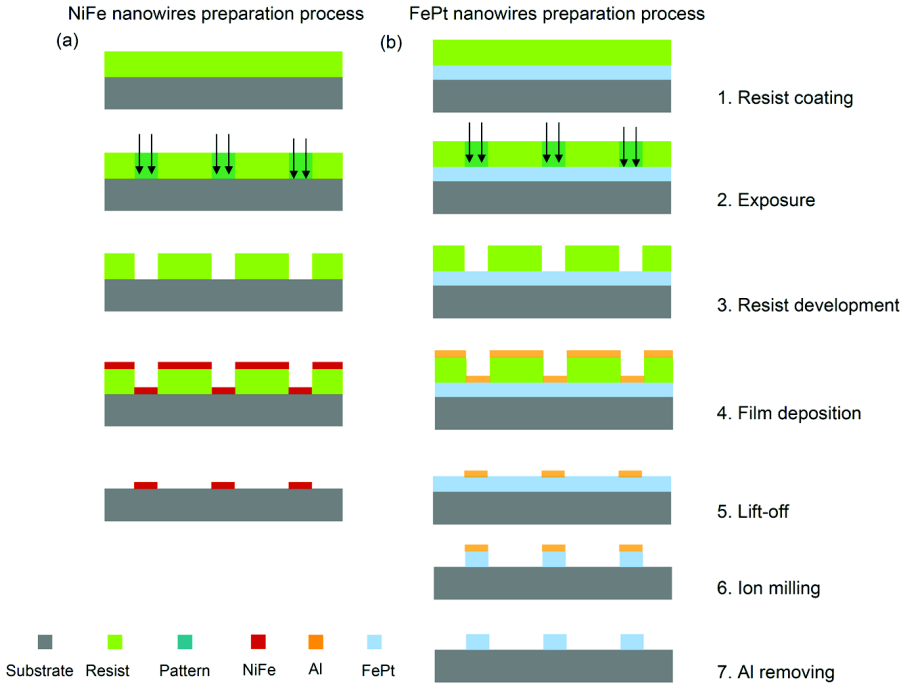

Figure A.2: (a) NiFe and (b) FePt nanowires fabrication process using e-beam lithography.

A.2.2 E-beam lithography

We use two steps of e-beam lithography: The first one is the creation of main wire and the second one is used to connect nanowires to the large electrical pads. Principle of the process can be followed as schemes in fig. A.2.

1. A positive e-beam resist layer of PMMA layer is deposited on the surface of the sample using spin coating, followed by 5 min baking at 180^oC to remove solvent and to achieve the homogeneous distribution of resist on the substrate. The thickness of PMMA layer is approximately of 120 nm.

2. E-beam of a JOEL nanowriter is used to directly write the patterns on the samples. This system works at 100 kV and provide a typical resolution around 7-10 nm in the used conditions and overlay alignment around 30 nm.

3. PMMA resist is then developed in MIBK and Isopropanol solution (ratio 1:3) in 30 seconds, followed by rinsing in Isopropanol in 30 seconds.

4. Deposit of 30 nm NiFe layer for NiFe samples or 20 nm Al for the fabrication of hard mask for FePt samples. This step is performed using e-beam evaporation.

5. The resist is then removed in acetone using the lift-off process. Creation of NiFe samples are done at this step. For FePt samples, it requires further process to create FePt nanowires.

6. Ion milling process using Ar^+plasma allows removing unwanted parts of FePt. The etching process is controlled by a SIMS detector, which measures the species present in the chamber during the etching process. For FePt 10 nm thick, it is usually carry out in 2 minutes

at RF power of 300 W.

7. The Al mask is removed using optical developer solution in 2 minutes. The definition of FePt nanowires is done at this step.

The second step of e-beam lithography is to connect the nanowires to the large contacts. It is basically the same procedures as for A.2a. In order to avoid the charging effect by MgO substrate on FePt sample, 20 nm Al is deposited on top of PMMA resist prior to e-beam exposure and removed before the development process. In the step of Ti/Au deposition, it is usually used an Ar^{+}beam etching process to clean the interface of the nanowires before to deposit 5nm of Ti and 100 nm of Au.

Finally, nanodevices are characterized by SEM, AFM and mostly by transport measurements.

Appendix B

Angular dependence of MMR measurements

As shown in the chapter 3, the slope of MMR is slightly changed when the applied field is rotated out of the anisotropy axis. Here, we present a simple analytical model to take into account the evolution of the MMR when the angle, ϕ of the applied field is varied. The rotation plane belongs to the *yz* plane and is orthogonal to the wire axis (*cf.*, B.1)

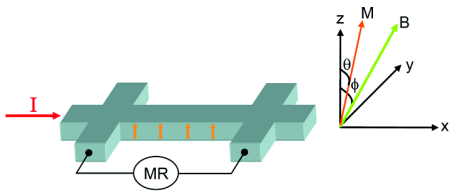

FIGURE B.1 – Schematic of MMR measurements configuration for different rotation of the applied field (ϕ) where the rotation is perpendicular to the wire axis in order to avoid AMR.

The MMR is related to the effective field. When the external field is applied along the anisotropy axis, the effective field is simply the algebraic sum of the anisotropy field and the applied, $H_{eff} = H_a + H$ .This relation catches the parallel and the antiparallel situations. However, when H is oblique, a vector expression is required. The magnetic equilibrium requires that the effective field is parallel to the magnetization giving the following equation :

$$\overrightarrow{H_{eff}} = \overrightarrow{H} + H_a(\overrightarrow{m}.\overrightarrow{k})\overrightarrow{k} = H_{eff}\overrightarrow{m}$$

Where $\overrightarrow{m}$ is the unit vector of magnetization and $\overrightarrow{k}$ is the unit vector of the easy axis (here along the z axis). H_a is the effective anisotropy field constant related to the anisotropy constant corrected by the demagnetizing energy :

$$H_a = \frac{2K_u}{M_s} - \mu_0 M_s$$

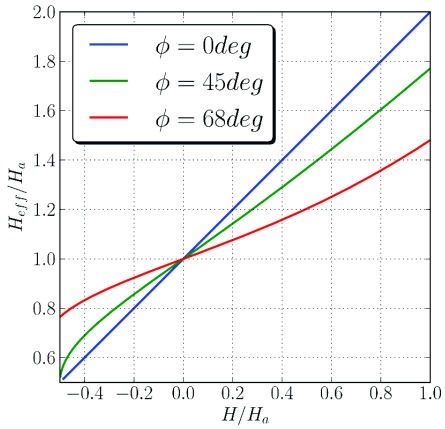

FIGURE B.2 – Variation of effective field H_{eff} as a function of the applied field H for various rotation angle ϕ of the applied field.

The vector equation can be rewritten using the angles of the magnetization, θ, and the angle of the applied field, ϕ, respect to the direction normal to the layer :

$$\begin{cases} H_{eff}\cos(\theta) = H\cos(\phi) + H_a\cos(\theta) \\ H_{eff}\sin(\theta) = H\sin(\phi) \end{cases}$$

These 2 equations allow to write the couple (H,H_{eff}) as a function of θ and to draw parametrically the curves $H_{eff}(H)$ for various angles of the applied field, fig. B.2.

$$\begin{cases} H = H_a\frac{\cos(\theta)\sin(\theta)}{\sin(\phi-\theta)} \\ H_{eff} = H_a\frac{\cos(\theta)\sin(\phi)}{\sin(\phi-\theta)} \end{cases}$$

In our case, the anisotropy field is so large with respect to the applied field that we can use the weak field approximation :

$$H_{eff} \approx H_a + \frac{\partial H_{eff}}{\partial H}_{H=0} H = H_a + \cos(\phi)H$$

It shows that oblique applied field acts as it was reduced by a factor $\cos(\phi)$. Then it should be interesting to represent the resistance of figure 3.5 in chapter 3 as a function of $H\cos(\phi)$ to see if the slopes of the MMR for various angles are close to each other. Fig. B.3 reproduced after correcting the applied field with $\cos(\phi)$, show that the slope of MMR well overlap. The small difference in the slope can be attributed to the estimation error in the real angle values.

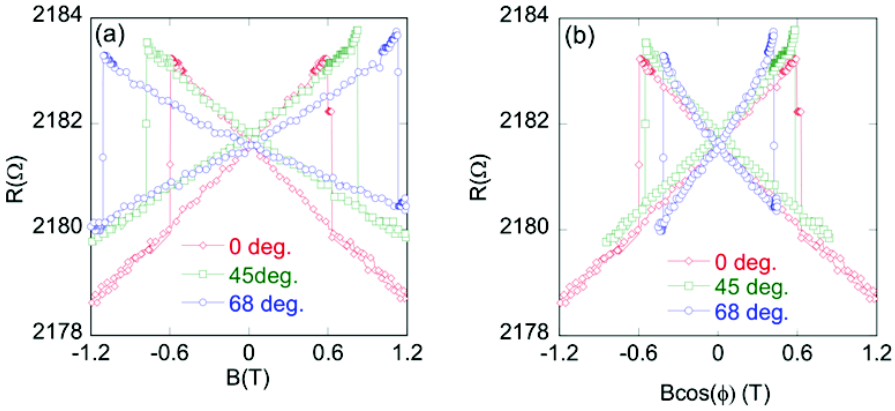

FIGURE B.3 – (a) MMR measurement for different applied field angles. (b) MMR as function of applied field corrected by cos(ϕ).

Appendix C

Further analysis of domain wall depinning by serial paths

As discussed in detailed in chapter 5, DW depinning process can follow the serial paths: the DW crossing sequentially two energy barriers to get depinned. The characteristic time of each process can be deduced by fitting the total depinning process using the following equation:

$$P(t) = \frac{\tau_{12}\left(1 - e^{-\frac{t}{\tau_{12}}}\right) - \tau_{23}\left(1 - e^{-\frac{t}{\tau_{23}}}\right)}{\tau_{12} - \tau_{23}} \tag{C.1}$$

We provide an example in fig. C.1, the experimental data can be well fitted with eq. C.1. This allows extracting the basic information of thermal activation process as pinning time, activation volume and energy barrier of each process as shown in fig C.3a and table C.3b.

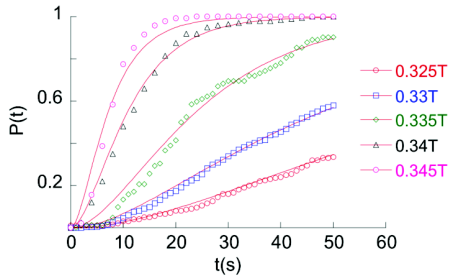

Figure C.1: Cumulative probability function P(t) of DW depinning with the case of serial path, at different constant magnetic fields . The solid lines are fits using eq. C.1.

As GMR provided a large signal, in one particular device, we could directly observe a small displacement of DW from state 1 to state 2 by GMR measurement. This allows analyzing independently each pinning state. We show in fig. C.2 that each pinning state can be perfectly fitted with one barrier process by eq. C.2. The characteristic parameters of each one is presented in fig. C.3c and table C.3d.

$$P(t) = 1 - exp\left[-\frac{t}{\tau}\right] \tag{C.2}$$

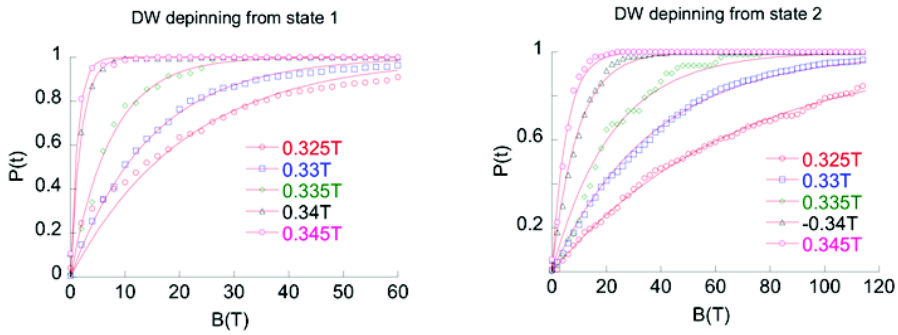

Figure C.2: Cumulative probability function P(t) of DW depinning at different constant magnetic fields for each state of pinned DW: (a) state 1 and (b) state 2 . The solid lines are for a simple path using eq.C.2

The results using the two ways are equivalent as being given in fig. C.3.

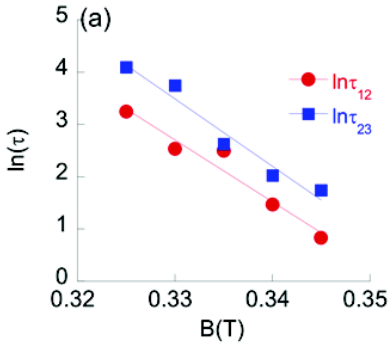

(b)

	State 1	State 2
Va (nm³)	236	258
E_0 (eV)	1.61	1.7

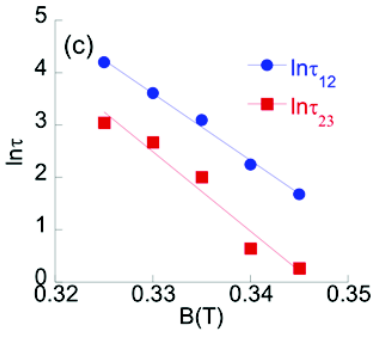

(d)

	State 1	State 2
Va (nm³)	257	305
E_0 (eV)	1.72	1.89

Figure C.3: Characteristic pinning time as a function of the applied field. The data are deduced from fitting for (a) total and (c) each depinning process. The symbols represent experimental results and the solid lines illustrate a linear fit on a log scale. Table (b) is the activation volume and energy barrier being calculated from data in (a) and (d) from data in (c).

Bibliography

[1] M. N. Baibich et al. Giant magnetoresistance of (001)fel(001)cr magnetic superlattices. *Phys. Rev. Lett.,*, 61:2472, 1988.

[2] G. Binasch et al. Enhanced magnetoresistance in layered magnetic structures with antiferromagnetic interlayer exchange. *Phys. Rev. B*, 39:4828(R), 1989.

[3] S. A. Wolf et al. Spintronics: A spin-based electronics vision for the future. *Science*, 294:1488, 2001.

[4] B. Dieny et al. Giant magnetoresistance in soft ferromagnetic multilayers. *Phys. Rev. B*, 43:1297 (R), 1991.

[5] J.S. Moodera et al. Large magnetoresistance at room temperature in ferromagnetic thin film tunnel junctions. *Phys. Rev. Lett.,*, 74:3273, 1995.

[6] M. Julliere. Tunneling between ferromagnetic films. *Phys. Lett. A*, 54:225, 1975.

[7] C. Chappert et al. The emergence of spin electronics in data storage. *Nat. Mater.*, 6:813, 2007.

[8] S. Mangin et al. Current-inducedmagnetization reversal in nanopillars with perpendicular anisotropy. *Nat. Mat.*, 5:210, 2006.

[9] T. Ono et al. Propagation of a magnetic domain wall in a submicrometer magnetic wire. *Science*, 284:468, 1999.

[10] W. Thomson. *Proc. Roy. Soc.*, 8:546, 1857.

[11] T.R. McGuire et al. Anisotropic magnetoresistance in ferromagnetic 3d alloys. *IEEE Trans. on Magn.*, 11:1018., 1975.

[12] J-E. Wegrowe et al. Magnetoresistance of ferromagnetic nanowires. *Phys. Rev. Lett.*, 82:3681, 1999.

[13] L. Vila et al. Magnetic vortices in nanowires with transverse easy axis. *Phys. Rev .B*, 79:172410, 2009.

[14] M. Klaui et al. Domain wall pinning in narrow ferromagnetic ring structures probed by magnetoresistance measurements. *Phys. Rev. Lett.*, 90:097202., 2003.

[15] M. Hayashi et al. Dependence of current and field driven depinning of domain walls on their structure and chirality in permalloy nanowires. *Phys. Rev. Lett.*, 97:207205., 2006.

[16] A. Gerber et al. Perspective of spintronics applications based on the extraordinary hall effect. *arXiv:0803.0124v1*, 2008.

[17] I. M. Miron et al. Perpendicular switching of a single ferromagnetic layer induced by in-plane current injection. *Nature*, 476:189, 2011.

[18] D. Ravelosona et al. Nanometer scale observation of high efficiency thermally assisted current-driven domain wall depinning. *Phys.Rev. Lett.,*, 95:117203, 2005.

[19] S. S. P. Parkin et al. Exchange-biased magnetic tunnel junctions and application to nonvolatile magnetic random access memory. *J. Appl. Phys.*, 85:5828, 1999.

[20] F. Hansteen et al. Femtosecond photomagnetic switching of spins in ferrimagnetic garnet films. *Phys. Rev. Lett.,*, 95:047402, 2005.

[21] L. Berger. Exchange interaction between ferromagnetic domain-wall and electric-current in very thin metallic films. *J. Appl. Phys.*, 55:1954, 1984.

[22] C. Y. Hung et al. Observation of a current induced force on bloch lines in nife thin films. *J. Appl. Phys.*, 67:5941, 1990.

[23] J.C. Slonczewski. Current-driven excitation of magnetic multilayers. *J. Mag. Magn, Mat.*, 159:L1, 1996.

[24] M. Tsoi et al. Excitation of a magnetic multilayer by an electric current. *Phys. Rev. Lett.*, 80:4281, 1998.

[25] J. A. Katine et al. Current-driven magnetization reversal and spin-wave excitations in co/cu/co pillars. *Phys. Rev. Lett.*, 84:3149, 2000.

[26] O. Boulle et al. Current-induced domain wall motion in nanoscale ferromagnetic elements. *Mat. Sci. Eng. R: Rep.*, 72:159, 2011.

[27] Stuart S. P. Parkin et al. Magnetic domain-wall racetrack memory. *Science*, 320:190, 2008.

[28] N. Vernier et al. Domain wall propagation in magnetic nanowires by spin-polarized current injection. *Europhys. Lett.*, 65:526, 2005.

[29] J. Grollier et al. Switching the magnetic configuration of a spin valve by current-induced domain wall motion. *J. Appl. Phys.*, 92:4825, 2002.

[30] M. Hayashi et al. Current driven domain wall velocities exceeding the spin angular momentum transfer rate in permalloy nanowires. *Phys. Rev. Lett.,*, 98:037204, 2007.

[31] I. M. Miron et al. Fast current-induced domain-wall motion controlled by the rashba effect. *Nat. Mat.*, 10:419, 2011.

[32] T. Koyama et al. Observation of the intrinsic pinning of a magnetic domain wall in a ferromagnetic nanowire. *Nat. Mat.*, 10:194, 2011.

[33] C. Burrowes et al. Non-adiabatic spin-torques in narrow magnetic domain walls. *Nat. Phys.*, 6:11, 2010.

[34] A. Thiaville et al. Micromagnetic understanding of current-driven domain wall motion in patterned nanowires. *Europhys. Lett.,*, 69:990, 2005.

[35] V. Uhlir et al. Current-induced motion and pinning of domain walls in spin-valve nanowires studied by xmcd-peem. *Phys. Rev. B*, 81:224418, 2010.

[36] J.-Y. Chauleau et al. Magnetic domain walls displacement: automotion vs. spin-transfer torque. *Phys. Rev. B*, 82:214414., 2010.

[37] T. Yang et al. Giant spin-accumulation signal and pure spin-current-induced reversible magnetization switching. *Nat. Phys*, 4:851, 2008.

[38] L. Liu et al. Spin-torque switching with the giant spin hall effect of tantalum. *Science*, 336:556, 2012.

[39] P. Laczkowski et al. Enhancement of the spin signal in permalloy/gold multiterminal nanodevices by lateral confinement. *Phys. Rev. B*, 85:220404, 2012.

[40] A. Hubert et al. Magnetic domains: The analysis of magnetic microstructures. *Springer-Verlag Berlin Heidelberg New York*, 1998.

[41] C. H. Marrows. Spin-polarised currents and magnetic domain walls. *Adv. Phys.*, 54:585, 2005.

[42] M. Hayashi. Current driven dynamic of magnetic domain wall in permalloy nanowires. *PhD thesis, Stanford University, USA*, 2006.

[43] L. Thomas et al. Current induced domain-wall motion in magnetic nanowires. *Handbook of Magnetism and Advanced Magnetic Materials, volume 2, JohnWiley & Sons, Ltd*, 2007.

[44] C. Burrowes et al. Role of pinning in current driven domain wall motion in wires with perpendicular anisotropy. *Appl. Phys. Lett.*, 93:172513, 2008.

[45] O. Boulle et al. Nonadiabatic spin transfer torque in high anisotropy magnetic nanowires with narrow domain walls. *Phys. Rev. Lett.*,, 101:216601, 2008.

[46] H. Tanigawa et al. Current-driven domain wall motion in cocrpt wires with perpendicular magnetic anisotropy. *Appl. Phys. Express*, 1:011301, 2008.

[47] R. Lavrijsen et al. Controlled domain-wall injection in perpendicularly magnetized strips. *Appl. Phys. Lett.*, 96:222502, 2010.

[48] F. Cayssol et al. Domain wall creep in magnetic wires. *Phys. Rev. Lett*, 92:107202, 2004.

[49] J. P. Attane et al. Thermally activated depinning of a narrow domain wall from a single defect. *Phys. Rev. Lett.*, 96:147204, 2006.

[50] B. Hillebrands et al. Spin dynamic in confined magnetic structures iii. *Springer*, 2006.

[51] J. P. Liu et al. Nanoscale magnetic materials and application. *Springer*, 2009.

[52] N. L. Schryer et al. The motion of 180° domain walls in uniform dc magnetic fields. *J. Appl. Phys.*, 45:5406, 1974.

[53] G. S. D. Beach et al. Dynamics of field-driven domain-wall propagation in ferromagnetic nanowires. *Nat. Mater.*, 4:741, 2005.

[54] D. Atkinson et al. Magnetic domain-wall dynamics in a submicrometre ferromagnetic structure. *Nat. Mater.*, 2:85, 2003.

[55] M. Muller et al. Velocity-force characteristics of a driven interface in a disordered medium. *Phys. Rev. B*, 63:184305, 2001.

[56] P. J. Metaxas et al. Creep and flow regimes of magnetic domain-wall motion in ultrathin pt/co/pt films with perpendicular anisotropy. *Phys. Rev. Lett.*, 99:217208, 2007.

[57] L. Berger. Dragging of domain by an electric-current in very pure, non-compasented. ferromagnetic metals. *Phys. Lett. A*, 46:3, 1973.

[58] L. Berger. Possible existence of a josephson effect in ferromagnets. *Phys. Rev. B*, 33:1572, 1986.

[59] A. Thiaville et al. Domain wall motion by spin-polarized current: a micromagnetic study. *J. Appl. Phys.*, 95:7049, 2004.

[60] G. Tatara et al. Theory of current-driven domain wall motion: Spin transfer versus momentum transfer. *Phys. Rev. Lett.*, 92:086601, 2004.

[61] X. Waintal et al. Current-induced distortion of a magnetic domain wall. *Europhys. Lett.*, 65:427, 2004.

[62] S. Zhang et al. Roles of nonequilibrium conduction electrons on the magnetization dynamics of ferromagnets. *Phys. Rev. Lett.*, 93:127204, 2007.

[63] Y. Tserkovnyak et al. Current-induced magnetization dynamics in disordered itinerant ferromagnets. *Phys. Rev. B*, 74:144405, 2006.

[64] I. Garate et al. Nonadiabatic spin-transfer torque in real materials. *Phys. Rev .B*, 79:104416, 2009.

[65] G. Meier et al. Direct imaging of stochastic domain-wall motion driven by nanosecond current pulses. *Phys. Rev. Lett*, 98:187202, 2007.

[66] I.M. Miron et al. Current-driven spin torque induced by the rashba effect in a ferromagnetic metal layer. *Nat. Mater.*, 9:230, 2010.

[67] A. P. Mihai et al. Stochastic domain-wall depinning under current in fept spin valves and single layers. *Phys. Rev. B*, 84:014411, 2011.

[68] T. Suzuki et al. Evaluation of scalability for current-driven domain wall motion in a co/ni multilayer strip for memory applications. *IEEE Trans. Mag*, 45:3776, 2009.

[69] Y. Li et al. Magnetization reversal of iron nanoparticles studied by submicron hall magnetometry. *J. Appl. Phys.*, 93:7912, 2003.

[70] http://www.qdusa.com/products/.

[71] A. B. Oliveira et al. Magnetization reversal in permalloy ferromagnetic nanowires investigated with magnetoresistance measurements. *Phys. Rev. B*, 78:024423, 2008.

[72] V. D. Nguyen et al. Magnon magnetoresistance of nife nanowires: Size dependence and domain wall detection. *Appl. Phys. Lett.*, 99:262504, 2011.

[73] E. M. Push. Hall effect and the magnetic properties of some ferromagnetic materials. *Phys. Rev.*, 36:1503, 1930.

[74] G. Boero et al. Submicrometer hall devices fabricated by focused electron-beam-induced deposition. *Appl. Phys. Lett.*, 86:042503, 2005.

[75] F. Cayssol et al. Detection of domain wall propagation in a mesoscopic wire. *J. Mag. Magn, Mat.*, 240:30, 2002.

[76] A. P. Mihai et al. Magnetization reversal dominated by domain wall pinning in fept based spin valves. *Appl. Phys. Lett.*, 94:122509, 2009.

[77] A. Fert. Origin, development, and future of spintronics. *Rev. Mod. Phys.*, 80:1517, 2008.

[78] T. Ono et al. Dynamics of magnetic domain walls in nanomagnetic systems. *Nanomagnetism and spintronics, Elsevier B.V.*, 2009.

[79] T. Ono et al. Magnetization reversal in submicron magnetic wire studied by using giant magnetoresistance effect. *Appl. Phys. Lett.*, 72:1116, 1998.

[80] J. P. Attane et al. Coercivity enhancement in fept nanowires due to the suppression of available paths for domain wall propagation. *Phys. Rev. B*, 84:144418, 2011.

[81] V. D. Nguyen et al. Dimensionality effects on the magnetization reversal in narrow fept nanowires. *Appl. Phys. Lett.*, 100:252403, 2012.

[82] V. Gehanno et al. Studies of epitaxial fe0.5pd0.5 thin films by x-ray diffraction and polarized fluorescence absorption spectroscopy. *J. Appl. Phys.*, 84:2316, 1998.

[83] J. P. Attane. Interactions entre parois magnétiques et defauts structuraux, et mise en ordre chimique par irradiation, observees dans des couches minces de alliages fept(pd). *PhD thesis, Université Joseph Fourier, Grenoble*, November, 2003.

[84] V. Gehanno. Anisotropie magnetique perpendiculaire des couches minces epitaxiees de alliages ordonnes fepd. *PhD thesis, Insitut National Polytechnique de Grenoble, Grenoble*, October, 1997.

[85] D. Halley. Croissance, mise en ordre chimique et relaxation des contraintes epitaxiales dans des alliages fepd et fept. *PhD thesis, Université Joseph Fourier, Grenoble*, December, 2001.

[86] A..P.Mihai. Depiegeage de parois magnetiques par activation thermique et transfert de spin dans des nanostructures de alliage fept. *Université Joseph Fourier, Grenoble*, October, 2009.

[87] J. P. Attane et al. Domain wall pinning on strain relaxation defects in fept(001)/pt thin films. *Appl. Phys. Lett.*, 79:794, 2001.

[88] T. Jourdan et al. Magnetic domain wall pinning and coercivity in fept/mgo and fept/pt thin films. *J. Mag. Mag. Mat.*, 321:2187, 2009.

[89] J. P. Attane et al. Invasion percolation universality class and fractal geometry of magnetic domains. *Phys. Rev. B*, 82:024408, 2010.

[90] D. Wilkinson et al. Invasion percolation: A new form of percolation theory. *J. Phys. A: Math. Gen.*, 16:3365, 1983.

[91] T. Seki et al. Spin-polarized current-induced magnetization reversal in perpendicularly magnetized l10-fept layers. *Appl. Phys. Lett.*, 88:172504, 2006.

[92] J. G. Zhu. Magnetoresistive random access memory: The path to competitiveness and scalability. *Proc. IEEE*, 96:1786, 2008.

[93] A. D. Kent. Spintronics: Perpendicular all the way. *Nature Materials*, 9:699, 2010.

[94] H. Zhao et al. Pinning effect and thermal stability study in l 10 fept-pinned spin valves. *J. Appl. Phys.*, 102:023909, 2007.

[95] C. H. Marrows et al. Giant magnetoresistance and oscillatory exchange coupling in disordered co/cu multilayers. *J. Phys. Condens. Matter.*, 11:81, 1999.

[96] J. Bass et al. Spin-diffusion lengths in metals and alloys, and spin-flipping at metal/metal interfaces: An experimentalist's critical review. *J. Phys. Cond. Mat.*, 19:183201, 2007.

[97] E. Paz et al. Control of magnetization reversal by combining shape and magnetocrystalline anisotropy in epitaxial fe planar nanowires. *Nanotechnology*, 21:255301, 2010.

[98] M. Brands et al. Reversal processes and domain wall pinning in polycrystalline co-nanowires. *Phys. Rev. B*, 74(17):174411, 2006. cited By (since 1996) 18.

[99] R. Hoffmann et al. Shape instability in out of equilibrium magnetic domains observed in ultrathin magnetic films with perpendicular anisotropy. *J. Mag. Mag. Mat.*, 192:409, 1999.

[100] R. Belhi et al. Magnetization reversal dynamics, nucleation, pinning, and domain wall propagation in perpendicularly magnetized ultrathin cobalt films: Influence of the co deposition rate. *J. Appl. Phys.*, 108:093924, 2010.

[101] A. O. Adeyeye et al. Size dependence of the magnetoresistance in submicron feni wires. *J. Appl. Phys.*, 79:6120, 1996.

[102] J. P. Attane et al. Magnetic domain wall propagation unto the percolation threshold across a pseudorectangular disordered lattice. *Phys. Rev. Lett.*, 93:257203, 2004.

[103] A. Thiaville et al. Measurement of the stray field emanating from magnetic force microscope tips by hall effect microsensors. *J. Appl. Phys.*, 82:3182, 1997.

[104] J. Vogel et al. Nucleation of magnetisation reversal, from nanoparticles to bulk materials. *C. R. Physique*, 7:977, 2006.

[105] V. D. Nguyen et al. Detection of domain-wall position and magnetization reversal in nanostructures using the magnon contribution to the resistivity. *Phys. Rev. Lett.,*, 107:136605, 2011.

[106] B. Raquet et al. Electron-magnon scattering and magnetic resistivity in 3d ferromagnets. *Phys. Rev. B*, 66:244331, 2002.

[107] A. P. Mihai et al. Electron-magnon diffusion and magnetization reversal detection in fept thin films. *Phys. Rev. B*, 77:060401, 2008.

[108] K. Kondou et al. Single shot detection of the magnetic domain wall motion by using tunnel magnetoresistance effect. *Appl. Phys. Express*, 1:0613021, 2008.

[109] S. Park et al. Asymmetric domain wall depinning under current in spin valves with perpendicular anisotropy. *Appl. Phys. Lett.,*, 98:232512, 2011.

[110] V. Uhlir et al. Direct observation of oersted-field-induced magnetization dynamics in magnetic nanostripes. *Phy*, 83:020406(R), 2011.

[111] A. V. Khvalkovskiy et al. High domain wall velocities due to spin currents perpendicular to the plane. *Phys. Rev. Lett.,*, 102:067206, 2009.

[112] X. M. Cheng et al. Antisymmetric magnetoresistance in magnetic multilayer with perpendicular anisotropy. *Phys. Rev. Lett.*, 94:017203, 2005.

[113] P. Segal et al. Asymmetric field dependence of magnetoresistance in magnetic films. *Phys. Rev. B*, 79:144434, 2009.

[114] G Rodriguez-Rodriguez et al. Study of domain wall propagation in nanostructured copt multilayers by using antisymmetric magnetoresistance. *Journal of Physics: Conference Series*, 200:042021, 2010.

[115] G. Xiang et al. Theoretical analysis of the influence of magnetic domain wall on the longitudinal and transverse magnetoresistance in tensile strained (ga,mn)as multilayers. *Phys. Rev. B*, 76:054440, 2007.

[116] H. Tang et al. Electrical transport across an individual magnetic domain wall in (ga,mn)as microdevice. *Phys. Rev. B*, 70:205213, 2004.

[117] P. M. Levy et al. Resistivity due to domain wall scattering. *Phys. Rev. Lett.*,, 79:5110, 1997.

[118] R. Danneau et al. Individual domain wall resistance in submicron ferromagnetic structures. *Phys. Rev. Lett.*, 88:1572011, 2002.

[119] H. Tanigawa et al. Domain wall resistance in fept wire with perpendicular magnetic anisotropy. *J. Appl. Phys.*, 99:08G520, 2006.

[120] F. J. Jedema et al. Electrical spin injection and accumulation at room temperature in an all-metal mesoscopic spin valve. *Nature*, 410:345, 2001.

[121] P. Laczkowski et al. Spin signal in metallic lateral spin valves made by a multiple angle evaporation technique. *Appl. Phys. Express*, 4:063007, 2011.

[122] X. Fan et al. Electrical detection of microwave assisted magnetization switching in a permalloy microstrip. *Appl. Phys. Lett.*, 95:062511, 2009.

[123] J. Akerman et al. Stochastic nature of the domain wall depinning in permalloy magnetic nanowires. *Phys. Rev. B*, 82:064426, 2010.

[124] C. Hassel et al. Domain wall resistance in epitaxial fe wires. *J. Magn. Magn. Mater.*, 323:1027, 2011.

[125] T. Wang et al. A magnetic force microscopy study of the magnetic reversal of a single fe nanowire. *Nanotechnology*, 20:105707, 2009.

[126] M. Jamet et al. Magnetic anisotropy of a single cobalt nanocluster. *Phys. Rev. Lett.*, 86:4676, 2001.

[127] http://math.nist.gov/oommf/.

[128] T. Y. Chung et al. Magnetization reversal in single domain permalloy wires probed by magnetotransport. *J.Appl. Phys.*, 103(7):07C506, 2008. cited By (since 1996) 2.

[129] Y. Liu et al. Handbook of advanced magnetic materials, volume i: Advanced magnetic materials: Nanostructural effects. *Publisher: Springer, ISBN-10: 1402079834*, 2005.

[130] K. J. Kim et al. Electric current effect on the energy barrier of magnetic domainwall depinning: Origin of the quadratic contribution. *Phys. Rev. Lett.*, 107:217205, 2011.

[131] J. Briones et al. Stochastic and complex depinning dynamics of magnetic domain walls. *Phys. Rev .B*, 83:060401(R), 2011.

[132] M. Y. Im et al. Direct observation of stochastic domain-wall depinning in magnetic nanowires. *Phys. Rev. Lett*, 102:147204, 2009.

[133] M. Eltschka et al. Non-adiabatic spin torque investigated using thermally activated magnetic domain wall dynamics,. *Phys. Rev. Lett*, 105:056601, 2010.

[134] F. Garcia-Sanchez et al. Effect of crystalline defects on domain wall motion under field and current in nanowires with perpendicular magnetization. *Phys. Rev. B*, 81:134408, 2010.

[135] E. Martinez et al. Thermal effects on domain wall depinning from a single notch. *Phys. Rev. Lett.,*, 98:267202, 2007.

[136] S. Lepadatu et al. Dependence of domain-wall depinning threshold current on pinning profile. *Phys. Rev. Lett.,*, 102:127203, 2009.

[137] J. V. Kim et al. Influence of magnetic viscosity on domain wall dynamics under spin-polarized currents. *Phys. Rev .B*, 80:214424, 2008.

[138] L. K. Bogart et al. Dependence of domain wall pinning potential landscapes on domain wall chirality and pinning site geometry in planar nanowires. *Phys. Rev .B*, 79:054414, 2009.

[139] D. Petit et al. High efficiency domain wall gate in ferromagnetic nanowires. *Appl. Phys. Lett.*, 93:163108, 2008.

[140] K. He et al. Observation of asymmetrical pinning of domain walls in notched permalloy nanowires using electron holography. *Appl. Phys. Lett.,*, 95:182507, 2009.

[141] M. Laufenberg et al. Observation of thermally activated domain wall transformations. *Appl. Phys. Lett*, 88:052507, 2006.

[142] P. Mohrke et al. Single shot kerr magnetometer for observing real-time domain wall motion in permalloy nanowires. *J. Phys. D: Appl. Phys.*, 41:164009, 2008.

[143] M. Klaui et al. Direct observation of domain-wall configurations transformed by spin currents. *Phys. Rev. Lett.,*, 95:026601, 2005.

[144] T. J. Hayward et al. Exquisitely balanced thermal sensitivity of the stochastic switching process in macroscopic ferromagnetic ring elements. *Phys. Rev. B*, 72:184430, 2005.

[145] S. Laribi et al. Reversible and irreversible current induced domain wall motion in cofeb based spin valves stripes. *Appl. Phys. Lett.*, 90:232505, 2007.

[146] J. Cucchiara et al. Telegraph noise due to domain wall motion driven by spin current in perpendicular magnetized nanopillars. *Appl. Phys. Lett.*, 94:102503, 2009.

[147] H.S. Lee et al. Reduced stochasticity in domain wall motion with increasing pinning density in thin fe films. *New J. Phys.,*, 13:083038, 2011.

[148] J. Heinen et al. Determination of the spin torque non-adiabaticity in perpendicularly magnetized nanowires. *J. Phys.: Condens. Matter*, 24:024220, 2011.

[149] M. C. Hickey et al. Spin-transfer torque efficiency measured using a permalloy nanobridge. *Appl. Phys. Lett.,*, 97:202505, 2010.

List of publications

1. **V. D. Nguyen**, L. Vila, A. Marty, L. Notin, C. Beigné and J. P. Attané "Stochasticity of domain wall depinning in ferromagnetic nanostructures" 2012 (in preparation)
2. **V. D. Nguyen**, L. Vila, P. Laczkowski, A. Marty, L. Notin, C. Beigné and J. P. Attané "Magnetization switching detection of a single Permalloy nanomagnet using magneto-transport measurement" Appl. Phys. Lett. (to be submitted)
3. **V. D. Nguyen**, L. Vila, A. Marty, L. Notin, C. Beigné and J. P. Attané "Contribution of extraordinary Hall effects signal to the longitudinal resistance measurement of the nanowires with perpendicular anisotropy" Appl. Phys. Lett. 2012 (submitted)
4. P. Laczkowski, L. Vila, **V. D. Nguyen**, A. Marty, J. P. Attané, H. Jaffrès, J. M. George and A. Fert "Enhancement of the spin signal in Py/Au multiterminal nanodevices by lateral confinement" Phys. Rev. B **85**, 220404R (2012)
5. **V. D. Nguyen**, L. Vila, A. Marty, J. C. Pillet, L. Notin, C. Beigné, S. Pizzini and J. P. Attané "Dimensionality effects on the magnetization reversal in narrow FePt nanowires" Appl. Phys. Lett. **100**, 252603 (2012)
6. **V. D. Nguyen** , C. Naylor, L. Vila, A. Marty, P. Laczkowski, C. Beigné, L. Notin, Z. Ishaque and J. P. Attané "Magnon magnetoresistance of NiFe nanowires: size dependence and domain wall detection" Appl. Phys. Lett., **99**, 262504 (2011)
7. J. P. Attané, D. Ravelosona, A. Marty, **V. D. Nguyen** and L. Vila "Coercivity enhancement in FePt nanowires due to the suppression of available paths for domain wall propagation" Phys. Rev. B **84**, 144418 (2011)
8. **V. D. Nguyen**, L. Vila, P. Lackowski, T. Fairve, A. Marty, J. P. Attane "Detection of domain wall position and magnetization reversal in nanostructures using the magnon contribution to the resistivity" Phys. Rev. Lett., **107**, 136605 (2011)

List of presentations

1. P. Laczkowski, J. Rojas Sanchez, W. F. Savero Torres, M. Cubukcu, **V. D. Nguyen**, C. Beigné, L. Notin, C. Vergnaud, M. Jamet, A. Marty, J. Attané and L. Vila "Generation and enhancement of spin currents in metallic lateral nanostructures" **Invited talk** at Joint European Magnetic Symposia, Parma, Italy, 9-14 Sep. 2012
2. **V. D. Nguyen**, L. Vila, A. Marty, P. Laczkowski, C. Beigné, L. Notin, M. Jamet and J. P. Attané "Detection of domain wall position and magnetization reversal in nanostructure using the contribution of magnon to the resistivity" **Invited talk** at INTERMAG2012, Vancouver, Canada, 7-11 May, 2012
3. P. Laczkowski, L. Vila, W. S. Torres, M. Cubukcu,J.-P. Attané, A. Marty, C. Beigné, **V. D. Nguyen**, L. Notin "Spin injection in metal based lateral nanostructures" Invited talk at SPIE Optics+ Photonics 2011, San Diego, California, USA
4. J. P. Attané, **V. D. Nguyen**, C. Burrowes, A. Mihai, A. Marty, J. V. Kim, D. Ravelosona, F.S Garcia, L. Buda-Prejbeanu, L. Vila "Spin-transfer effects in FePt nanowires with narrow magnetic domain walls" **Invited talk** at 55th Annual Conference on Magnetism and Magnetic Materials, Alanta, Georgia, USA, 14 – 18 Nov., 2010
5. **V. D. Nguyen**, L. Vila, A. Marty, C. Beigné, L. Notin, S. Pizzini and J. P. Attané "Spin transfer effect in FePt nanowires: controlling the stochasticity of domain wall depinning using constrictions" **Oral presentation** at INTERMAG2012, Vancouver, Canada, 7-11 May, 2012
6. **V. D. Nguyen**, C. Naylor, L. Vila, A. Marty, P. Laczkowski, C. Beigné, L. Notin and J. P. Attané "Detection of domain wall position and magnetization reversal in nanostructure using the contribution of magnon to the resistivity" **Oral presentation** at Magnetic Nano-Object Workshops and School, Ecole de Physicque des Houches, France, 5-10, Feb., 2012
7. **V. D. Nguyen**, L. Vila, A. Marty, P. Laczkowski, J.C. Pillet, T. Faivre, C. Beigné, P. Warin, M. Jamet, J. P. Attané " Detection of magnetization

reversal in nanostructures using the magnon contribution to the resistivity " **Oral presentation** at Colloque Louis Neel, Brest-Oceanopolis, France, 21-23 Sep., 2011

8. **V. D. Nguyen**, L. Vila, A. Marty, P. Laczkowski, J.C. Pillet, T. Faivre, C. Beigné, P. Warin, M. Jamet, J. P. Attané "Electron-magnon interaction as a new way to detect magnetization reversal and domain wall position in nanowires" **Oral presentation** at Recent Trends in Nanomagnetism, Spintronics and their Applications (RTNSA), Pay Basque, 1– 4 June, 2011
9. **V. D. Nguyen**, L. Vila, A. Marty , C. Beigne, L. Notin, J. C.Pillet, J. F. Jaquot, S. Pizzini, M. Tissier, J. P.Attane "Coercivity enhancement and magnetization reversal modes in narrow FePt nanowires" **Poster presentation** at Joint European Magnetic Symposia, Parma, Italy, 9-14 Sep. 2012
10. **V. D. Nguyen**, L. Vila, M. Tissier, A. Marty, M. Cubukcu, P. Laczkowski, W. S. Torres, J. C. Rojas Sanchez and J. P. Attane "Magnetization reversal modes in narrow FePt nanowires with high perpendicular anisotropy" **Poster presentation** at 19th ICM, Busan, Korea, July 8-13, 2012
11. **V. D. Nguyen**, L. Vila, A. Marty, J. C. Pillet, C. Beigné, L. Notin, S. Pizzini and J. P. Attané "Magnetization reversal modes in narrow FePt nanowires with high perpendicular anisotropy" **Poster presentation** at INTERMAG2012, Vancouver, Canada, 7-11 May, 2012
12. **V. D. Nguyen**, J. P. Attané, , C. Burrowes, A. Mihai, A. Marty, J. V. Kim, D. Ravelosona, F.S. Garcia, L. Buda-Prejbeanu, L. Vila "Spin-transfer effects in FePt nanowires with narrow magnetic domain walls" **Poster presentation** at RTNSA, Pay Basque, 1– 4 June, 2011
13. **V. D. Nguyen**, L. Vila, A. Marty, T. Faivre, J. C. Pillet, A. Mihai, P. Laczkowski, Q. Riffard, L. Notin and J. P. Attané "Precise detection of domain wall position in nanowires using magnon magnetoresistance measurements" **Poster presentation** at 55th Annual Conference on Magnetism and Magnetic Materials, Alanta, Georgia, USA, 14 – 18 Nov., 2010

Acknowledgments

At the end of my PhD, I wish to take this opportunity to express my gratitude to all the people who have shared their time, dedication and enthusiasm with me during my stays in Grenoble.

First and foremost, I would like to thank J. P. Attané, L. Vila and A. Marty for giving me an opportunity to join their group, the close daily guidance in my work and enormous supports. Thank you so much for your warm encouragements and your patience in training me.

I woud like to thank all the members in the Laboratory of Nanostructures and Magnetism, INAC, CEA Grenoble who have actively contributed to the success of My PhD work. Special thanks are sent to P. Laczkowski, J. C. Rojas Sánchez, M. Cubukcu, W. Savero Torres, I. Groza, A. Jain, M. Jamet, C. Beigné, L. Notin, C. Vergnaud, A. Brenac, S. Lequien, R. Morel, J. C. Pillet and P. Warin, for sharing your time, interest, company and experience with me during my PhD in the Laboratory.

I am much appreciated all committee members of my PhD defense, A. Thiaville, M. Bailleur, H. Courtois and D. Ravelosona for making the efforts of reading my manuscript and for joining the PhD defense committee.

I would like to acknowledge all the staffs of the clean room, PTA in Grenoble, for their helps in nanofabrication process. I also thank to S. Pizzini and J. Vogel at Néel Institute, CNRS for the great supports in performing Kerr microscopy measurements. I am much indebted to the administration assistance and finance support from Nanoscience Fondation (RTRA) Grenoble.

I would like to express my deep gratitude to all the members in the Lab. of Magnetism and Superconductivity, Institute of Material Science in Hanoi, Vietnam. I specially thank my former teachers, D. N. H. Nam, N. X. Phuc and L. V. Hong for their constant support and sustained encouragements. Also, I wish to thank the Director of Institute of Material Science, N. Q. Liem for his supports.

During my stays in Grenoble, I had a great time to stay with Ducros family. Very special thanks are sent to Anne and Gerard for their love and

encouragements. Also, I am very grateful to Moriceau family for their supports. Thanks all Vietnamese friends in Grenoble who have always brought unforgettable time when we were together.

This is great time for me to express the gratitude to my family, in particular, my parents for their patience and understanding. Finally, the most beloved thanks are saved for my wife, Thanh Ngoc and in particularly for my little son, Nhat Quang who just arrived one week after my defense. During the 3 years, the large distance between Grenoble and Troyes made our life more difficult. Their love has provided me incredible support, which apparently helped me to overcome all difficulties over these years.

Abstract

In the first part of this thesis, we study the magnetization reversal process of FePt nanowires with high magnetocrystalline anisotropy. When reducing the wire width below the mean dendrite width, the magnetization reversal favors a transition from the dendrite growth to the propagation of a single domain wall (DW). Further decreasing of the width towards the disorder length and/or the mean edge roughness leads to a large increase of coercivity, which finally results in a mix of DW propagation and nucleation in ultra-narrow wires.

The second part focuses on the use of Magnon magnetoresistance (MMR), *i.e.,* the magnon contribution to the resistivity, to study the magnetization reversal in nanostructures with either perpendicular (FePt) or planar magnetization (NiFe). We showed that MMR can be used in nanowires and nanomagnets, in particular to detect DW position in nanowires processed in a single layer.

Finally, the dynamic of DW depinning under field and current in both FePt and NiFe systems has been studied. We observe three different modes of DW depinning, which depend on the nature of defects, or on the geometry of the constriction. Statistical analysis of the pinning time indeed shows that the depinning path can be described as simple path, serial paths or alternative paths. Additionally, the effect of DC current on all depinning mechanisms is found to be equivalent to the effect of applied field which, allow measuring the spin transfer efficiency in these systems.

Keywords: Magnetization reversal, magnon magnetoresistance, domain wall, spins transfer torque.

Résumé

Dans la première partie de cette thèse, nous étudions le renversement de l'aimantation de nanofils d'alliage FePt à forte anisotropie magnétocristalline. Lorsque la largeur du fil devient inférieure à la taille des dendrites, nous avons montré qu'il existe une transition du processus de renversement de l'aimantation, de la croissance de dendrites vers la propagation d'une paroi magnétique unique qui renverse tout le fil. Au-delà, la diminution de la largeur du fil jusqu'à la taille caractéristique du désordre et/ou de la rugosité moyenne conduit au renforcement de la coercivité. Ceci conduit finalement dans les fils ultra-fins à un renversement consistant en un mélange de nucléation de domaines et de propagation de parois magnétiques.

Dans la deuxième partie, nous rapportons l'utilisation de la magnétorésistance de Magnon (MMR), qui provient de la contribution des magnons à la résistivité, pour mesurer le renversement d'aimantation, dans des nanostructures avec aimantation perpendiculaire (FePt) ou planaire (NiFe). Nous avons montré que la MMR peut être utilisée pour détecter le retournement de l'aimantation dans les nanofils et nano-aimants, et en particulier pour détecter la position d'une paroi magnétique le long d'un nanofil fabriqués à partir d'une couche unique.

Enfin, nous étudions dans une dernière partie la dynamique de dépiégeage de paroi magnétique sous champ et sous courant, dans les deux systèmes FePt et NiFe. Nous observons trois types de dépiégeage de paroi, qui dépendent de la nature des défauts ou de la géométrie de la constriction. L'analyse statistique du temps de piégeage montre que le processus de dépiégeage peut être décrit comme procédant d'un chemin simple, de chemins en série, ou de chemins alternatifs. En outre, l'effet du courant sur tous ces mécanismes de dépiégeage s'est révélé équivalent à l'effet du champ appliqué, ce qui permet de mesurer l'efficacité du transfer de spin dans ces systèmes.

Mot clés: Renversement de l'aimantation, magnétoresistance de magnon, paroi magnétique, effets de transfert de spin